JJ-2001

Fixed-Wing Micro Air Vehicle for the 2020 WPI UAV Competition

A Major Qualifying Project Report
Submitted to the Faculty of the
WORCESTER POLYTECHNIC INSTITUTE
in Partial Fulfillment of the Requirements for the
Degree of Bachelor of Science
in Aerospace Engineering

by

Jared DeMaio

Hector Gonzalez

Aleye Okhipo

Sully Naji

Michael Salamone

Michael Salamone

April 7, 2020

Approved by:

_____

Jagannath Jayachandran, Advisor
Assistant Professor, Aerospace Engineering Program
WPI

_____

David J. Olinger, Co-Advisor
Associate Professor, Aerospace Engineering Program
WPI

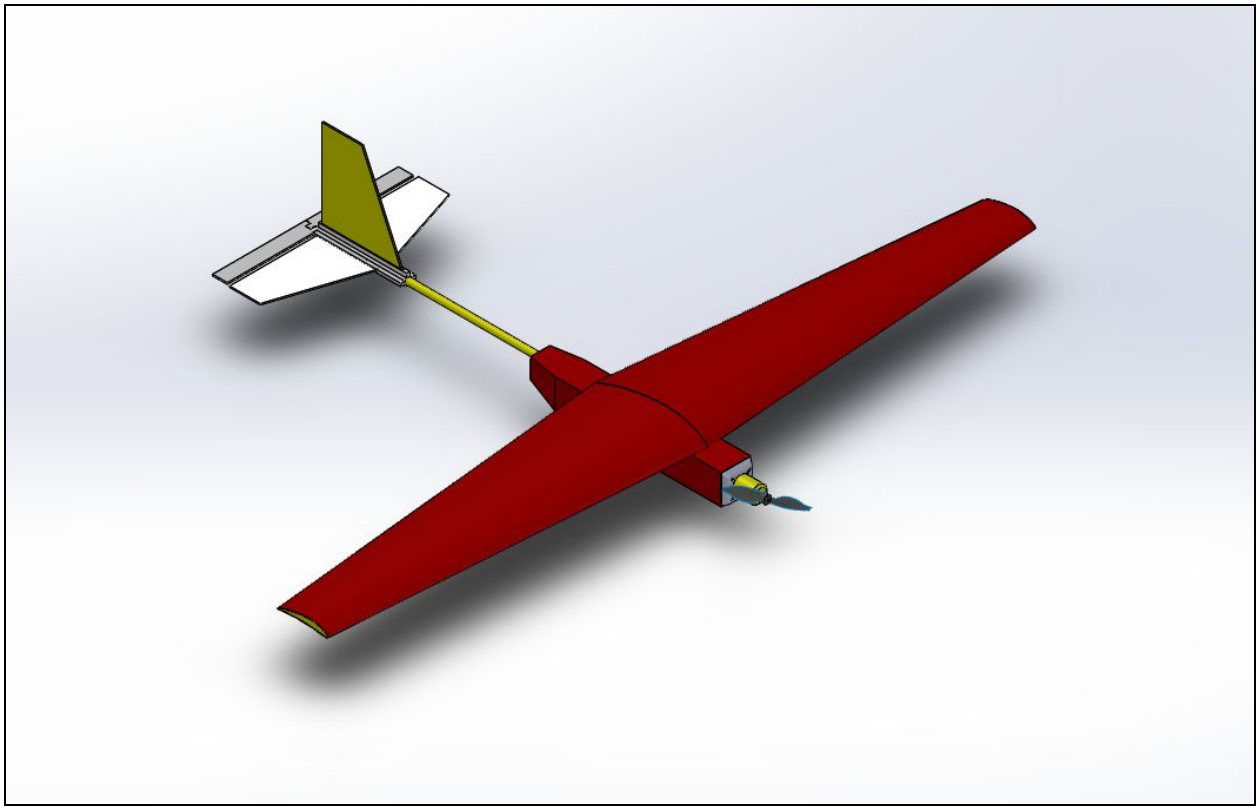

Completed Aircraft

Abstract

A Fixed Micro Air Vehicle was designed and constructed in order to compete in the 2020 WPI UAV Competition, for which the scoring was based on weight fraction, flight time, payload target accuracy, autonomy, and originality. Some key features of the aircraft were its carbon fiber design, its 6.02 foot wingspan, and unloaded weight of 3.92 pounds. The one flight test performed revealed issues with stability and handling, which could not be resolved due to the Coronavirus pandemic.

Table of Contents

List of Figures

List of Tables

Acknowledgements

Our team would like to thank the following individuals for their guidance, support and assistance throughout the completion of this project.

Project Advisor	Professor Jagannath Jayachandran
Project Co-Advisor	Professor David J. Olinger
RC Pilot	Keith Blackstock
Financial Administrator	Barbara Furhman
Flight Test Airfield	Millis Model Aircraft Club

Table of Authorship

Section	Author[s]	Editor[s]
1.0 Introduction	Gonzalez, Salamone	Salamone
1.1 Background and Literature Review	Naji	Naji
1.2 Mission Requirements	Gonzalez, Salamone	Okhipo
1.3 Project Management	Gonzalez, Salamone	Okhipo
1.4 Tasks and Timetable	Gonzalez, Salamone	Okhipo
2.0 Specifications & Design Summary	DeMaio	Okhipo
2.1 Weight Buildup Table	Salamone	Gonzalez, DeMaio
3.1 Preliminary Drawings	Salamone	Okhipo
3.2 Initial Sizing	DeMaio	Okhipo
3.3 Scoring Breakdown	DeMaio	Gonzalez
4.1 Aerodynamic Analysis	DeMaio	Gonzalez
4.2 Structural Design	Okhipo, Salamone	Gonzalez
4.3 Propulsion System Design	Salamone, DeMaio	Gonzalez
4.4 Control System Design	Gonzalez, Okhipo, DeMaio	Salamone
5.1 Additive Manufacturing	Salamone	Naji
5.2 Carbon Fiber Hand Lay-up	DeMaio	Naji

5.3 Wing Manufacturing	DeMaio	Gonzalez
5.4 Tail Manufacturing	DeMaio	Salamone
5.5 Control Surfaces	Gonzalez, Okhipo	Salamone
5.6 Fuselage Manufacturing	DeMaio	Okhipo
6.1 Wind Tunnel Test	DeMaio	Salamone
6.2 Fuselage Structure Test	Okhipo	Gonzalez, Naji
6.3 Wing Loading Test	DeMaio	Okhipo
6.4 Glide Test	DeMaio	Gonzalez
6.5 Flight Test	DeMaio	Salamone
7.1 Summary	Gonzalez	DeMaio
7.2 Conclusions	DeMaio, Okhipo	Okhipo
7.3 Project Broader Impact	DeMaio	Gonzalez
Appendix A	DeMaio	Okhipo
Appendix B	DeMaio	Okhipo
Appendix C	Okhipo	Salamone
Appendix D	Salamone	Gonzalez
Appendix E	Salamone, Naji	---

1.0 Introduction

The goal of this Major Qualifying Project (MQP) was to design and construct a Micro class Air Vehicle (MAV) to compete at the 2020 Worcester Polytechnic Institute Unmanned Aerial Vehicle (UAV) Competition. A Micro Air Vehicle, is a class of unmanned aerial vehicles (UAV), or, an aircraft without a human pilot on board. This competition required our team to design and construct an aircraft that would take-off from a specific area, deliver a payload at a specified target location, and return to the landing area. Our team utilized knowledge of WPI coursework as well as conducted research during the design and construction process of our aircraft.

The primary goal of the WPI UAV competition was to have our aircraft adhere to the established strict regulations and requirements while scoring maximum points during the competition. The aircraft's mission requirements for the competition were divided into three sections: taking-off by hand launch at the take-off/landing zone, flying and delivering our payload on the specified target location, and returning to the take-off/landing zone. The team's competition score is based on aircraft endurance, payload accuracy, average velocity, and autonomous capabilities. Scoring metrics are shown below in Fig. 1.

$$S = \lambda_1 \frac{W_{\text{payload}}}{W_{\text{empty}}} \cdot t_{\text{flight}} \cdot V_{avg} + \lambda_2 \Delta + \lambda_3 \sum_n A_n + P.$$

Symbol	Meaning
$W_{\text{loaded}}, W_{\text{empty}}$	Weight of the aircraft with and without payload, respectively
t_{flight}	Time of flight in range leg in secs
V_{avg}	Average groundspeed during flight, computed using onboard GPS-based speed measurements in meters/sec.
Δ	Define δ to be the distance between the target location and actual payload drop point. Then $\Delta = \begin{cases} 1, & 0 < \delta < 1\text{ m}, \\ 0, & 1\text{ m} \leq \delta < 3.5\text{m}, \\ -1, & 3.5\text{m} < \delta. \end{cases}$
A_n	Points for demonstrating autonomy capabilities $n = 1, \ldots, 5$ (see Section 1.8) $A_1 = A_2 = A_5 = 1,$ $A_3 = 3,$ $A_4 = 5.$
P	Originality points on a scale of $0 - 10$.
λ_i	Constants $\lambda_1 = 0.01$, $\lambda_2 = 35$, and $\lambda_3 = 35$.

Figure 1: Competition Scoring Metrics

Our team's early efforts focused on researching the different aircraft design areas of aerodynamics, structures, stability and controls, and propulsion. A table demonstrating how our team divided the work, and the team's project management plan, can be seen in Sec. 1.4. The team designed a unique aircraft based upon the research we conducted in the nascent stages of this project. Group decisions were shaped by research, calculations, analysis, and tests, such as thrust, gliding, and flight tests. This report aims to detail the different steps taken by the team to achieve our final goal of building an aircraft and successfully participating in the competition.

1.1 Background and Literature Review

To gain a deeper understanding of the tasks at hand while designing a micro aircraft, literature review was performed. This literature review encompassed textbooks, academic journals, and online resources. Below is a brief description of the main topics that were researched for our project.

1.1.1 Aerodynamics

The primary purpose of the literature review in the aerodynamics component of the project was to determine the wing and tail shapes and locations. For these purposes, Raymer (2018) proved to be a valuable resource.

Most past MQP's have had a straight wing, where the taper ratio $\lambda=1$, for ease of manufacturing. According to Raymer (2018), the most aerodynamically efficient wing is an elliptical wing. However, a wing with a taper ratio of 0.45 results in drag due to lift that is less than 1 percent higher than an elliptical wing platform for the same aspect ratio. The tapered wing also incurs about 7 percent lower drag due to lift than that of a rectangular wing platform (*see* Raymer, 2018).

In terms of wing placement, a high wing has more inherent stability characteristics than low or mid wing designs. It also allows for the possibility of payload to be carried under the fuselage without extra structural support needing to be passed through the center of the fuselage (*see* Raymer, 2018). A third benefit is that there is less risk of catching a wing tip on the ground during landing, which mitigates the risk of disqualification.

Several tail designs exist, such as a T-tail and V-tail , but the stall characteristics of the T-tail (i.e. less control authority at high angles of attack) and the non-linear relations between latitudinal and longitudinal modes presented by the V-tail made these options undesirable for a project with our time and budget constraints (*see* Raymer, 2018). The traditional tail design is something that our team is comfortable with, and has experience writing control algorithms for after taking Professor Cowlagi's Aircraft Dynamics and Control class (*see* Cowlagi, 2019).

1.1.2 Structures

The team began background research with the analysis of several previous MQP's. Also, the team used notes from structures and design classes at WPI. These notes provided a flow chart of how to go about the design process. We decided to use Solidworks to create 3-dimensional models and perform preliminary stress and deflection analyses of components. The criteria for the selection of materials included: strength, weight, ease of manufacturing, and price.

After completing research on model building materials suitable for use in model airplanes, we concluded that the most common are balsa wood and composites such as carbon fiber and fiberglass. All of these materials have specific attributes that make them suitable for specific applications, and these attributes were taken into consideration to make a decision. Balsa wood is used to build model aircraft today due to its inexpensive cost, large availability, and low density. Unlike metals and some composites, balsa wood is relatively easy to shape as desired. It is also very strong in tension but does not perform as well in compression. Composite materials are typically strong in one specific direction. These materials are typically strongest in the direction that the fiber strands are in tension. For this reason, composites are set up in layers and

then a very strong resin is applied to bond the layers together. The most common types of composites are fiberglass and carbon fiber. The difference between the two types is in strength and weight. Carbon fiber can withstand significantly more stress than fiberglass.

1.1.3 Controls

This section discusses the control surfaces, servo sizing, and autonomy and flight controller background and literature review.

1.1.3.1 Control Surfaces

In order to understand the different controls components, the team conducted research and literature review. The team conducted research on different controls surfaces and how the sizes are determined. From reading Sadraey (2012) and Raymer (2018), we discovered that a historical data approach was needed to size the control surfaces. According to Raymer, every control surface of an aircraft takes up a specific amount of area percentage. These percentages are standard when designing an aircraft, therefore, we took into consideration the size of our wing and the amount of area each control surface was going to take. Although the area percentages shown in Raymer's (2018) book are standard approximations used for larger aircrafts, we were able to use these percentages to design our control surfaces. Table 1 below demonstrates the area percentage approximations we used when sizing the control surfaces of the aircraft.

Control Surface	**Area Percentage**
Flaps	35%
Ailerons	10%
Elevator	40%

Rudder	35%

Table 1: Area percentage approximations used from Raymer's (2018) textbook.

1.1.3.2 Servo Sizing

In order to find the adequate servo mechanism for each control surface, the team conducted research on how to properly size the servos. We found each servo needs to produce a certain amount of torque output in order to move the control surfaces. The amount of torque required was dependent on different variables, for example, the length of the control surface, different aerodynamic forces, and the maximum control surface deflection. We used a torque equation formulated by Chuck Gadd (*see* Servo Torque Calculator, n.d) to calculate our torque and adequately size our servos. This equation used variables such as the chord length of the control surface, the length of the control surface, the maximum control surface deflection relative to the wing, the maximum servo deflection. Although most of these variables were calculated by us, we used historical data approximations in Raymer's (2018) textbook for the maximum control surface and servo deflection angles.

1.1.3.3 Autonomy and Flight Controller

As previously mentioned in the introduction, part of the team's score consists of points for demonstrating autonomy and targeted payload drop. In order to achieve this the team needed to select a flight controller. A flight controller is a small computer with several integrated sensors that allows a pilot to control the movement of the aircraft using command inputs given via the radio transmitter. Additionally, using the integrated sensors, a flight controller is able to measure and store real time flight data and control the aircraft autonomously. (*see* Montgomery, 2014)

Most flight controllers have various sensors that supplement their calculations, for example, a gyroscope helping with an aircraft's orientation. When picking a flight controller, the team's main priority was finding one that could perform waypoint navigation, was relatively inexpensive, and one that has a large user base. The large user base was important because we wanted to make sure we had adequate resources available in case we encountered any issues with the flight controller.

After researching different flight controllers the team decided on the Pix hawk 4 mini, hereafter referred to as PX4 mini. The PX4 mini comes with an external GPS, powerboard and connection cables. It also includes a pre-programmed firmware that instructs and communicates with our electronic components, such as servos and the motor, in order to fly our plane. This firmware can be altered and designed to fit the specific needs of our plane.

In order to conduct waypoint navigation and automatic payload drop, the mission has to be mapped using a ground control system. A ground station is a software application that is used to communicate with the flight controller, PX4 mini, via wireless telemetry. It also displays real-time data on the plane's performance and position which helps during autonomous flight, waypoint navigation and automatic target detection. The two most popular and compatible ground station softwares are Mission Planner and QGround control. QGround control has a better user interface and is easier to learn. It is also very compatible with the Pixhawk 4 mini in terms of calibration. Mission Planner, on the other hand, is harder to navigate as a first time user but has more capabilities compared to QGround control. Therefore, we decided to use Mission Planner, as seen in Fig. 2, due to its compatibility with the PX4.

Figure 2: A Snapshot of Mission Planner

1.1.4 Propulsion

This section discusses the battery, electronic speed controller, motor, and propeller background and literature review. The team also consulted associates from *Hog Heaven Hobby Shops* in Sturbridge, MA.

1.1.4.1 Battery

The WPI UAV Competition Rules allow a maximum battery size of a 3 cell 11.1 volt, 2200 mAh. A 3 cell battery, hereafter referred to as 3S pack, holds 3.7 volts per cell. 2200 mAh represents the capacity of the battery. mAh represent milliamp hours (*see* Schneider, 2020).

Lithium polymer, hereafter referred to as LiPo, is the material of the battery. There are other types of batteries. For example, Nickel-Cadmium and Nickel-Metal Hydride. LiPo batteries are more popular because they are lighter and have higher charge rates (*see* Schneider, 2020). The discharge rating, hereafter referred to as C rating represents maximum safe amp draw of a

given battery. The safe amp draw is calculated by multiplying the C rating by the overall capacity of the battery (*see* Schneider, 2020).

1.1.4.2 Electronic Speed Controller

The electronic speed controller, hereafter referred to as ESC, uses pulse width modulation to convert the signal from controller into a voltage in order to regulate motor speed (*see* Liang, 2016). The ESC must have at least 20% more capacity than the battery to operate at low temperature (*see* FliteTest, 2019). A battery elimination circuit, hereafter referred to as BEC, is built into the ESC. The BEC regulates voltage from the LiPo battery. This eliminates the need for a separate battery for the ESC (*see* Liang, 2020).

1.1.4.3 Motor

There are two types of brush motors available for remote control planes: Brushed and brushless motors. Brushed motors provide current to the motor windings. Brushless motors, on the other hand, do not have these windings. Brushed motors have simple wiring, but are less efficient than brushless motors (*see* Commutating Encoder, 2019).

There are inrunner and outrunner motors. Inrunner motors rotate the shaft inside the outer motor casing. Outrunner motors rotate the entire outer casing about the center of the motor. Outrunner motors are popular for UAVs. Inrunner motors are typically found on UAV helicopters (*see* FliteTest, 2019).

Motor speed is determined by RPM per volt rating (Kv) (FliteTest, 2019). A large Kv rating signifies more RPM.

Motor power is denoted by watts. Wattage can be determined by multiplying voltage and amperage (*see* FliteTest, 2019). The higher the volts or the higher the amperage, the larger power

output. Motor thrust for remote control planes has more steps. Thrust is a function of battery and propeller size. Correctly sizing the battery and propeller will optimize the thrust of the motor (*see* FliteTest, 2019).

1.1.4.4 Propeller

There are multiple types of propeller configurations. There are "in front of" or "behind" propellers. These names reflect the propeller placement on the fuselage. There are also tractor and pusher propellers. Tractor propellers rotate counterclockwise, and pusher propellers rotate clockwise. These directions are determined by an observer looking from in front of the propeller (*see* Iskrev, 2015). Pusher propellers are more efficient than tractor propellers. This is because tractor propellers are pulling air over the aircraft's skin. Pusher propellers, on the other hand, do not have to account for this.

Propeller selection is governed by the motor size. Manufacturers will give a list of suggested propellers for thrust optimization (*see* Weakley, 2018). Propeller dimension convention is represented as 'diameter x pitch'. Diameter represents the overall length of the propeller. The pitch represents the distance traveled per one revolution (*see* RC Airplanes, 2019). Two bladed propellers are more efficient than three or four bladed propellers. Three or four bladed propellers are desirable if propeller [ground] clearance is an issue, and multiple engines are needed. A balanced propeller is necessary to avoid vibrations. Vibrations are undesirable because they reduce engine life. Propeller balancers can be used to re-balance a propeller (*see* RC Airplanes, 2019).

1.2 Mission Requirements

The mission requirement is to take-off from a specified take-off/landing area, deliver payload at a specified target location, and return and land in the take-off/landing area. For a complete list of requirements, see the 2020 WPI UAV Competition Rules. The venue layout can be seen in Fig. 3.

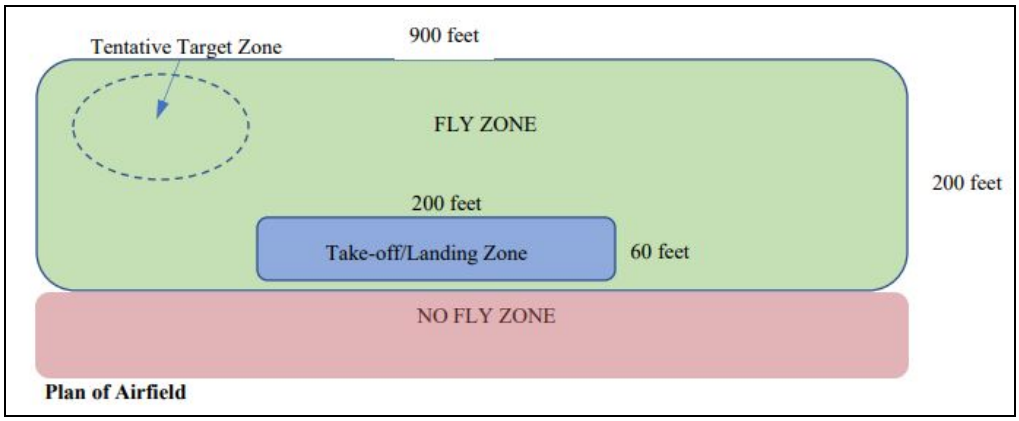

Figure 3: Layout Of The Airfield For The 2020 WPI UAV Competition

1.3 Project Management

In order to efficiently complete this project and the competition, our team of five students were divided into four different groups. These four groups were aerodynamics, structures, propulsion, and controls and stability. Students in each group were responsible for research, analysis, fabrication, and testing. Table 2 shows the different groups.

Unit	Owner	Description
Aerodynamics	DeMaio	Create airfoil prototype, Conduct wind tunnel tests, Wing Sizing Analysis
Structures	Naji	Material testing, SolidWorks Modeling, Aircraft design
	Okhipo	

	Salamone	Additive Manufacturing
Controls and Stability	DeMaio	Controls surface sizing, Servo sizing, Servo and control surfaces linkage, Lateral controls, Static and Dynamic stability, Wiring diagram, Flight Controller selection
	Gonzalez	
	Okhipo	
Propulsion	Salamone	Propeller selection, Motor selection, Electronic Speed Controller selection

Table 2: Team Project Management And Subgroups

1.4 Tasks and Timetable

To ensure our aircraft was fully functional by the deadline, the team created milestones to keep us on track. The breakdown and timeline of these tasks can be seen in Table 3 below.

	A Term	**B Term**	**C Term**
Aerodynamics	Literature Review, Aerodynamic Analysis, Wind Tunnel Test	XFLR5 corrections, SolidWorks Model	
Structures	Literature Review, Destructive and non destructive tests	SolidWorks Model, Wing Build, Glide Test Prototype,	Updated SolidWorks Payload Release fabrication Fuselage Construction
Controls	Literature Review	Control Surface Sizing, Servo Sizing, Servo Linkage Lit Review, Lateral Controls	Cutting of control surfaces, Servo and control surfaces linkage, Autonomy
Propulsion	Literature Review	Propeller and Motor Procurement	

Table 3: Group Project Timeline

2.0 Specifications & Design Summary

This section includes a summary of specifications. These specifications have been developed and modified throughout the course of the project and result from analysis detailed in later sections of this paper. This section tabulates the design parameters, so that the reader can easily find all dimensions that are of specific interest.

Specification	Value
Cruise Airspeed (ft/s)	42 (ft/s)
Payload (lbs)	2 (lbs)
Empty Weight (lbs)	4.61 (lbs)
Time of Flight (min)	19.7 (min)
Range (m)	15,148 (m)
Propulsion	1 electric motor

Table 4: Design Specifications

These specifications, which are explained in detail in Section 3, guided our project at the beginning and allowed us to formulate our design. The following table displays a summary of the key design parameters of our aircraft.

Specification	Value
Overall Length	3.8 (ft)
Empty Weight	3.92 (lbs)
Gross Weight (Theoretical)	6.61 (lbs)

Specification	Value
Range (Theoretical)	9.41 (mi)
Most-Forward Point	35.85% Chord
CL Required	0.95

Specification	Value
Wing Span	6.02 (ft)
Wing Area	4.14 (ft^2)
Wing Root Chord	0.9487 (ft)
Wing Tip Chord	0.4269 (ft)
Wing Mean Aero Chord	0.72 (ft)
Wing Taper Ratio	0.45
Wing Aspect Ratio	8.76
Wing Airfoil	NACA 8412
Wing Configuration	High Mounted
Wing Incidence Angle	2.65 degrees
L/D at Cruise	19.2
W/S Cruise	1.6680 lb/ft^2
W/S Loiter	2.8891 lb/ft^2
W/S Stall	1.8346 lb/ft^2
Stall Speed	27.4864 (ft/s)
Neutral Point	65.55% Chord

Specification	Value
HT Area	0.4978 (ft^2)
HT Span	1.41 (ft)
HT Root Chord	0.4704 (ft)
HT Tip Chord	0.2352 (ft)
HT Taper Ratio	0.5
HT Aspect Ratio	4
HT Airfoil	NACA 0008
VT Area	0.3329 (ft^2)
VT Height	0.7066 (ft)
VT Root Chord	0.6281 (ft)
VT Tip Chord	0.3140 (ft)
VT Taper	0.5
VT Aspect Ratio	1.5
VT Airfoil	NACA 0008
Tail Configuration	Conventional
Center of Gravity	55% Chord

Table 5: Final Design Parameters

The final design drawing is presented in larger format in Appendix E, but is also presented here.

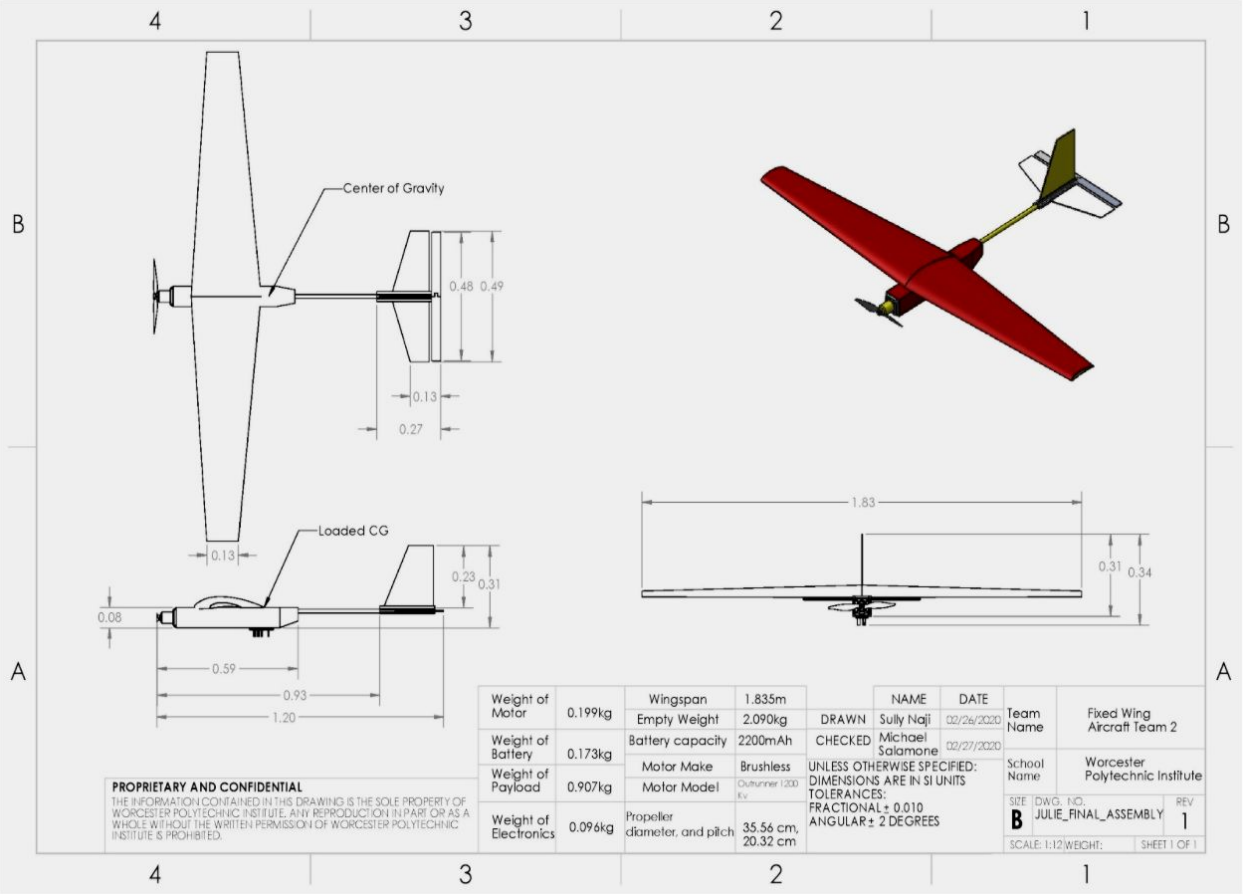

Figure 4: Final Design Drawing

An image of the final aircraft as-built is also presented here.

Figure 4a: As-Built Photo of Aircraft

2.1 Weight Buildup Table

Table 6 shows the weight buildup of the aircraft components in alphabetical order.

Component	Weight (lbs)
Battery	0.38
Carbon Fiber Wing	0.79
Electronic Speed Controller	0.18
Foam Wing	0.39
Fuselage	0.70
Horizontal Tail Control Surface	0.08
Horizontal Tail; x2	0.18 (Including both)
HS - 40 Servo; x2	0.02
HS - 45HB Servo; x3	0.05
HS - 53 Servo; x2	0.04
Motor	0.44
Nose	0.12
Payload Release	0.1
Pixhawk 4 Mini	0.08
Power Distribution Board	0.02
Propeller	0.01
Tail Connector	0.12
Tail Rod	0.10
Vertical Tail	0.12
Total Weight	**3.92**

Table 6: Weight Buildup Table

3.0 Preliminary Design

To begin the design of our MAV, we decided to utilize the basic design progression laid out by Raymer (2018) and the AE 4770 Aircraft Design class taught by Professor Olinger at WPI. This approach is laid out for conventional fuel aircraft at full-scale, meaning that the design approach had to be modified in order to fit the parameters given in our competition rules and the limitations of the historical data available to us. See the flowchart in Fig. 5.

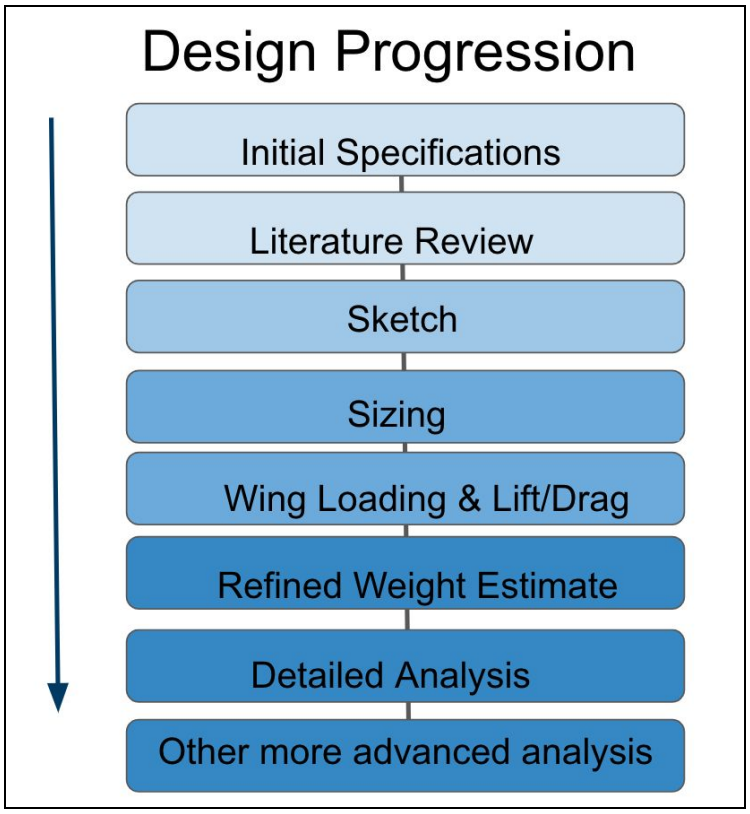

Figure 5: Design Process (Olinger, 2019)

3.1 Preliminary Drawings

The team decided on a high wing, front tractor propeller, conventional tail design. The high wing design was to avoid a mid wing or low wing that may obstruct the payload. The front

tractor propeller was chosen because it places the center of mass further forward on the fuselage. A center of mass closer to the nose is desirable for stability. A rear pusher propeller also risks hitting the payload upon release. The team opted for a conventional tail because of the team's more extensive knowledge of stability for a conventional tail. An initial drawing of the aircraft can be seen in Fig. 6. Note, the wing in this design is much farther forward than the one present in the final design drawing in Section 2.0 and in Appendix E. The payload mechanism was also neglected in the initial concept and was added in later stages of the design.

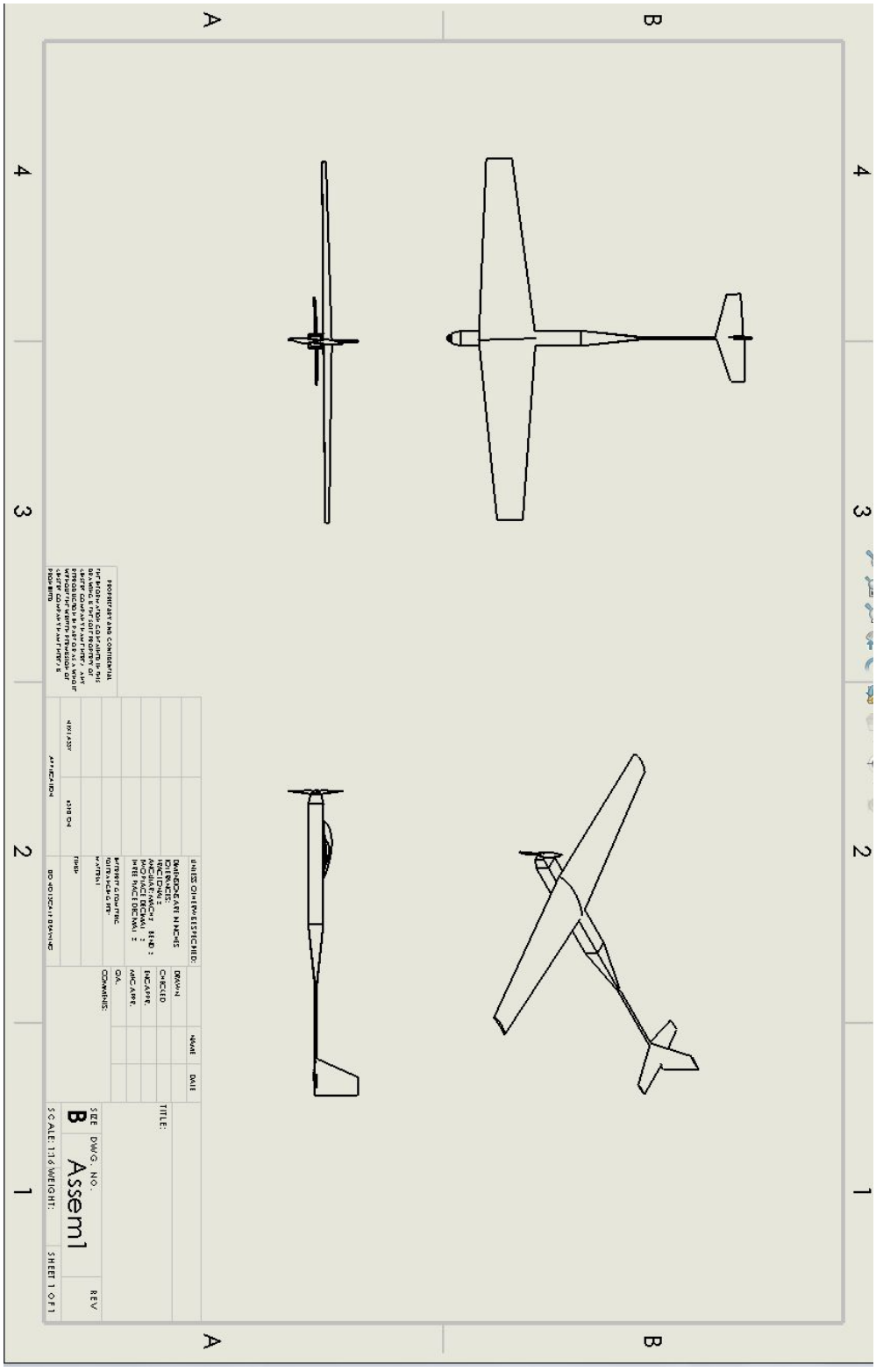

Figure 6: Initial 4 View Drawing

3.2 Initial Sizing

In Raymer (2018), one important consideration is the weight of the aircraft. In our application, weight is not a function of time/range as it is for conventionally fueled aircraft. In order to conduct our calculations, we made the assumption that our aircraft would be flying at the maximum allowable weight of 6.61 lbs for the duration of our flight. In order to define our initial design parameters, we decided to collect and analyze historical data to get an idea for what size and shape our aircraft should take. Many of the calculations performed in this section are directly out of Raymer (2018).

3.2.1 Trade Studies

To perform trade studies, we analyzed past MQP reports to collect historical data. From these reports we plotted each aircraft's overall length, aspect ratio, and wing loading against gross weight. The MQP's referenced for this analysis were the fixed wing projects from 2012, 2014, 2015, 2016, 2017, and 2019 (Andraka et al, 2015; Blair et al, 2012; Brown et al, 2017; Celaj et al, 2019; Lipka et al, 2014; and Smith et al, 2016). The plot of overall length to weight is displayed below in Fig. 7.

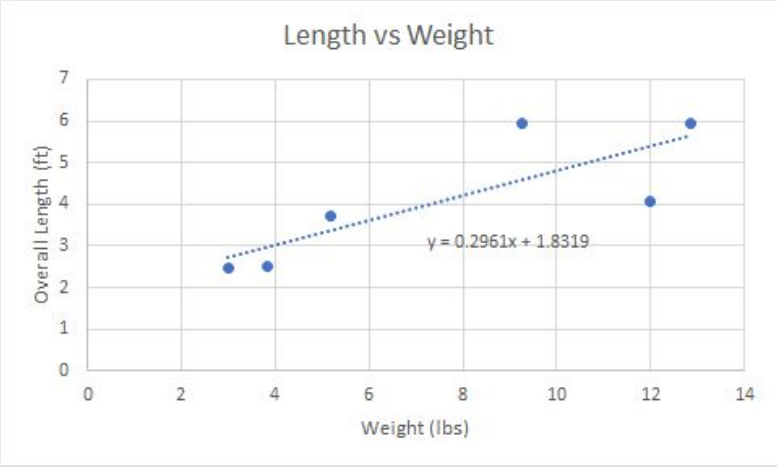

Figure 7: Length vs Weight Trade Study

This plot shows MQP aircraft with larger gross weights have been longer from nose to tail than lighter aircraft. The linear regression line in Fig. 7 forecasts the aircraft will be approximately 3.8 ft in length. Fig. 8 displays the aspect ratio of the main wing versus weight.

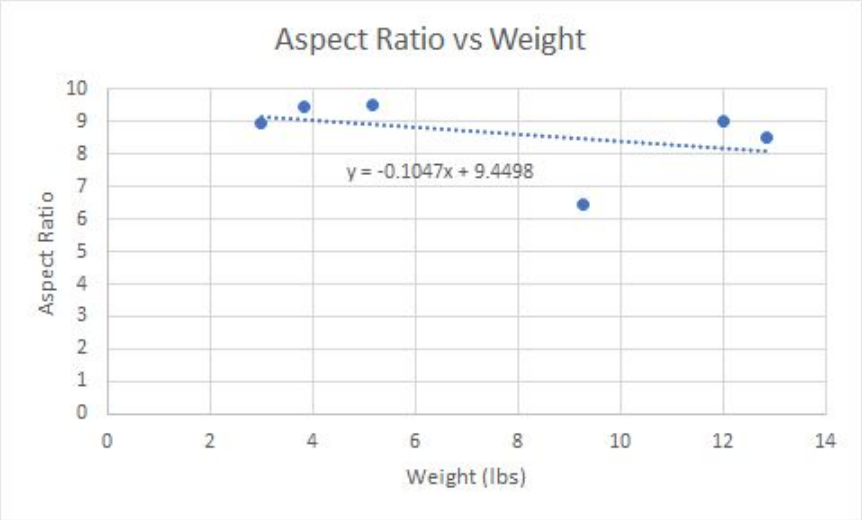

Figure 8: Aspect Ratio vs Weight Trade Study

Based on this graph, aspect ratios are relatively constant over various weights, with one outlier, the 2016 Fixed Wing MQP (*see* Smith et al, 2016). This fixed wing was tasked with a significantly different mission than our aircraft. Plotting our aircraft onto this trend, our aspect ratio comes out to 8.76. Aspect ratio is defined as follows:

$$AR = \frac{b^2}{S} \qquad (1)$$

Where AR is the wing aspect ratio, b is the wingspan, and S is the wing area. The final trade study we conducted was for wing loading. This study can be seen in Fig. 9.

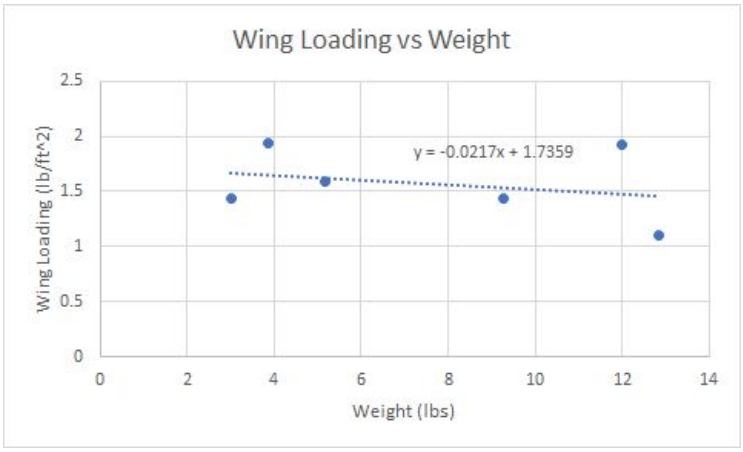

Figure 9: Wing Loading vs Weight Trade Study

From this plot, wing loading for past MQP planes have been relatively constant, regardless of weight, ranging between 1.1 and 1.94 $\frac{lbs}{ft^2}$. Wing loading is defined as:

$$wing\ loading\ =\ \frac{W}{S} \qquad (2)$$

Where W is the aircraft weight. Placing our plane into this model results in a wing loading of 1.5927 $\frac{lbs}{ft^2}$, which will be important in the wing sizing analysis done in Section 3.2.2.

3.2.2 Initial Wing Sizing

From the wing loading value found from the third trade study in Section 3.2.1, we were able to determine the wing area required to support our aircraft by rearranging Eqn. 2. We found the value for wing area to be 4.14 ft^2. This result and a rearrangement of Eqn. 2 yield a wingspan of 6.02 ft.

Another value that is helpful to get an idea of the overall shape of the wing is the taper ratio, defined as:

$$\lambda = \frac{c_{tip}}{c_{root}} \qquad (3)$$

Where c_{tip} is the chord length at the wingtip and c_{root} is the chord length at the wing root. Based on our literature review, we settled for an aspect ratio of 0.45 for our wing. By manipulating Eqns. 1 and 3, the aspect ratio gives us a root chord of 0.9487 ft and a tip chord of 0.4269 ft. An analysis into taper ratio will be presented in Section 4.1.1.

From taper ratio, we are able to determine the mean aerodynamic chord, a value that is widely used throughout calculations for aerodynamics and stability. The mean aerodynamic chord $\bar{c}$ is found by the following equation:

$$\bar{c} = \frac{2}{3} c_{root} \frac{(1+\lambda+\lambda^2)}{(1+\lambda)} \qquad (4)$$

The mean aerodynamic chord comes out to 0.72 ft. For reference, a wing platform was drawn using SolidWorks, and is displayed below in Fig. 10.

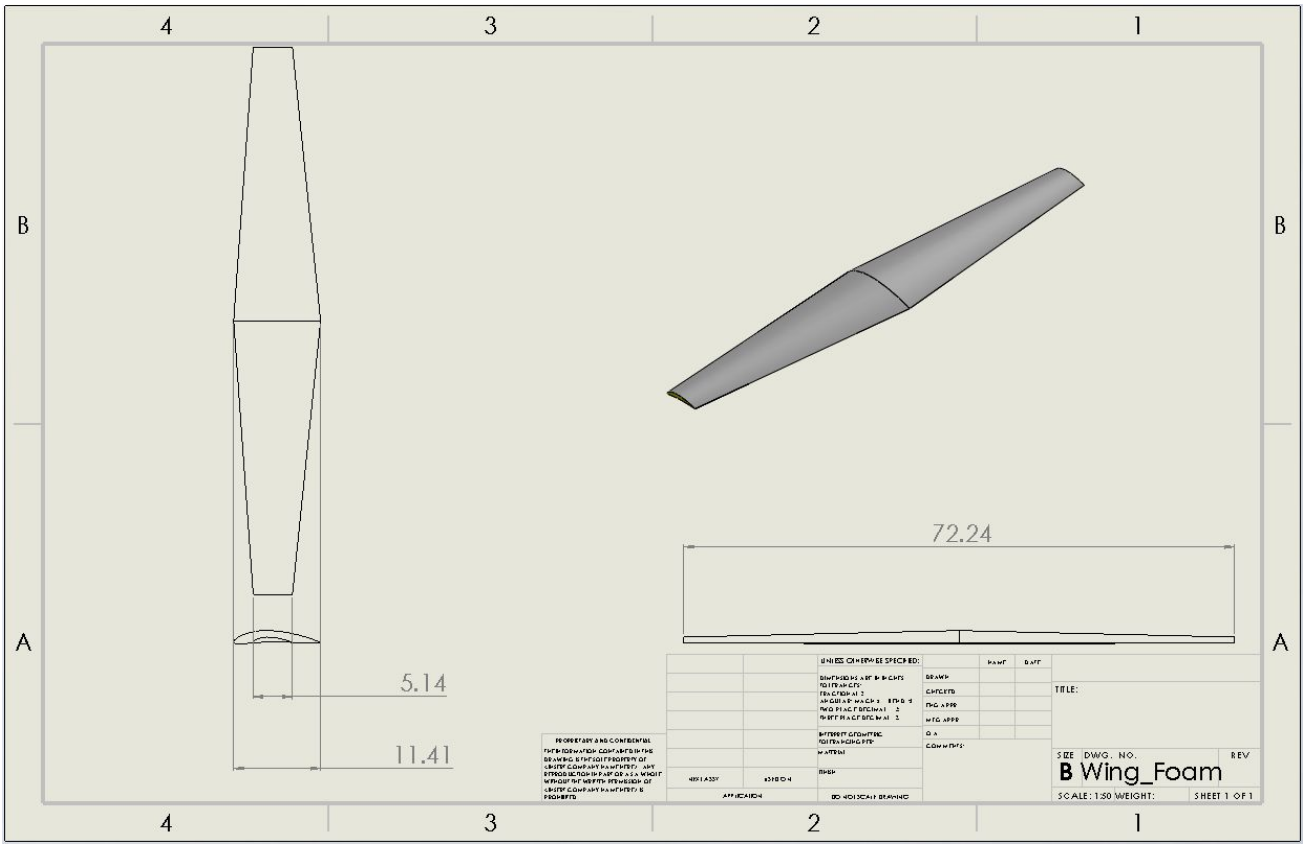

Figure 10: Wing Platform Shape (units are in inches)

Other considerations for the wing design will be discussed in detail in Sec. 4.1, including airfoil selection, taper ratio, dihedral, and winglets, as well as some considerations of revised wing sizing.

3.2.3 Initial Tail Sizing

In order to obtain a general size for the tail surfaces of the aircraft, we used the method of tail volume coefficients. The tail volume coefficients, both for vertical and horizontal tail components, take into account historical data and present a ratio of wing to tail area, scaled by the moment arm.

The first tail surface that we sized was the horizontal tail surface. From the tables of typical values contained in Raymer (2018), we obtained the horizontal tail volume coefficient c_{HT}, to be 0.50. Then using Eqn. 5 below, we obtain S_{HT}, which is the horizontal tail area.

$$S_{HT} = \frac{c_{HT}\bar{c}\,S}{L_{HT}} \qquad (5)$$

Where L_{HT} is the moment arm between quarter chords of the wing and horizontal tail. Using our wing area of 4.14 ft^2, mean aerodynamic chord of 0.72 ft, and a moment arm assumed to be 3 ft (based on estimated overall length), we find the horizontal tail area to be 0.4978 ft^2.

The same general process was applied to the vertical tail coefficient, though the formula to obtain the vertical tail area is slightly different. From Raymer (2018), we found the vertical tail volume coefficient c_{VT} to be 0.04. Using Eqn. 6 we obtained S_{VT}, the vertical tail area.

$$S_{VT} = \frac{c_{VT}b\,S}{L_{VT}} \qquad (6)$$

Where L_{VT} is the moment arm between quarter chords of the wing and vertical tail. Using the wing area of 4.14 ft^2 , wingspan of 6.02 ft, and again assuming a moment arm of 3 ft, we find a vertical tail area of 0.3329 ft^2 .

The next step in sizing the tail surfaces was to figure out what type of aspect ratios and taper ratios that were ideal. According to Raymer (2018), we need to keep our surfaces in accordance with the parameters tabulated below:

Variable	Corresponding Parameter	Value Range
AR_{HT}	Horizontal Tail Aspect Ratio	3-5
AR_{VT}	Vertical Tail Aspect Ratio	1.3-2.0
λ_{HT}	Horizontal Tail Taper Ratio	0.3-0.6
λ_{VT}	Vertical Tail Taper Ratio	0.3-0.6

Table 7: Tail Parameter Ranges

From this table, we selected the following values for our tail sections, tabulated below:

Variable	Value
AR_{HT}	4
AR_{VT}	1.5
λ_{HT}	0.5
λ_{VT}	0.5

Table 8: Selected Tail Values

Eqns. 1 and 2 in Sections 3.2.1 and 3.2.2 above can be used to determine the following parameters:

Variable	Corresponding Parameter	Value
b_{HT}	Horizontal Tail Span	1.411 ft
b_{VT}	Vertical Tail Height	0.7066 ft
$c_{HT,\,root}$	Horizontal Tail Root Chord	0.4704 ft
$c_{HT,\,tip}$	Horizontal Tail Tip Chord	0.2352 ft
$c_{VT,\,root}$	Vertical Tail Root Chord	0.6281 ft
$c_{VT,\,tip}$	Vertical Tail Tip Chord	0.3140 ft

Table 9: Calculated Tail Measurements

These parameters were used to create drawings of the horizontal and vertical tails in SolidWorks, displayed in Figs. 11 and 12 below, respectively.

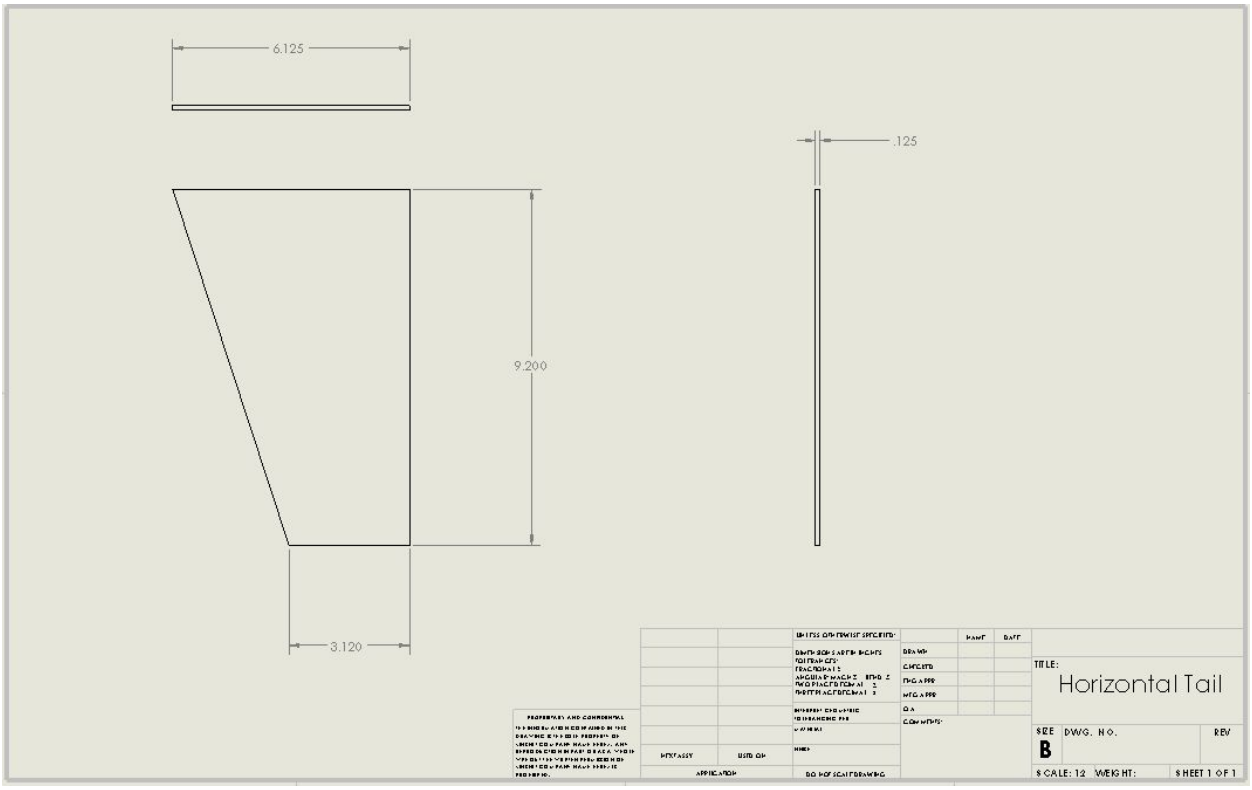

Figure 11: Horizontal Tail Platform

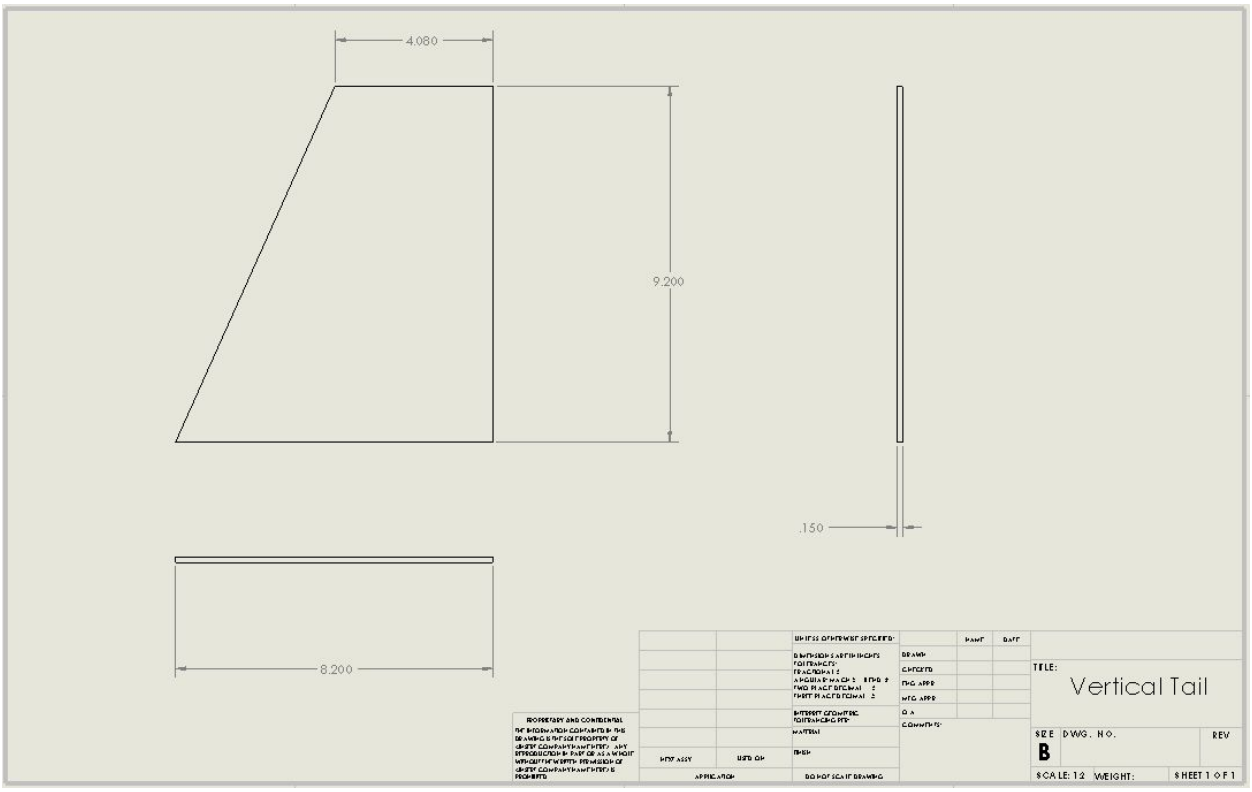

Figure 12: Vertical Tail Platform

3.3 Scoring Breakdown

One of the first tasks in designing our aircraft was to analyze the rules and determine which aspects the final score is most sensitive to. With this information we determined which design choices would best optimize our design. This scoring equation weights components of payload capacity, range, payload drop accuracy, autonomy, and originality in order to produce a total score. Both fixed-wing MQP teams, as well as the VTOL MQP team are scored using the same criteria and the same scoring equation. This scoring equation is as follows:

$$S = \lambda_1 \frac{W_{payload}}{W_{empty}} t_{flight} v_{avg} + \lambda_2 \Delta + \lambda_3 \sum_n A_n + P \qquad (7)$$

Where S is the total score, λ is a multiplier where $\lambda_1 = 0.01, \lambda_2 = \lambda_3 = 35$, $W_{payload}$ is the payload weight carried throughout the duration of the flight, W_{empty} is the aircraft empty weight, t_{flight} is the aircraft flight time in seconds, v_{avg} is the average ground speed of the aircraft in meters per second, and P is a score 0-10 for originality. Δ is a multiplier for payload drop defined as:

$$\begin{aligned} \Delta &= 1, && 0 < \delta < 1 \\ \Delta &= 0, && 1 \leq \delta < 3.5 \\ \Delta &= -1, && 3.5 < \delta \end{aligned} \qquad (8)$$

Where δ is the distance from the spot that the payload lands, to the target. A_n refers to autonomy points. A_1 is given 1 point, dedicated to implementation of an autopilot. A_2 is also given 1 point, dedicated to demonstration of a waypoint guidance system. A_3 is given 3 points for demonstration of a no-fly-zone avoidance system. A_4 is given 5 points for visual target detection. A_5 is allocated 1 point for automated payload drop.

From this scoring equation, we decided to maximize the range of our aircraft. This decision allowed us to design our aircraft, and retrofit autonomous control to the functioning aircraft design at a later stage. After all, if we never get off the ground, we cannot get a score for autonomy. As for the payload drop accuracy, we decided that we would be careful in designing our drop mechanism to be as simple as possible and to have a quick release. However, the only part of the payload drop that affected our conceptual design was that we would need to fly low and slow to have an accurate payload drop.

To be able to determine what we can expect for a score, we found an equation for endurance (*see* Traub, 2011). This equation is given below as Eqn 9.

$$t = Rt^{1-n}\left[\frac{_{total}V*C}{\frac{1}{2}U^3SC_{D0}+(2W^2k/\rho US)}\right]^n \qquad (9)$$

In this equation, t is the endurance in hours, Rt is the battery hour rating, n is a discharge coefficient based on the type of battery and thermal effects, $_{total}$ is the overall propulsion system efficiency, V is voltage, C is battery capacity, U is velocity, S is the wing area, C_{D0} is the coefficient of drag at zero degrees angle of attack, W is the aircraft weight, ρ is the density of air, and k is the lift induced drag factor, defined as it appears in Raymer's (2018) textbook:

$$k = \frac{1}{\pi*AR*e_o} \qquad (10)$$

Where AR is the wing aspect ratio and e_o is the Oswald efficiency of the wing. When Eqn. 8 is multiplied by velocity, we obtain a range. Assuming the conditions in Tbl. 9, our expected range from Traub's equation (2011) gives us the following plot:

Variable	Value
Rt	1 h
n	1.3
$_{total}$	0.5
V	11.1 V
C	2.2 Ah
S	0.3846
C_{D0}	0.03
W	29.43 N
ρ	1.225 $\frac{kg}{m^3}$

AR	8.76
e_o	0.75

Table 10: Range Analysis Parameters

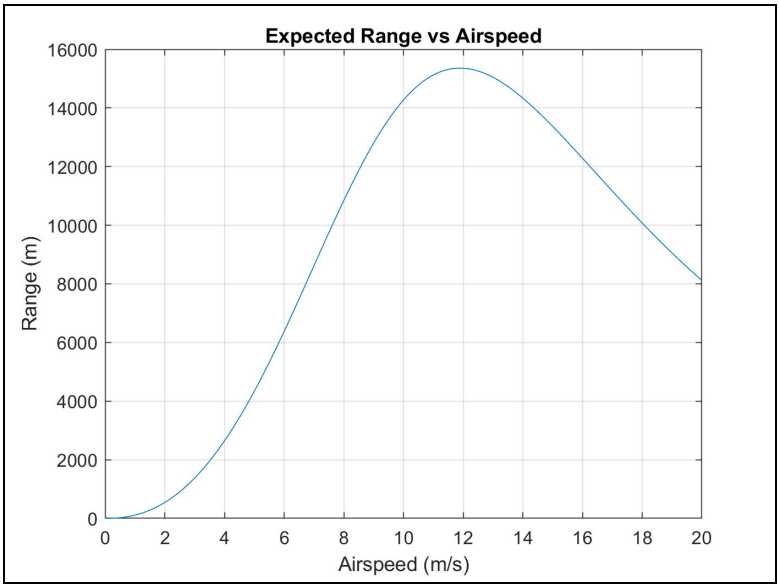

Figure 13: Expected Range vs Airspeed

Values for *Rt*, *n* and $_{total}$ were assumed based on the examples given in Traub's article (*see* Traub, 2011). The associated MATLAB script that was used to develop Fig. 13 can be found in Appendix A. From this plot we were able to determine that at full weight, our aircraft would be expected to have a maximum range of 15,359 meters (9.54 miles) at an airspeed of 11.89 m/s (39 ft/s) with an expected flight time of 21.53 minutes. To keep our assumptions conservative, we assumed that we would fly slightly faster than optimum, which gives our aircraft the opportunity to generate slightly more lift than our estimates indicate that we need. We assumed that we would fly at 12.8 m/s (42 ft/s), which gives a range of 15,148 meters (9.41 miles) with an expected flight time of 19.72 minutes. The overall range is decreased by 1.4% at this faster airspeed, which is a small tradeoff for the additional safety provided by the additional lift.

The non-monotonic behavior of the curve in Fig. 13 is primarily a result of drag. At low airspeeds, higher angles of attack are required to maintain lift, which reduce aerodynamic efficiency. In this analysis, this increased drag due to lift at lower speeds is taken into account by the lift induced drag factor, k, in the denominator of Eqn. 9, which reduces endurance and therefore range. As airspeed increases to an optimal condition, only a small angle of attack is required, reducing drag greatly. In Eqn. 9, the increased velocity, U, causes the effect of the lift induced drag factor to be reduced. As airspeed increases beyond this optimal condition, drag once again begins to increase. This is a result of the square relation between velocity and drag. In Eqn 9, this is captured where U is cubed in the denominator. This also reduces range in this analysis.

We also calculated a score from the range component of the scoring equation from the use of the range equation by applying the first term of Eqn. 6 and subbing in the range found in Fig. 13. A plot of projected range score is presented in Fig. 14.

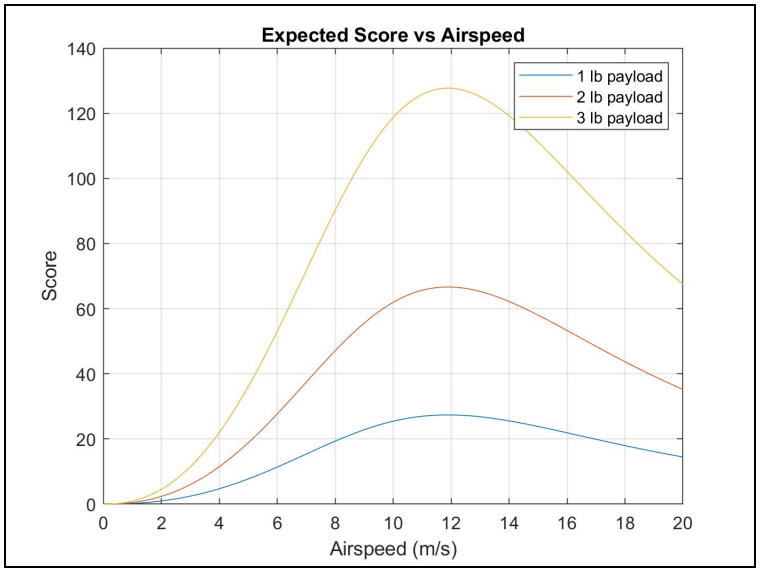

Figure 14: Expected Score vs Airspeed

In Fig. 14, it is assumed that our MAV is flying at the full 3 kg (6.61 lb) gross weight, varying payload to empty weight ratios. As seen in the plot, for a given gross weight, it is advisable to carry a higher percentage of the MAV's weight in payload, as the airspeed for maximum score is constant, and is not significantly affected by the payload fraction.

An analysis was also conducted to see if flying under the maximum allowable weight is advisable or provides any benefit. A plot of score vs airspeed for a set empty weight of 3.61 lbs is displayed in Fig. 15.

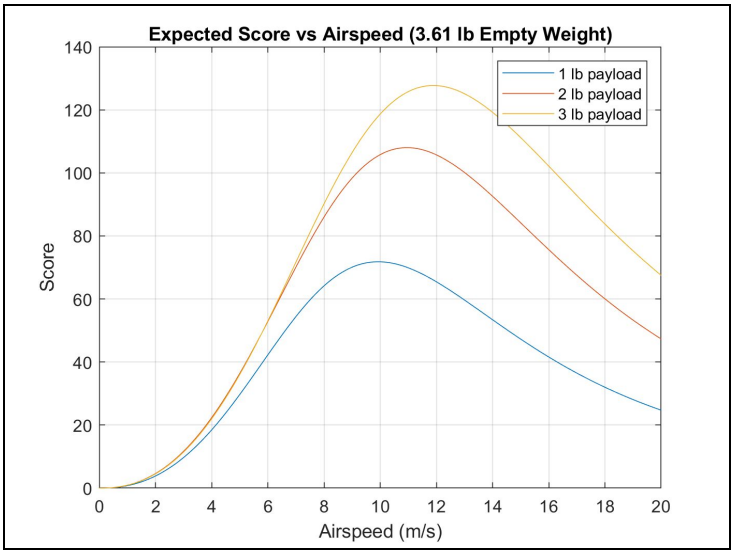

Figure 15: Expected Score vs Airspeed (3.61 lb Empty Weight)

This plot reveals that it is beneficial to carry more payload for a given empty weight. The only trade-off for carrying more weight is that the airspeed needed to maximize score increases as the gross weight increases. Further investigation into the cause of this trade-off leads to the result displayed in the range vs airspeed plot seen in Fig 16 below. To carry less payload leads to a lower gross weight and allows for a longer range for a given empty weight. The plot also displays that the maximum range for lower payloads occurs as lower airspeeds, corresponding with the lower lift required to maintain steady level flight.

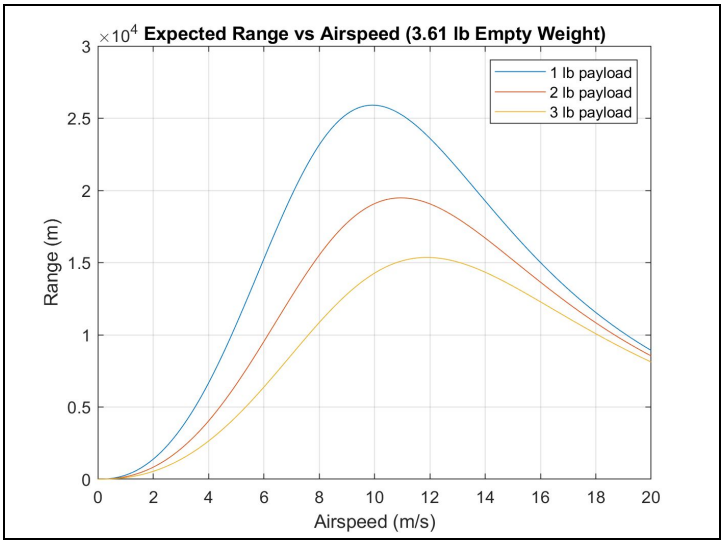

Figure 16: Expected Range vs Airspeed (3.61 lb Empty Weight)

From analysis of the plots in this section, we decided to make an empty weight of 4.61 lbs our target for empty weight. This would allow for 2 lbs of payload to be carried during our flight. With the range projected for our aircraft at the full 6.61 lb gross weight, this would give us a score of 65.7 points from range at our target airspeed of 42 ft/s. Obviously, any weight savings that can be made during the design of the aircraft will result in an increased payload capacity and a higher range score.

4.0 Detailed Design

This section provides a detailed analysis of all major design decisions made in the creation of our aircraft. Subsections will discuss the aerodynamic, structural, propulsion, and controls related issues related to the project. Each section will describe each design iteration (if applicable) and decisions and logic associated with redesign efforts.

4.1 Aerodynamic Analysis

After obtaining a wing area and cruise speed, as well as some basic dimensions of the wing, we were able to proceed with picking an airfoil capable of generating enough lift for our aircraft. In designing a suitable wing, we utilized an open-source computational fluid dynamics (CFD) software known as XFLR5 to iterate through possible airfoil designs, looking for lift coefficients and the angle of attack at which they occur. From these results, we selected an airfoil for our application. XFLR5 primarily uses vortex-lattice methods to perform its calculations and is used to analyze airfoils for model aircraft at low Reynolds numbers (*see* XFLR5, 2009).

4.1.1 Airfoil Selection

The first step we took in determining what airfoil we would use in our design was to establish what coefficient of lift is required given our airspeed and wing area. To calculate coefficient of lift, we used the following equation:

$$Cl_{req} = \frac{W}{\frac{1}{2}\rho U^2 S}\left(1 + \frac{2}{AR}\right) \qquad (11)$$

Use of Eqn. 11 yields a value of 0.95 as a coefficient of lift at cruise. Another important value to consider was the Reynold's number over the wing. Reynold's number is defined by Eqn. 12.

$$Re = \frac{\rho U \bar{c}}{\mu} \qquad (12)$$

Where μ is the dynamic viscosity of air. Calculating the Reynold's number for our wing yields a value of 190,000. The XFLR5 program that we used is also very particular about making sure that Reynolds numbers are defined for a full range of values corresponding to different chord lengths at different spanwise locations on the wing. In order to accommodate the program, we calculated the Reynolds numbers over the root and tip of the wing by substituting the values for root and tip chord. The Reynolds number at the wing root comes out to 250,000 and 112,000 at the wing tip for the 0.45 taper ratio case.

When looking for an airfoil, we looked for a high lift, thin airfoil that adheres to the rule of thumb not to exceed 3 degrees angle of attack (AoA) on the wing at the cruise condition. Several airfoils were investigated in the 2D case. Of these, the NACA 6412, NACA 7412, and NACA 8412 performed the most favorably. Each airfoil was iterated over a range of Reynold's numbers and angles of attack: from Reynold's numbers of 100,000 to 300,000, and from angles of attack of -10 degrees to 20 degrees. The AoA needed to achieve the required coefficients of lift from this 2D analysis are displayed in Table 11.

	NACA 6412	NACA 7412	NACA 8412
AOA for Cl_{req} (2D)	2.5 degrees	1.5 degrees	0.5 degrees

Table 11: 2D Airfoil Analysis Summary

The first airfoil we will discuss is the NACA 6412, which has a spline displayed in Fig. 17a. The NACA 6412 airfoil was able to generate the required 0.95 coefficient of lift at approximately 2.5 degrees angle of attack. This value fits inside the envelope of angle of attack that we were looking for, albeit very narrowly.

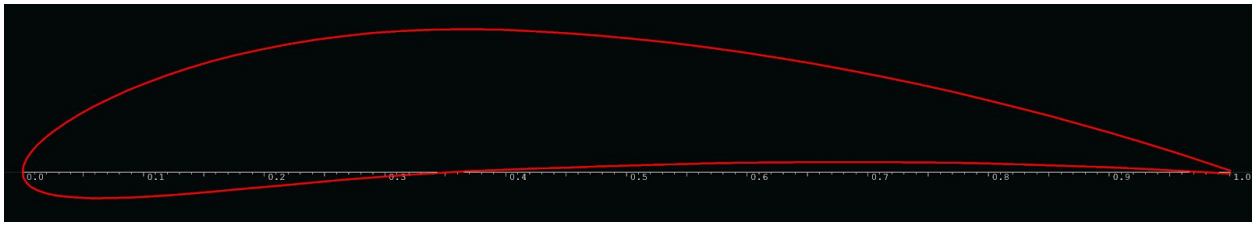

Figure 17a: NACA 6412 Spline

Initial suspicions were that the NACA 6412 would not be able to retain its lift curve in 3D analysis. This will be discussed further later in this section. A lift curve plot generated by XFLR5 for the NACA 6412 is displayed below as Fig. 17b.

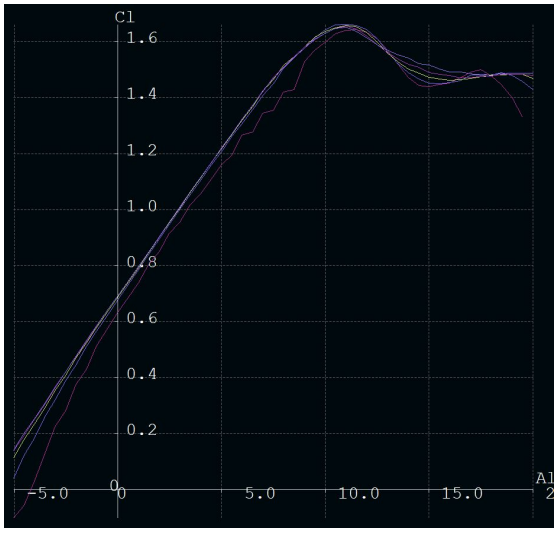

Figure 17b: 2D Lift Curve NACA 6412
Coefficient of Lift (y axis) vs Angle of Attack in degrees (x axis)

The second airfoil that fit the required parameters was the NACA 7412. This airfoil has the same maximum thickness and same location of maximum thickness, but a higher camber

than that of the NACA 6412. A spline of this airfoil is displayed below in Fig. 18a. The NACA 7412 airfoil was able to generate the required 0.95 coefficient of lift at approximately 1.5 degrees angle of attack. This value fits comfortably within the envelope that we wished to achieve.

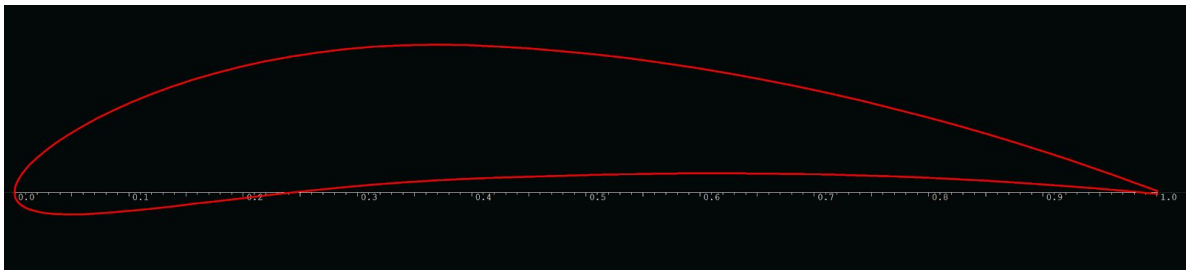

Figure 18a: NACA 7412 Spline

A plot generated in XFLR5 is displayed below as Fig. 18b. The scatter seen in this plot is a result of convergence issues with the program at lower Reynolds Numbers. The program initializes the boundary layer only after failed convergence of the iterative scheme, rather than computing the boundary layer before every calculation (*see* XFLR5, 2009). This issue is one significant reason why wind tunnel tests are required to confirm the theoretical results from XFLR5.

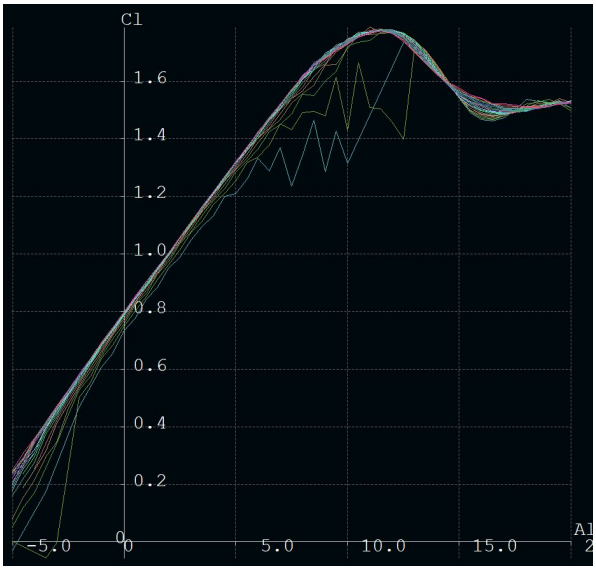

Figure 18b: 2D Lift Curve NACA 7412
Coefficient of Lift (y axis) vs Angle of Attack in degrees (x axis)

The final airfoil that we will present is the NACA 8412, which has a higher camber than the NACA 7412. A spline of this foil is displayed in Fig. 19a. The NACA 8412 airfoil was able to generate the required 0.95 coefficient of lift at approximately 0.5 degrees angle of attack. This value fits comfortably within the envelope that we wished to achieve.

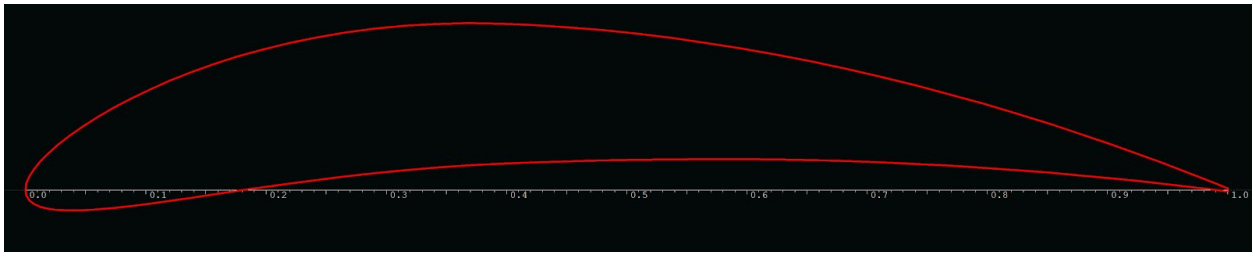

Figure 19a: NACA 8412 Spline

A plot generated in XFLR5 is displayed below as Fig. 19b. In this plot, Reynolds Number increases from the bottom line to the top line.

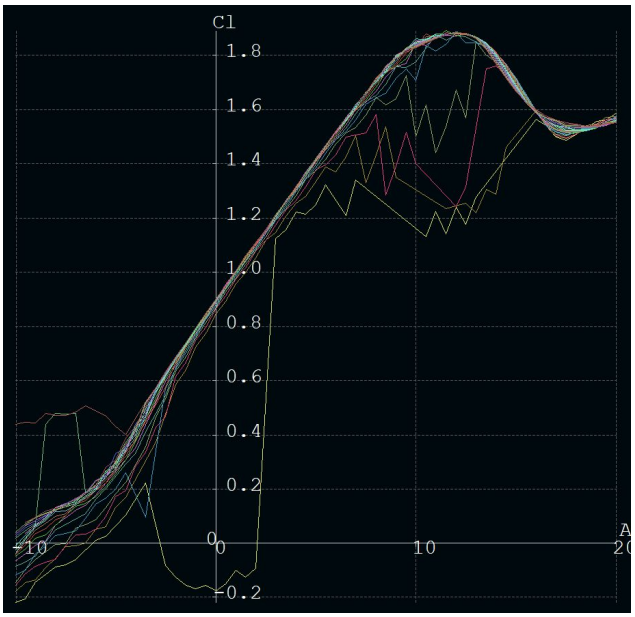

Figure 19b: 2D Lift Curve NACA 8412
Coefficient of Lift (y axis) vs Angle of Attack in degrees (x axis)

The purpose of the 2D analysis was to narrow down the set of airfoils to process in the 3D plane analysis that XFLR5 provides, which takes into account wing geometry and spanwise

aerodynamic effects on the wing. This feature requires the user to define several more dimensions, including the chord lengths at various locations, spanwise offsets, and mesh size, depending on the selected analysis method in order to get output, and is therefore much more time consuming than the 2D analysis presented above. However, the 3D analysis is able to take into account spanwise lift distribution and wing tip effects that the 2D analysis is unable to capture. As a result, the lift curves that the 3D analysis provides are lower than those of their 2D analogs, and the drag curves are more physically meaningful.

Each airfoil was run through three wing platform designs, corresponding to a taper ratio of 0.45, 0.67, and 1.00. Below, models of the NACA 8412 are displayed as Figs. 20, 21, and 22, corresponding to 0.45, 0.67 and 1.00 taper ratios respectively. The platforms for the other two airfoils look very similar to the ones presented below and for the sake of brevity, have not been included.

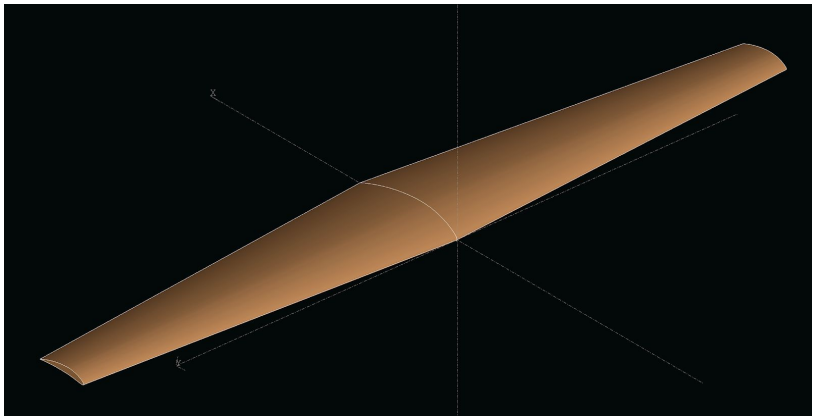

Figure 20: NACA 8412 0.45 Taper Ratio

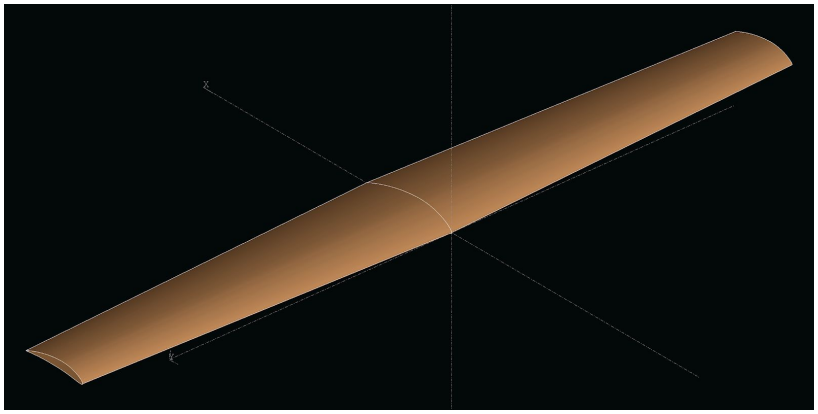

Figure 21: NACA 8412 0.67 Taper Ratio

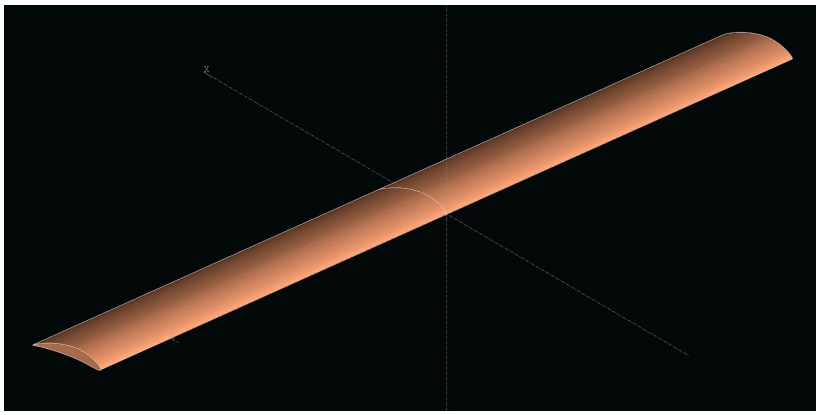

Figure 22: NACA 8412 No Taper

The NACA 8412, which ended up being our selected airfoil, reached the 0.95 coefficient of lift required to maintain steady level flight was met at an angle of attack of about 2.65 degrees, again for the 0.45 taper ratio case. At the cruise angle of attack, the coefficient of drag we would encounter would be 0.0495, slightly higher than the other two options, but not significant enough to override the angle of attack concern. This corresponds to a lift-to-drag ratio of 19.2, which is 97% of the maximum lift to drag, which occurs at about 1 degree angle of attack. The lift curve, with all three designs plotted together in Fig. 23. The top line, seen in red, corresponds to the 0.45 taper case and crosses the 0.95 Cl threshold at 2.65 degree AoA. The middle line in green is the 0.67 taper case and the lowest line in purple is the wing without a taper, crossing 0.95 Cl at

an AoA of 3.0 degrees. This analysis would not converge over a 15 degrees angle of attack, so the stall conditions were not well documented. Regardless, in our application, we do not anticipate a need to exceed 15 degrees angle of attack on the wing, which would correspond to about 12.5 degrees nose up.

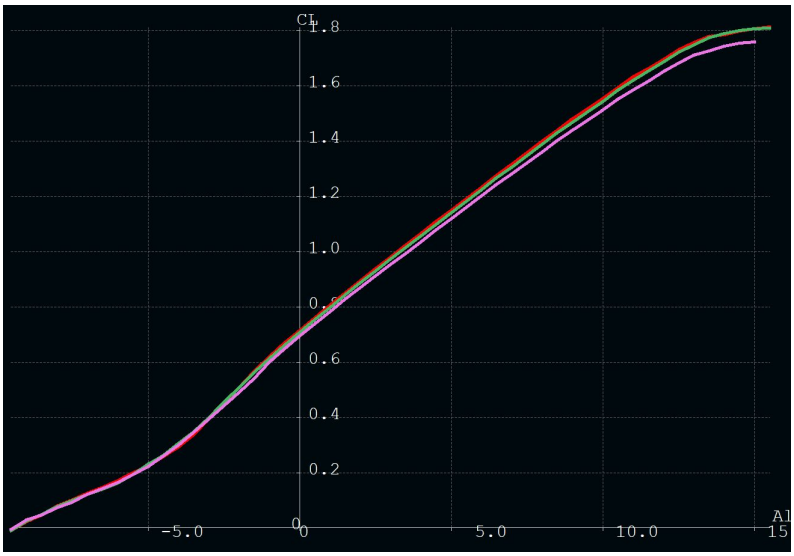

Figure 23: NACA 8412 3D Lift Curve
Coefficient of Lift (y axis) vs Angle of Attack in degrees (x axis)

The drag plot in Fig. 24 also confirms the added efficiency of the 0.45 taper ratio, with the most drag being produced by the taperless wing.

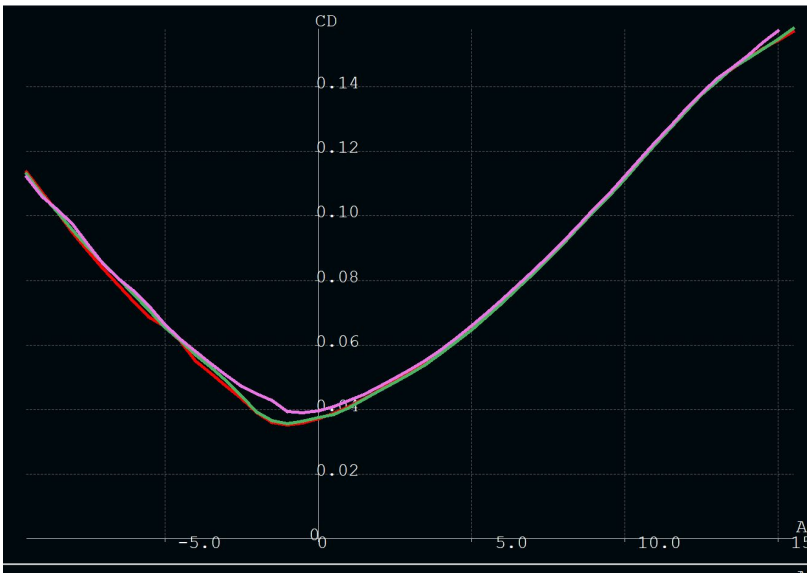

Figure 24: NACA 8412 3D Drag Curve

Coefficient of Drag (y axis) vs Angle of Attack in Degrees (x axis)

The lift-to-drag plot was also found, and can be seen as Fig. 25 below.

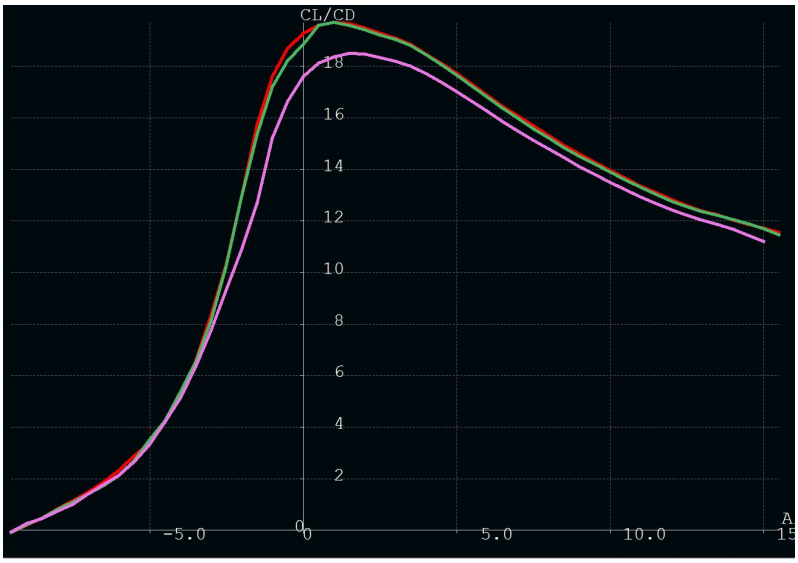

Figure 25: NACA 8412 3D Lift/Drag
CL/CD (y axis) vs Angle of Attack in Degrees (x axis)

The summary table, Tbl. 12, shows all the parameters that were analyzed for all three airfoils. It is clear that the angles of attack required for the NACA 6412 and 7412 to generate enough lift to maintain level flight are much higher than the angle required for the NACA 8412. The NACA 8412 is the only foil not to violate the rule of thumb of not exceeding 3 degrees angle of attack at cruise. Violation of this rule of thumb leads to issues with aerodynamic moments being too high and causing stability issues. The only notable tradeoff that is experienced with the NACA 8412 is a 4% increase in drag. This trade off is something that will have to be compensated by the engine selection, as a lower cambered airfoil with less drag will lead to stability issues (*see* Raymer, 2012).

	NACA 6412	NACA 7412	NACA 8412
AOA for Req. CL (0.45 taper)	4.60 deg	3.65 deg	2.65 deg

AOA for Req. CL (0.67 taper)	4.70 deg	3.75 deg	2.75 deg
AOA for Req. CL (no taper)	4.90 deg	4.00 deg	3.00 deg
CD at trim AOA	0.0475	0.0475	0.0495
L/D at trim AOA	20.1	20.1	19.2
% of Max L/D	90%	96%	97%

Table 12: 3D Airfoil Analysis Summary

Validation of the analysis conducted on the NACA 8412 will be shown through a wind tunnel test presented in Section 5.1.

4.1.2 Tail Airfoil

We also decided to add an airfoil to the tail surfaces. Typical airfoils for tail surfaces are very thin and symmetric. As a result, we decided to use a NACA 0008. The only result that we require out of XFLR5 for this airfoil is a lift curve slope, which comes out to 5.27 rad^{-1}. A plot of this lift curve slope is displayed as Fig. 26 below. High angles of attack will not be necessary in our application, so the XFLR5 convergence issues above 9 degrees angle of attack do not present a large concern.

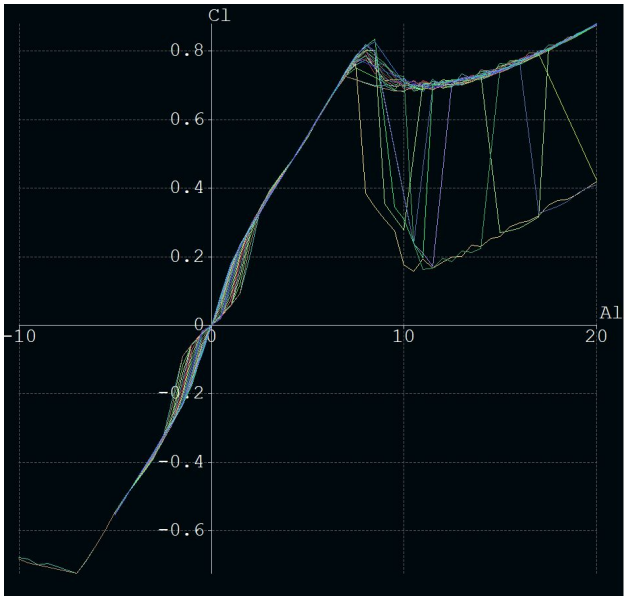

Figure 26: NACA 0008 2D Lift Curve
Coefficient of Lift (y axis) vs Angle of Attack in Degrees (x axis)

4.1.3 Wing Features

After selecting an airfoil and wing shape, we looked into adding a dihedral to our wing and/or winglets. These wing features were modeled in XFLR5, however, did not display any differences in lift to drag ratio from a featureless wing of the same aspect ratio and taper. Upon further investigation and reading into the XFLR5 documentation, we discovered that XFLR5 is incapable of modeling these features and will disregard them. Regardless, we have included the models made in XFLR5 for these design considerations, and will discuss both dihedrals and winglets as they apply to our aircraft. We will discuss the benefits and drawbacks of each and give a rationale for our design decisions.

The first feature we examined was the dihedral. A dihedral wing is intended to add roll stability to an aircraft. A high wing design typically has a dihedral angle of between 0 and 2 degrees (*see* Raymer, 2018). High wing aircraft have an inherent dihedral effect that other configurations do not, which factored into our decision. Raymer (2018) also warns that if the

dihedral angle is too large, that Dutch Roll can become an issue. Our take on the dihedral was that its inclusion would result in an increased complexity in terms of mounting the wings to the fuselage, having to be able to measure a shallow angle rather than just making sure that our wings were level. An XFLR5 model of a 2 degree wing dihedral is displayed below as Fig. 27.

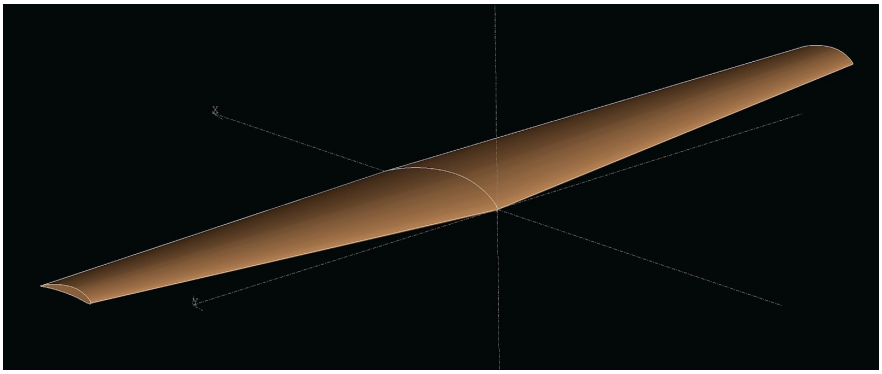

Figure 27: NACA 8412 2 Degree Dihedral

The other feature considered was the addition of winglets. Winglets are intended to decrease wingtip vortices, thus increasing lift and decreasing drag. According to Raymer, winglets act to increase the "effective span" of the wing, however if the wing is already efficient, the benefit of the winglet could be negligible (*see* Raymer, 2018). An added risk is that if the winglet is not properly designed, it can add weight and contribute to flutter in the wing, which would end up decreasing the efficiency of the wing and add structural concerns. Our group is not confident that we would be able to design a winglet that would be of a high enough quality that it would benefit our design. Also, looking into past MQP reports, we saw no instances where a winglet was implemented. As a result, we decided to exclude consideration of a winglet from our aircraft design. A model of a wing platform with a winglet is displayed below as Fig. 28.

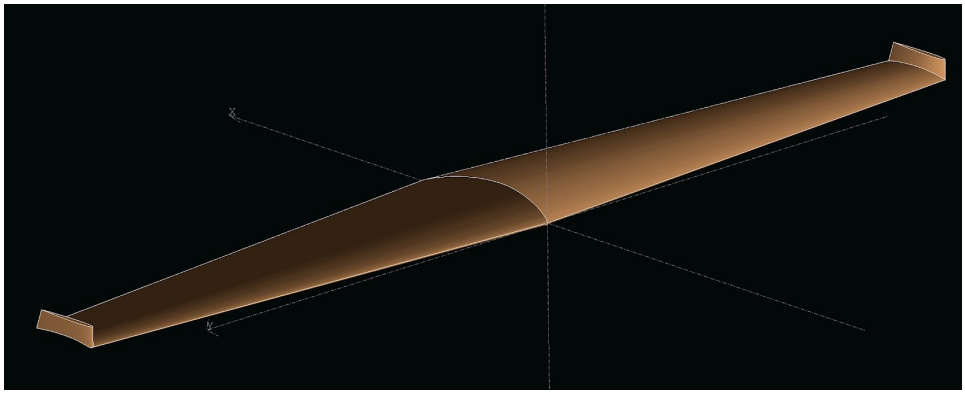

Figure 28: NACA 8412 With Winglets

4.1.4 Wing Loading

To be able to better understand the size of our main wing that is needed to maintain flight at various conditions, a critical component to analyze is the wing loading. In this analysis, conditions of cruise, loiter, and stall were taken into account. These values for wing loading at each condition were used to ensure that the aircraft's wings have a proper amount of area to maintain lift through all phases of flight. Our initial wing sizing was also done performing a wing loading analysis using historical data, so this new analysis will need to be compared to the original analysis in order to make a decision as to which most accurately fits our application.

At the cruise condition for propeller craft, wing loading is given by the following equation in Raymer (2018):

$$\frac{W}{S} = \frac{1}{2}\,\rho U_{cruise}^2 \sqrt{C_{D,0}\,\pi\,AR\,e_0} \qquad (13)$$

Where $C_{D,0}$ is the drag coefficient, assumed 0.015, and e_0 is the Oswald efficiency, calculated with the following equation:

$$e_0 = 1.78(1 - 0.045(AR)^{0.68}) - 0.64 \qquad (14)$$

The value found for Oswald efficiency was 0.7897 from Eqn. 14 and the value for wing loading at cruise out of Eqn. 13 was 1.1795 $\frac{lbs}{ft^2}$.

For the loiter condition, Raymer (2018) gives the following equation:

$$\frac{W}{S} = \frac{1}{2}\,\rho U_{cruise}^2 \sqrt{3\,C_{D,0}\,\pi\,AR\,e_0} \qquad (15)$$

Eqn. 15 yields a wing loading of 2.049 $\frac{lbs}{ft^2}$.

For the stall condition, we first had to determine the stall speed of our aircraft. In order to find this, we utilized an equation for stall speed displayed in Eqn. 16.

$$V_{stall} = \sqrt{\frac{2W}{\rho S Cl_{max}}} \qquad (16)$$

Where Cl_{max} was the maximum coefficient of lift, in our application, this value was 1.8. Using Eqn. 16, we found that the stall speed was 27.5 ft/s. Then to find the wing loading at stall, we applied the following equation from Raymer (2018):

$$\frac{W}{S} = \frac{1}{2}\,\rho U_{cruise}^2 Cl_{max} \qquad (17)$$

Evaluation of this equation yields a value of 1.5927 $\frac{lbs}{ft^2}$ at the stall condition. As the stall condition is not the limiting factor for wing loading, we do not need to add flaps in order to land properly. However, we do wish to be able to fly as slow as possible during our payload drop section of our flight. This feature will be implemented in order to give the pilot as much lift as possible at low airspeeds, improving the likelihood of a successful payload drop.

To be able to resize the wing, we took the lowest value of wing loading from the cruise condition and rearranged Eqn. 1 from Section 3.2.1 in order to obtain a new wing area of 5.60

ft^2 . Applying this to our predefined wing shape, with the same aspect ratio and taper ratio, the wingspan increased to 7 ft with a mean aerodynamic chord of 0.84 ft.

It must be noted that these equations presented in Raymer are for a full scale aircraft. As such, we cannot rely blindly on these equations to justify our design. Additionally, we must take into consideration the project requirements. A larger wing would require our empty weight to be higher, which reduces our score, even if it might allow us to carry more payload. A larger wing would also induce more drag, increasing power consumption and reducing range. The final consideration is logistical. Our plan was to affix the wing to the fuselage in order to reduce the assembly required on site on flight day and to provide increased structural strength. In order to transport a wing of greater than 6'2", we would need to be able to seperate the wing off of the fuselage of the aircraft, and likely break it into several pieces for transport. This, coupled with the linear regression for wing loading of past MQP planes gives us confidence that the 6.02 ft wingspan iteration will be sufficient for our design. This 6.02 ft configuration is consistent with the final as-built configuration of the aircraft.

4.1.5 Refined Tail Sizing

After closer inspection of the overall layout of the aircraft, we determined that in order to fit all of the electronics into the fuselage and to place the center of gravity under the wing of the aircraft, that the main wing would need to be pushed back 6". The overall length of the aircraft was unchanged, meaning that the lever arm between the tail and wing was reduced from 3 ft to 2.5 ft. To compensate for this change, both the vertical and horizontal tail sections had to be resized.

The method for resizing the tail sections was unchanged. Eqns. 5 and 6 from Section 3.2.2 were applied once again, using the same tail volume coefficients as before. The only parameter that changed was the denominator of each equation, relating to the lever arm between quarter chords of the main wing and each tail. The tail sections retained the same geometry, just scaled up. A table of the updated tail parameters is presented in Table 13.

Parameter	Preliminary Value	Final Value
Moment Arm	3 (ft)	2.5 (ft)
HT Area	0.4978 (ft^2)	0.60 (ft^2)
HT Span	1.41 (ft)	1.55 (ft)
VT Area	0.3329 (ft^2)	0.40 (ft^2)
VT Height	0.7066 (ft)	0.77 (ft)
HT Root Chord	0.4704 (ft)	0.52 (ft)
HT Tip Chord	0.2352 (ft)	0.26 (ft)
VT Root Chord	0.6281 (ft)	0.69 (ft)
VT Tip Chord	0.3140 (ft)	0.34 (ft)

Table 13: Summary of Refined Tail Dimensions

In addition to resizing the tail, technical difficulties were experienced attempting to cut airfoil shapes for the tails. This difficulty resulted in the decision to abandon the airfoil for the tails and revert to the flat plate model. The flat plates roughly approximate the same aerodynamic characteristics of an uncambered thin airfoil, so no additional calculation was required to implement the design change.

4.1.6 Lift to Drag Analysis

To validate the cruise condition found in the scoring analysis found under Section 3.3, a drag buildup model was created. This drag buildup model is a historical model, which is laid out in detail in Raymer (2018). This model includes parameters for drag on the wing, fuselage, and tail. A simplistic model for drag on a rectangular box was also integrated into the Raymer model, as we intend to carry the payload external to the fuselage. The payload drag is modeled by Eqn. 18.

$$D = C_D A \frac{\rho V^2}{2} \qquad (18)$$

Where C_D is the drag coefficient of the rectangular box, which is taken to be 1.05, and A is the cross-sectional area of the payload, estimated as 6 square inches.

The drag produced by this buildup model was iterated for velocities spanning the entirety of our aircraft's flight envelope. This allowed us to compare the drag at each of these velocities to the lift we require to determine the airspeed needed to maximize our aerodynamic efficiency. This drag model will also be used in Section 4.3.3 to aid in motor selection. Fig. 29 displays a plot of lift-to-drag ratio versus airspeeds within the flight envelope.

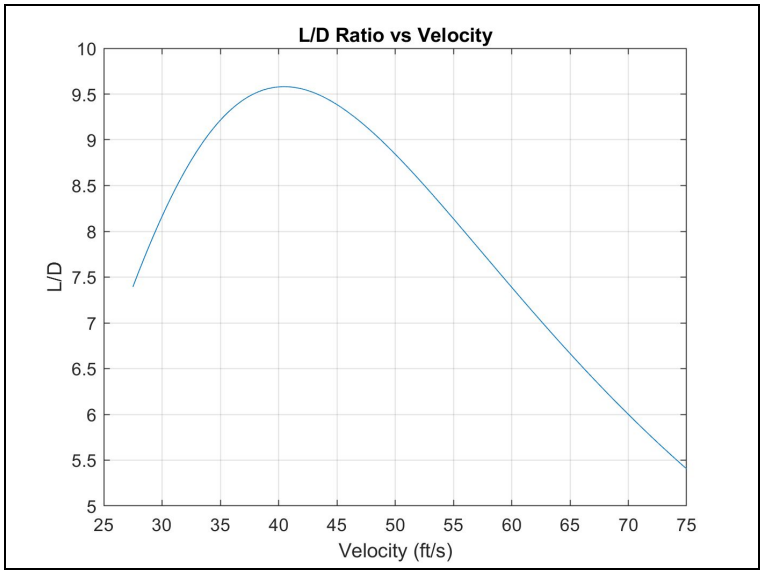

Figure 29: Lift-to-Drag Ratio vs Airspeed

The maximum lift-to-drag ratio for our aircraft is found to be 9.6 and occurs at an airspeed of 41 ft/s. This lift to drag ratio is seperate from the analysis performed solely on airfoils or wing platforms earlier in Section 4 in that this analysis is for the full aircraft and includes features that could not be modeled accurately in XFLR-5. The airspeed calculated as our ideal flight condition matches up well with our previously defined flight condition. This plot also provides qualitative verification of our range and scoring analysis in Section 3.3. Aerodynamic efficiency and range are inherently related. As such, it is logical that the range plot and lift-to-drag plots should follow similar trends.

4.1.7 Turn Radius

One crucial maneuver for any aircraft is the level turn. The main parameter that defines the level turn is the minimum turn radius R_{min}. To calculate this value, 3 load factors need to be determined. These load factors are the lift-limiting load factor, thrust-limiting load factor, and the

structural-limiting load factor. To calculate the lift-limiting load factor, the following Eqn. 19 was used.

$$n_{lift} = \frac{1}{2}\,\rho\, V^2 \frac{Cl_{max}}{\frac{W}{S}} \qquad (19)$$

Likewise, the thrust-limiting load factor was determined using Eqn. 20.

$$n_{thrust} = \sqrt{\frac{\frac{1}{2}\rho V^2}{k * \frac{W}{S}} * \left(\frac{T}{W} - \frac{\frac{1}{2}\rho V^2 C_{d0}}{\frac{W}{S}}\right)} \qquad (20)$$

In this equation, k is a coefficient based on aspect ratio and Oswald efficiency, and $\frac{T}{W}$ is the thrust to weight ratio, which is defined in detail in Section 4.3.3.

The final load factor, $n_{structural}$ requires extensive analysis to arrive at a value. This extensive analysis was beyond our scope and capabilities. However, the structural limit is typically not the quantity that limits the overall turn radius. As such, we found it sufficient to perform a turn radius calculation based on only the lift and thrust limits. A simple validation that the structural limit is not violated is provided through a wing loading analysis. Theoretical results are presented in Section 4.2.2 and experimental results are provided in Section 5.2.

The equation to determine the turn radius for an aircraft at a given airspeed is:

$$R_{min} = \frac{V^2}{g\sqrt{n_{min}-1}} \qquad (21)$$

In this equation, n_{min} indicates the lowest value of load factor. In our application, the lowest value for load factor came out of the thrust, which gave a value of 3.265 G. Iterating this equation over airspeeds within our aircraft's flight envelope produces the following plot.

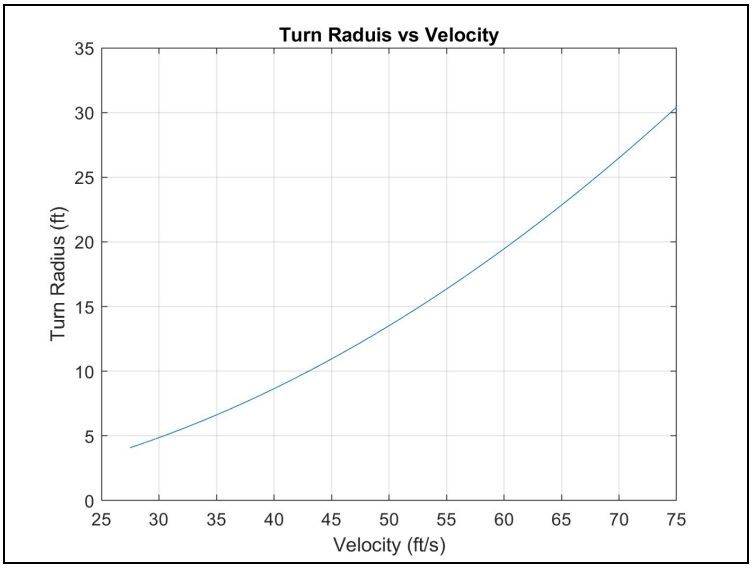

Figure 30: Turn Radius vs. Airspeed

As one would expect based on the equation, the turn radius increases as the airspeed increases. At our cruise condition, our minimum turn radius is 17.62 ft by this calculation. This turn would indicate a very aggressive maneuver, one which our mission profile does not require. This turn radius is more than sufficient to fulfil our design needs.

4.2 Structural Design

The two main fuselages that are used in R/C Airplanes are of circular and square cross-section fuselages. During the beginning of the term the team spent a few weeks trying to decide between these two shapes. Most of the research claimed that circle fuselages were better because they produced less aerodynamic drag, however, we determined that the difference in aerodynamic drag for our purposes was negligible. The team was more concerned about how the different shaped structures would hold up in the event of a crash, and also about the ease of manufacturability between both shapes. Our hypothesis was that the circular fuselage would

maintain its structural integrity better during a crash, but the square fuselage would be easier to construct.

The team constructed test fuselages out of balsa wood in order to test our different designs and manufacturing process. Due to material availability and budgetary constraints, we used a balsa sheet that we found in the Aerospace MQP Lab. Since the balsa sheet we found was not large enough to cut out our full sized fuselage dimensions, our fuselage was scaled down by a factor of three for the purpose of the experiment. This way, the parts were small enough to be cut out from the balsa sheet we obtained from the lab. We also purchased five 3/32 x 3/32 balsa sticks in order to construct the spars of the fuselage. The team constructed four fuselages in total, which took approximately two hours to construct.

The fuselage was made out of three solid shapes that were laser cut from the balsa sheets and the balsa sticks previously mentioned. The pieces were first designed in SolidWorks, then laser cut. In order to use the laser cutter at Foisie Innovation Studios, at least one of the team members present has to be certified in laser cutting. The circular piece, as shown in Fig. 31, has an outer diameter of two inches and an inner diameter of one inch. Likewise, the square piece has an outer width of two inches and an inner width of an inch.

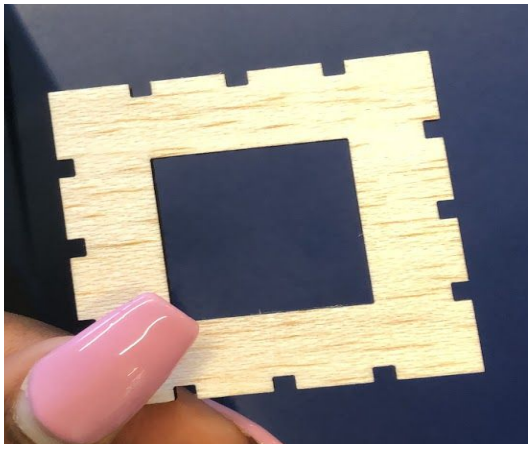

Figure 31: Laser Printed Balsa Square Piece For Fuselage (left) and Balsa Circular Piece Model (right)

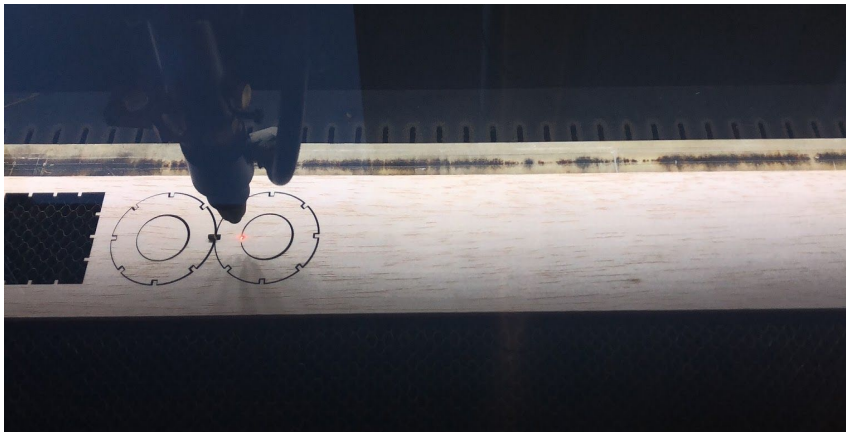

Figure 32: Process of Laser Cutting Circular Fuselage

For the assembly process, we cut the balsa sticks into 6 inch long pieces and glued each piece to the notches in the square and circular pieces. We used two different types of glue for the construction processes. One was the Starbond EM-2000 Thick glue and the other was the Starbond EM-2000 Thin glue. We used both glues in order to test the drying times and see which one the team prefers. As shown in Fig. 33, the team constructed one circular and one square fuselage using the thin glue and another pair using the thick glue. The team preferred using the thick glue due to its quick drying time, hence the pieces are less likely to move out of place.

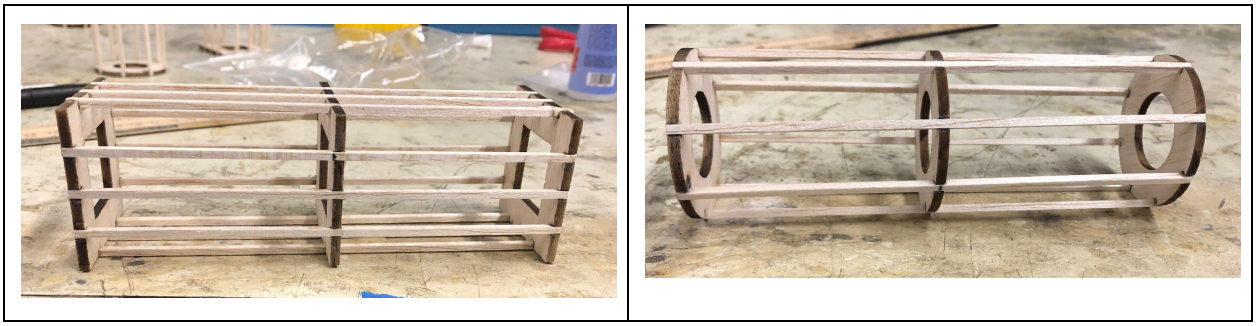

Figure 33: Finalized Models of Square and Circular Fuselages

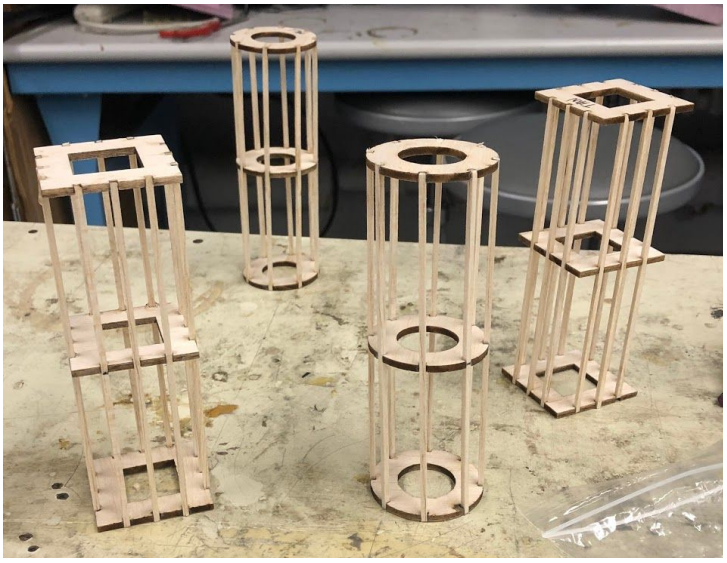

Figure 34: Four Finalized Models of Fuselages

As a result, the team was able to construct four fuselages out of balsa wood, two square and two circular. The construction process was relatively easy. The only issue was how the circular fuselage was in a slight torsion, to which the team could not come to a definite conclusion as to why this occurred. Our hypothesis is that each circular piece wasn't cut the same and as a result each circle wasn't perfectly aligned during construction, hence causing the torsion. The fuselages were later tested under loading and impact in order to decide what shape of the fuselage to go with. These tests and results are described in further detail in Section 5.2.

4.2.1 Material Property Calculations

The team did not know the material properties of the lab carbon fiber. The material properties of carbon fiber, such as density, can estimate a weight distribution. Accurate weight measurement is needed to calculate the center of mass.

The carbon fiber and foam are not available on SolidWorks or online. There are two unknowns: the wing carbon fiber density, and the wing foam mass. We did not consider any ingredients in the fabrication. We are only concerned in the final result. The team made functions in Python to find these values. See Appendix D for an example of the code.

The known values from SolidWorks include the carbon fiber and foam volume. The known values from the vendors include the foam density. From the finished wing, the team weighed the total mass of the carbon fiber and foam wing.

The mass of the foam was found with volume, and density of the foam. The density of the carbon fiber was found with the newfound foam mass, total mass, and carbon fiber volume as detailed in the following algorithm. With these values, the team found the density of the carbon fiber as 31.04 lbs/ft^3.

4.2.1.1 Material Property Algorithm

How to find an unknown density:

1. Create SolidWorks model
    a. Foam shape
    b. Carbon fiber shell
        i. Assume 1 mm thickness

2. Capture SolidWorks model volume
3. Create lab prototype
4. Capture prototype mass
5. Divide step 4 by step 2

4.2.2 Theoretical Calculations of Wing Load Distribution

This section provides a crude, back-of-the-envelope type of calculation to verify that the load applied to our wing as a result of a level turn will not cause structural issues for our wing. To simplify the analysis, several assumptions had to be made. The first assumption made was that the load on the wing would correspond to the load factor given in Section 4.1.7 for minimum turning radius, multiplied by a safety factor of 1.4, bringing the assumed load to 4.58 G's.

The model that we assumed for our calculations is the following:

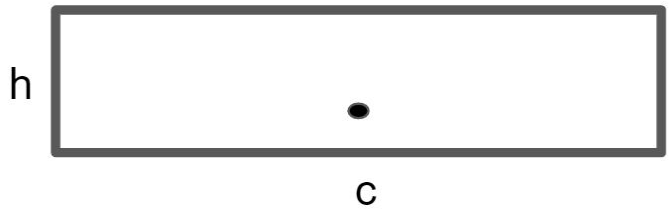

Figure 35: Simplified Wing Model

The length c corresponds to the chord length of the wing, which was allowed to vary with spanwise position based on the wing's taper. The height, h, was also allowed to vary linearly as a function of spanwise position. The centroid was placed asymmetrically as indicated on the diagram, roughly approximating the centroid of the actual airfoil shape, placing it at 40% the height h. These measurements also allowed us to create a moment of inertia about the centroid,

which was also allowed to vary with spanwise position.

The load on the wing was assumed to be an elliptical distribution. To calculate this, the aerodynamic load on the wing root, L'_0 must be calculated using the following equation (*see* Raymer, 2018).

$$L'_0 = \frac{nW}{2} \Big/ \int_0^{b/2} \sqrt{1 - \left(\frac{2z}{b}\right)^2}\, dz \tag{22}$$

In this equation, *z* indicates spanwise position. Matlab's symbolic toolbox was used to perform this integral. In our application, this value comes out to 6.4 lbf. From this load at the wing root, the lift distribution can be found as a function of spanwise position using the following equation (*see* Raymer, 2018).

$$L' = L'_0 \sqrt{\left(1 - \left(\frac{2z}{b}\right)^2\right)} \tag{23}$$

To find the shear force experienced at each spanwise position, the following equation was applied to find shear force in the wing.

$$V = \int_z^{b/2} \left(L'_0 \sqrt{1 - \left(\frac{2s}{b}\right)^2} \right) ds \tag{24}$$

In this equation, s is the spanwise position left outboard of the position being evaluated. Likewise, the moments can be calculated using the following equation (*see* Raymer, 2018).

$$M = \int_z^{b/2} \left((s - z) * L'_0 \sqrt{1 - \left(\frac{2s}{b}\right)^2} \right) ds \tag{25}$$

Normal and shear stress can also be calculated from these shear forces and moments

respectively. The equations for such calculations are as follows.

$$\tau = \frac{V(z)}{A} \qquad (26)$$

$$\sigma_{xx} = M(z)\,\frac{y_{max}}{Ixx} \qquad (27)$$

For this application, only the compressive stress was considered, as this stress will have a larger magnitude in our application, and it is the weaker direction in terms of carbon fiber's strength. The resulting plots of wing loading, shear force, moment, shear stress, and normal stress are presented below as Figs. 36 a-e.

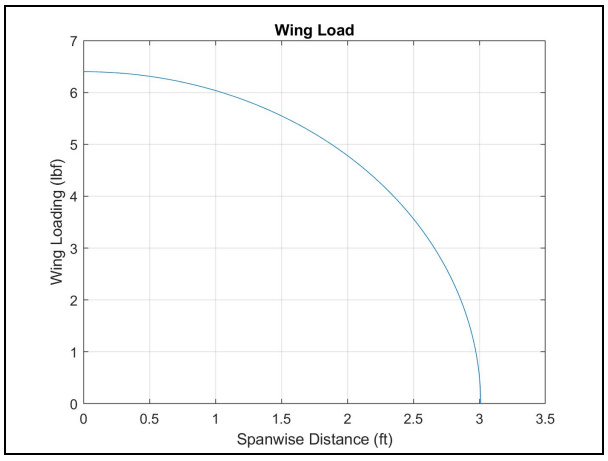

Figure 36a: Spanwise Wing Load Distribution

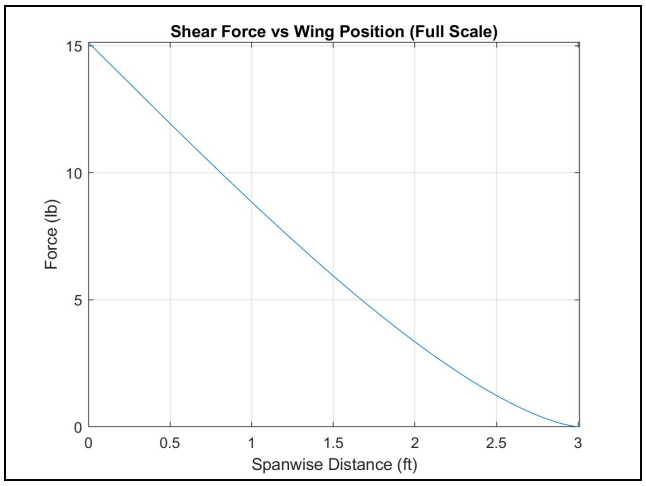

Figure 36b: Spanwise Shear Force Distribution

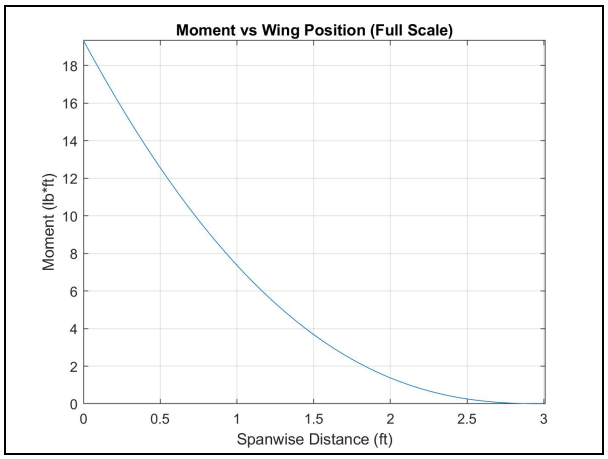

Figure 36c: Spanwise Moment Distribution

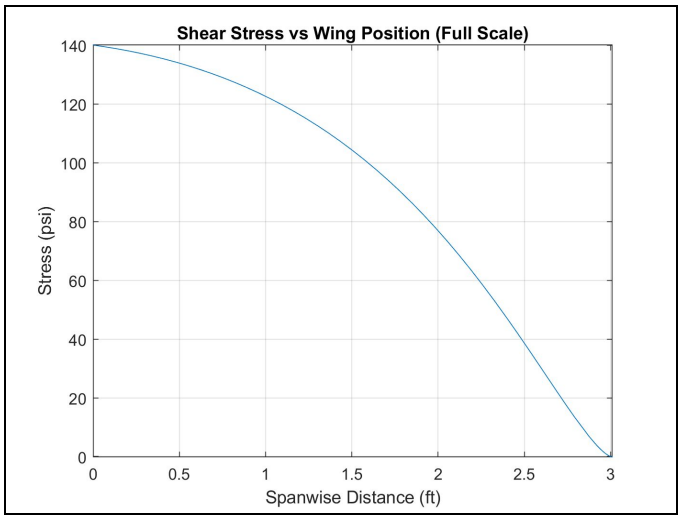

Figure 36d: Spanwise Shear Stress Distribution

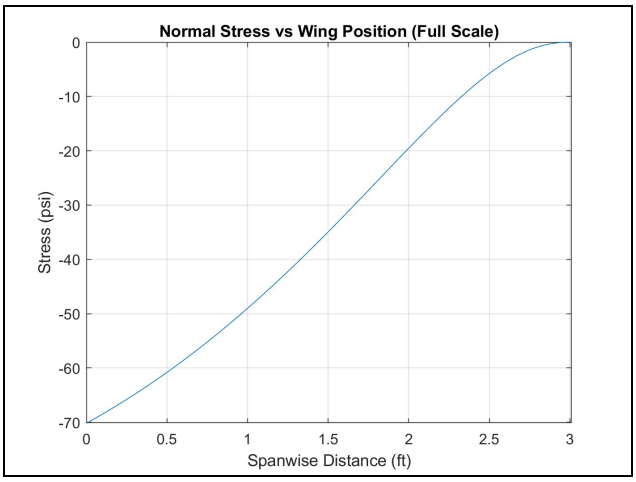

Figure 36e: Spanwise Normal Stress Distribution

These plots allow us to make several conclusions. First, based on the wing load distribution plot, we can verify that the mathematical model does produce an elliptical load distribution over the span. The plots for shear and moment are more interesting. Typically for a fixed cross-section beam, the shear force would decay linearly. In this model, it is slightly nonlinear, especially toward the tip due to the wing taper. The moment decays roughly as it would for a fixed cross-section. The shear stress, which for this application is an out of plane, or transverse shear, has a maximum at the wing root, with a value of 140 psi, and decays to 0 psi at the tip. For laminated composites, transverse shear is the weakest component of shear stress. Proper evaluation of transverse shear requires extensive testing, and is still an active area of research. This analysis was beyond the scope of the current project. The magnitude of stress is so small, however, that it was not believed to be a major concern. The normal stress, which is the compressive stress on the top surface of the wing, decays from 70 psi at the root, to 0 psi at the wing tip. Considering that carbon fiber laminated composites have a compressive strength on the order of 1,000-2,000 psi, the normal stress developed in the wing was also not a major concern. A wing loading test was performed as verification of this analysis. That test is described in Section 5.3.

4.2.3 Landing Ski

To protect the aircraft propeller upon landing, we designed a landing ski. Due to the 3 inch long fuselage bottom, we opted for one large ski opposed to two small skis. Two small skis seemed questionable because of how much contact area there will be for adhesion. Therefore,

one large ski allows for more contact area adhesion. The holes in the landing ski are to lighten the overall weight of the ski, as well as reduce the amount of drag it will experience. The landing ski was not implemented in the final design due to time constraints. An isometric view and drawing can be seen in Figs. 37 and 38.

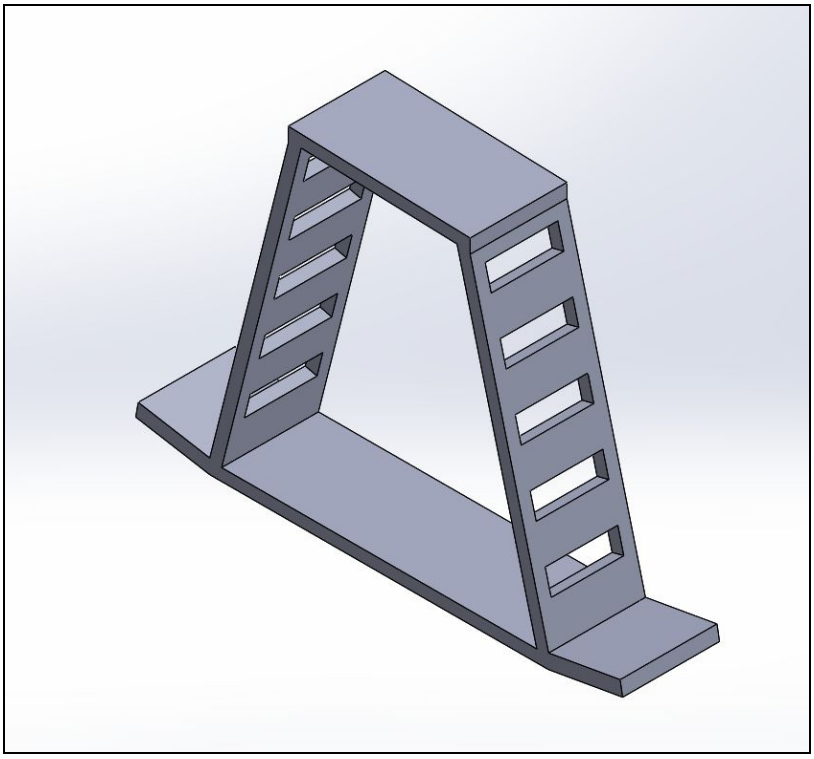

Figure 37: Landing Ski Isometric

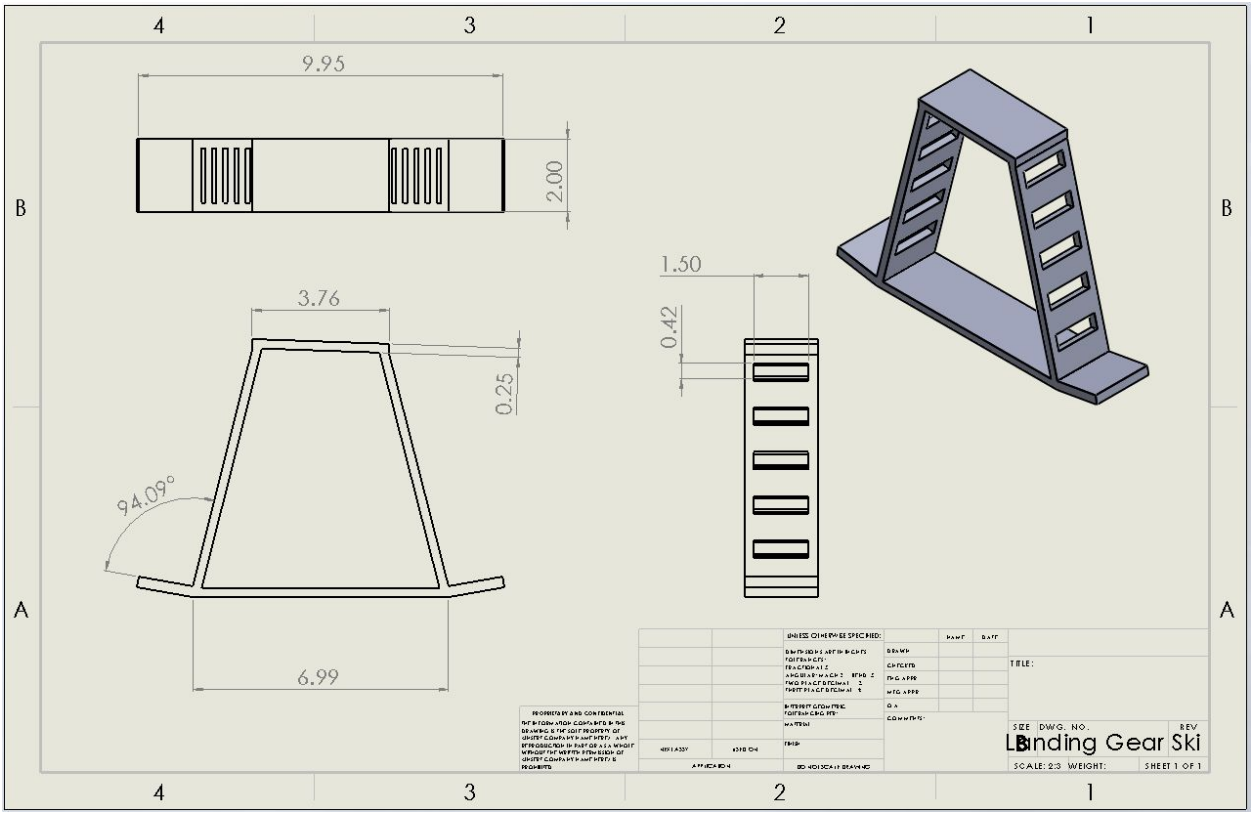

Figure 38: Landing Ski Drawing

4.2.4 Payload Carry and Release

For one of the missions, certain payloads have to be carried by the airplane . These payloads consist of bean bags that weigh approximately one pound each. Thus, a major point of analysis is to determine the optimum way to carry the payload in order to reduce drag of the plane. Also, to provide stability as well as sufficient clearance for safe hand launch. Principle design requirements were that the system had to be structurally robust, easily loaded, and secured from opening during flight. Our design of the payload mechanism can be seen in Fig. 39. We 3D printed the mechanism from polylactide (PLA), and a servo motor was used to control the payload system.

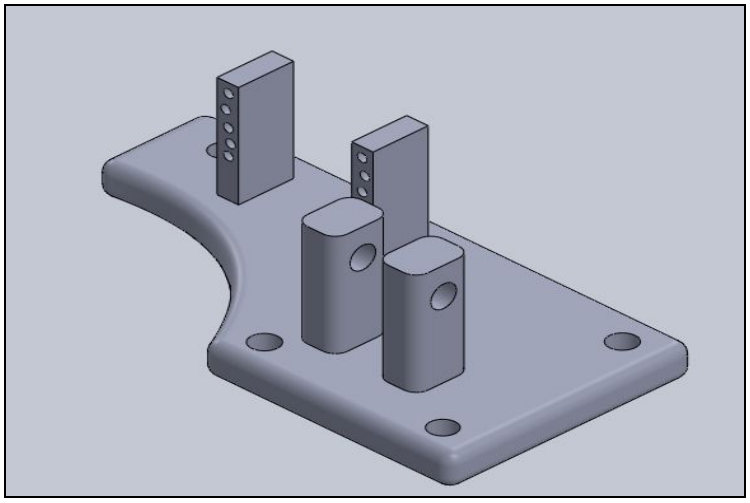

Figure 39: Payload mechanism design

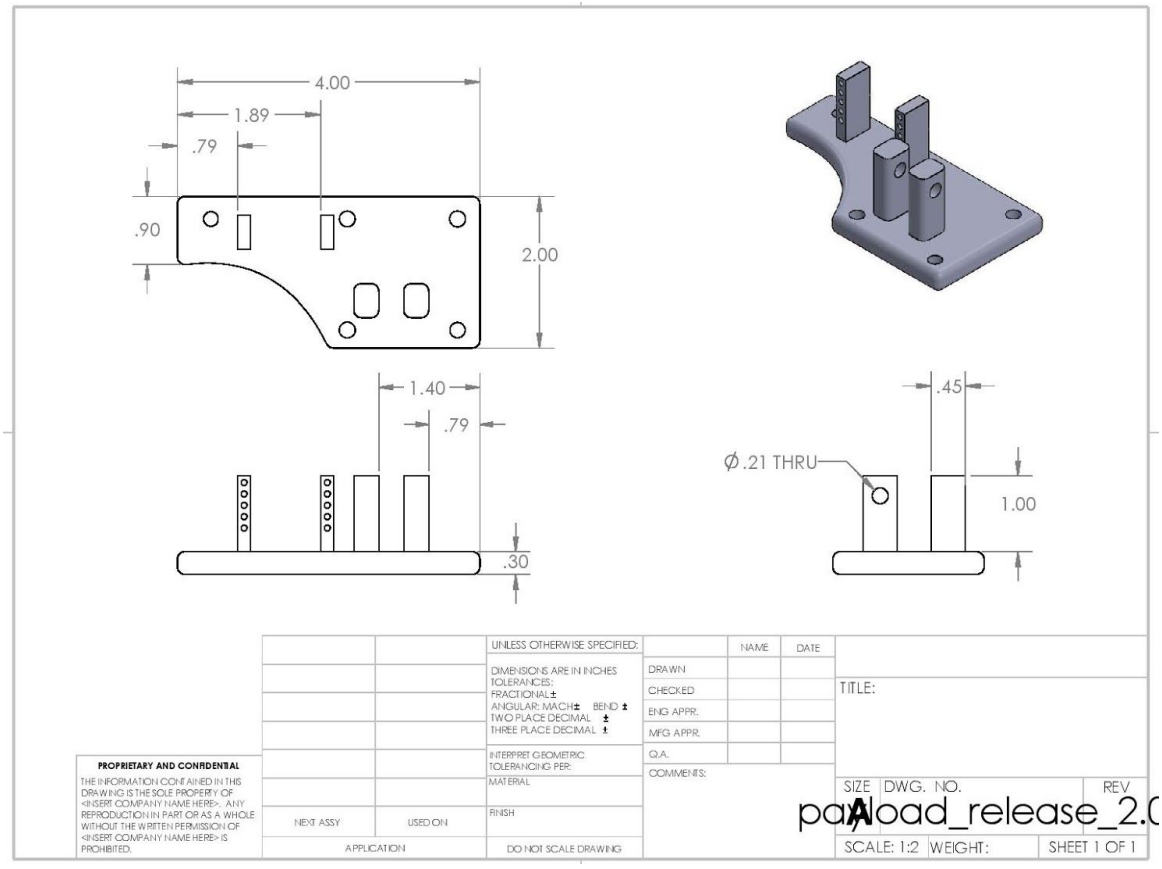

Figure 40: Payload Mechanism Drawing

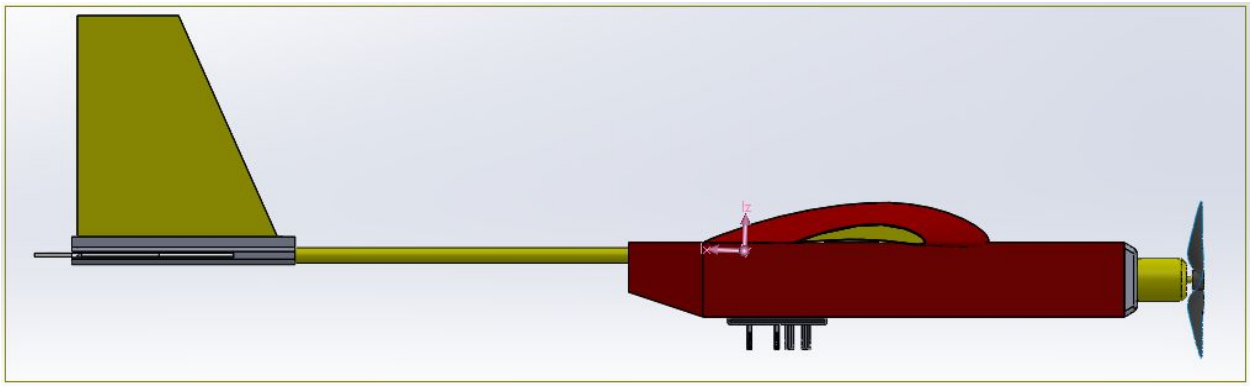

Figure 41:Location of the Payload Mechanism

4.3 Propulsion System Design

This section discusses the propulsion of the aircraft. The propulsion system includes the battery, electronic speed controller, motor, and propeller.

4.3.1 Battery

The team opted for the maximum battery size per the WPI Internal competition rules. A larger battery will hold a larger charge, which translates to a larger endurance. Therefore, the team chose the 11.1 volt 2200 mAh 3S battery.

4.3.2 Electronic Speed Controller (ESC)

The ESC selected by the team has a capacity of 60A. This is done to ensure sufficient safety for amperage draw between the motor and the battery. Given the motor has a draw of 42A, then a 30% safety factor rounds to a 60A ESC. The selected ESC includes a battery eliminator circuit (BEC). This reduces the need for a separate battery to control the ESC.

4.3.3 Motor

The team selected a 650 Watt 1200 Kv brushless outrunner motor. This motor was selected with the support of *Hog Heaven* associates. The associate reviewed the aircraft specifications and suggested this motor. There was no thrust stand present, so the team could not test various motors. Since we could not test different motors, we listened to the advice of the sales associates.

Thrust to weight was analyzed for three conditions: cruise, loiter, and take-off. For cruise loiter, and stall, the equation for thrust to weight is exactly the same:

$$\frac{T}{W} = \left(\frac{\frac{1}{2}\rho V^2 C_{D0}}{(W/S)}\right) + \left(\frac{(W/S)}{\pi A R e_0 \left(\frac{1}{2}\rho V^2\right)}\right) \qquad (28)$$

For each condition, all that changes are the wing loading values input into the equation. These values can be found for each condition in Section 4.1.4. A value for a historical norm was also found out of a horsepower to thrust conversion (*see* Raymer, 2018). Though this historical value is taken from analysis of full-scale aircraft, it remains consistent with typical values calculated by other resources (*see* Mueller, 2019) . Values for thrust-to-weight are tabulated below.

Condition	**Thrust/Weight**	**Thrust Required**
Cruise	0.0525	0.3468 lbf
Loiter	0.0607	0.4005 lbf
Stall	0.0912	0.6017 lbf

Historical Norm	0.5238	3.457 lbf

Table 14: Thrust Parameters by Flight Condition

It becomes obvious that the thrust required to maintain flight at each trim condition is significantly lower than the historical norm. This is a result of the values for thrust to weight being the value required to simply overcome drag at each condition. The historical norm value is related to the maximum thrust available to the vehicle. This additional thrust can be used during maneuvers, such as the turn analysed in Sec. 4.1.7, or to accelerate from one trim state to another.

The thrust of the motor selected for our application was plotted against the drag found in Section 4.1.6 to give the plot in Fig. 42. This plot displays that at the cruise condition, we have 3.1 pounds of thrust available to us, while only requiring 0.6 pounds to maintain level flight. This lends confidence that our motor selection will be more than sufficient to power our aircraft for all of its needs.

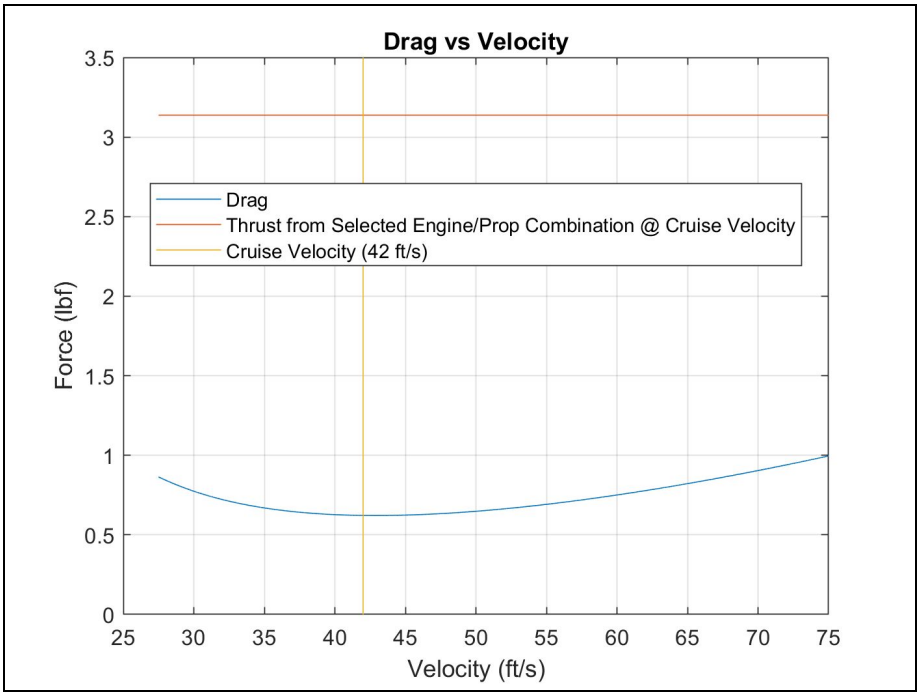

Figure 42: Drag vs Velocity Compared to Selected Motor

4.3.4 Propeller

The team selected a 14” x 8” single blade Advanced Precision Composites propeller. This propeller was selected because it is recommended by the motor manufacturer.

4.4 Control System Design

The stability and controls group worked on designing an aircraft that is statically and dynamically stable. The following sections will explain the various steps we conducted to achieve a statically and dynamically stable aircraft.

4.4.1 Static Stability

To determine whether or not the aircraft is statically stable as designed, two parameters need to be evaluated. These parameters are the neutral point and the most-forward point. In order

to be considered statically stable, the center of gravity (CG) must be located between these two points. To find the neutral point of the aircraft, we used the following equation out of the AE 4723 Aircraft Dynamics and Control class taught by Professor Cowlagi at WPI (*see* Cowalgi, 2019):

$$h_{np} = h_{ac} + \frac{a_t}{\bar{a}}(1 - \frac{d\varepsilon}{d\alpha})V_h \qquad (29)$$

Where h_{ac} is the aerodynamic center of the wing as a percentage of mean aerodynamic chord, definitionally 0.25. a_t is the tail lift curve slope of the tail, found in Section 4.1.1. $\bar{a}$ is a quantity given by the following equation:

$$\bar{a} = a + a_t \frac{S_{HT}}{S}(1 - \frac{d\varepsilon}{d\alpha}) \qquad (30)$$

Where a is the lift curve slope of the main wing, found to be 5.209 rad^{-1} from the plots in Section 4.1.1. $\frac{d\varepsilon}{d\alpha}$ is the downwash derivative, given by the following equation:

$$\frac{d\varepsilon}{d\alpha} = \frac{2a}{\pi AR} \qquad (31)$$

V_h is also a quantity, which is given by the following equation:

$$V_h = \frac{S_{HT}}{S} \frac{\overline{L_t}}{\bar{c}} \qquad (32)$$

Here, $\overline{L_t}$ is the distance between the wing and tail aerodynamic chord, and $\bar{c}$ is the mean aerodynamic chord. Evaluating all of these quantities together yields a value of neutral point of 65.55% mean aerodynamic chord, which when dimensionalized, comes out to 0.4725 ft behind the leading edge of the wing.

The other parameter to evaluate is the most forward point, given from the AE 4770 class in the form of the following Eqn. 33 (*see* Olinger, 2019):

$$h_{mf} = \frac{-0.15 + h_{ac} + A * h_{act}}{A + 1} \qquad (33)$$

Where A is a quantity given by the following equation:

$$A = \eta \frac{S_t}{S} \frac{a_t}{\bar{a}} \left(1 - \frac{d\varepsilon}{d\alpha}\right) \qquad (34)$$

Where η is a constant, given by 0.9. h_{act} is the moment arm between the aerodynamic centers of the wing and tail normalized by dividing by the mean aerodynamic chord. Applying Eqn. 33, we found that our most-forward point was 35.85% of mean aerodynamic chord. When dimensionalized, the most-forward point is located 0.2584 ft behind the leading edge of the wing.

In order to remain stable, the center of gravity must be located within this envelope. The center of gravity of an RC aircraft can be greatly influenced by the location of electronic components within the fuselage. With this in mind, we will place our electronics accordingly once all of the electronics for the aircraft have been selected.

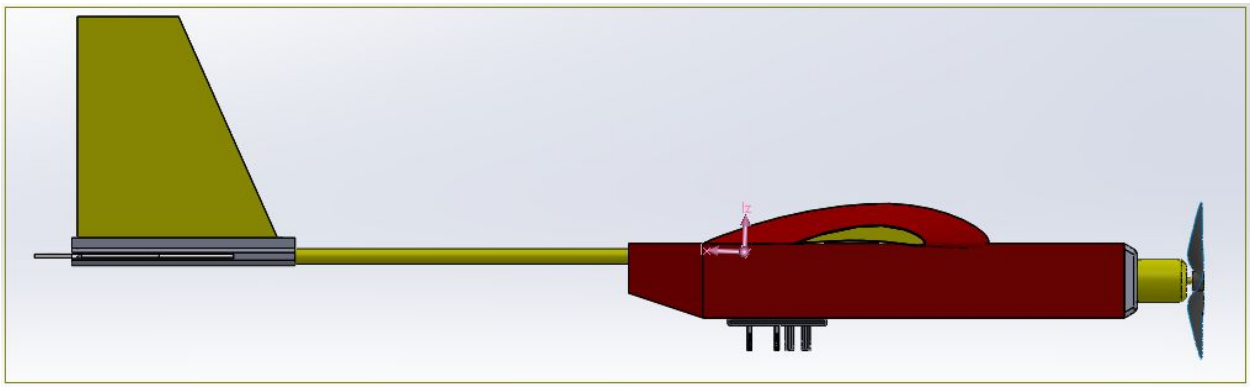

Figure 43: Drawing of Aircraft on SolidWorks.

In the final design, the center of gravity was placed at about 55% of the mean aerodynamic chord. This placement, based on available calculations, should result in static stability for the aircraft.

4.4.2 Control Surface Sizing

In addition to determining the static stability of the aircraft, we also designed the control surfaces needed for the aircraft. The control surfaces the team decided to use are ailerons, flaps, an elevator, and the rudder. This section will be addressing how we designed each control surface and why we decided on specific parameters when designing the control surfaces.

Using various publications and Raymer's (2018) book, which is used for the Aircraft Design course at WPI, we designed the control surfaces using the historical data for area percentage shown in Table 15. The area percentage are approximations that allowed our team to calculate how much of the tail and wing area had to be dedicated to the control surface.

Control Surface	Area Percentage	Resulting Area
Ailerons	10%	0.414 ft^2
Flaps	35%	0.343 ft^2
Elevator	40%	0.121 ft^2
Rudder	35%	0.174 ft^2

Table 15: Area percentage and resulting area of control surfaces.

Once the team decided on an area percentage and calculated an initial area, we then proceeded to design the specific sizing of each control surface. Using Raymer (2018), Sadraey (2012), and the calculations done by the Aerodynamics group, we calculated the following dimensions, shown in Table 16 using a combination of percentage estimates for each control surface.

We obtained the chord length from the area by using simple algebra. For our elevator and rudder, the span of the control surface was the length of the horizontal tail and vertical tail respectively. Then, we divided the resulting area as shown in Table 15 (span * chord) by the length of the tails to obtain the chord. We used a similar approach to determine the chords for our flaps and ailerons. The only difference is we left an inch of buffer space in between each control surface and the tip of the wing (4 inches total). We also had to take into account the width of the fuselage. As a result, we subtracted the width of the fuselage and four inch buffer space from the wing span before calculating the chords for the aileron and flaps.

Control Surface	Resulting Area	Chord	Span
Ailerons	0.414 ft^2	0.75 ft	0.19 ft
Flaps	0.343 ft^2	1.81 ft	0.19 ft
Elevator	0.121 ft^2	0.775 ft	0.16 ft
Rudder	0.174 ft^2	0.226 ft	0.77 ft

Table 16: Calculated dimensions for control surfaces.

Once we determined the dimensions of each control surface, we were able to begin determining the necessary sizes for the servos needed for our aircraft.

4.4.3 Servo Sizing

Servo motors are used to control the various control surfaces. For our aircraft we are using six servos: One for each aileron and flap, the rudder, and elevator. In order to select the appropriate servo for each control surface the team calculated the torque output required from each servo in order to adequately maneuver the control surfaces. We used Eqn. 35 to calculate

the torque required. This equation was taken from Chuck Gadd's (*see* Servo Torque Calculations, n.d) discussion on servo torque calculations.

$$T = \rho * C_{cs} * V^2 * L * \frac{sin(\Theta_{cs})}{tan(\Theta_s)} \qquad (35)$$

Where C_{cs} is the chord length of control surface, L is the length of control surface , Θ_{cs} is the maximum control surface deflection relative to the wing, and Θ_s is the maximum servo deflection. We selected the maximum deflection angles for the control surfaces and servos based on historical data found in Raymer's Aircraft Design textbook. The different torque values we got can be seen in Table 17.

Control Surface	C_{cs} (m)	V (mph)	L (m)	Θ_{cs} (degrees)	Θ_s (degrees)	Torque (oz-in)
Aileron	0.0579	28.64	0.228	30	35	9.22
Flaps	0.0579	28.64	0.55	30	35	22.24
Rudder	0.07	28.64	0.235	35	50	13.89
Elevator	0.0475	28.64	0.235	25	35	6.39

Table 17: Torque needed for every control surface.

After determining the torque output needed for the servo, the team was able to determine what servos to use for the different control surfaces. Our servo selection can be seen in Table 18

Servos	**HS-40**	**HS-53**	**HS-40**	**HS-45HB**
Use	Ailerons	Flaps	Elevator	Rudder
Voltage (V)	4.8-6.0	4.8-6.0	4.8-6.0	4.8-6.0
Torque (oz-in)	8.4-10.5	20.9-26.5	8.4-10.5	13.0-17.0

Weight (oz)	0.17	0.25	0.17	0.28
Dimensions (in.)	0.79 x 0.34 x 0.67	1.12 x 0.46 x 0.95	0.79 x 0.34 x 0.67	0.92 x 0.38 x 0.88

Table 18: Servos selected with their respective specifications.

4.4.4 Servo Placement

In order to have adequate control over the aircraft, it is the convention that all control surfaces have a maximum deflection angle of 20 ° (*see* FAA, 2009). To achieve this we placed the servos, so that the servo arm makes a ninety-degree angle with the control horn. Usually, a small hole is cut on the wing, and the servos are placed in the opening so as to protect them from falling off and not disrupt the flow of air around the wing. However, because our plane is made entirely of carbon fiber it wasn't feasible to cut an opening for the servo on our wing. In addition, we originally decided to have landing gear on our plane in order to reduce our empty weight. All these reasons factored into why we decided to place the servos on top of the wing using super glue. By placing the servos on the wing we were able to avoid destroying the servos in case of a crash.

4.4.5 Linkage System

In order to move the control surfaces, we created a linkage system for all our control surfaces. Our control system consisted of a push rod, control horns, and servos. We decided to use a push-pull system for all our control surfaces because it would only need one servo instead of two if we had used a pull-pull system. We made the control system by glueing the control horn to the edge of the control surface using super glue. Then, we used pliers to bend the ends of

the pushrod into a zigzag pattern in order to prevent the rods from slipping out of the control horn and servo arm. We found a 6 inch push rod gave us the most amount of deflection in our control surfaces. Therefore, after experimenting with pushrods of other lengths, we made the decision of using the 6 inch pushrods. Finally, we connected the other end of the push rod to the servo arm. This set-up created the push-pull system we used for all our control surfaces. Figures 44a, 44.b, and 45 demonstrate the materials we used for our linkage system and our final result.

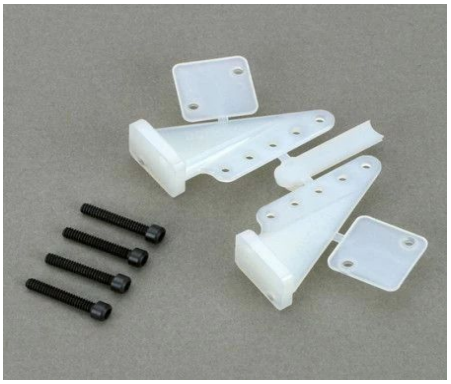

Figure 44a: Control Horn

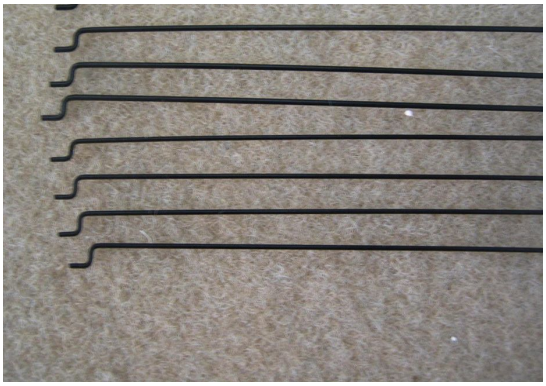

Figure 44b: Push Rods

Figure 45: Push-Pull Linkage System

4.4.6 Dynamic Stability

To assure that small disturbances during flight settle to zero after some period of time, we had to analyse the characteristics of the aircraft's dynamic stability. To accomplish this, we looked at both the longitudinal and lateral modes. These were evaluated using a combination of hand calculations and XFLR5 simulations.

From the SolidWorks Model, we obtained the following moments of inertia:

Component	Value (lb ft^2)
I_{xx}	503.98
I_{yy}	406.19
I_{zz}	885.85
I_{xz}	13.49

Table 18: Moments of Inertia

From these values, as well as the procedures outlined by Napolitano (2013), we were able to construct both the longitudinal and lateral state matrices.

```
A_long =

   -0.1565    0.4372         0  -32.2000
   -3.4334   -5.9909   26.8521         0
    0.0815   -3.9191  -10.7718         0
         0         0    1.0000         0
```

Figure 46: Longitudinal State Matrix
The longitudinal state matrix is formed in imperial units for simplicity

```
A_lat =

   -0.3450    0.0257  -12.9777    9.8100
    0.4046  -18.2200    6.7369         0
    3.5015   -2.7517   -2.8748         0
         0    1.0000         0         0
```

Figure 47: Lateral State Matrix
The lateral state matrix is formed in metric units due to issues with unit conversions

To determine if the aircraft is stable, the eigenvalues of both matrices must have negative real components. Each eigenvalue describes the behavior of a specific mode of aircraft stability. These modes are given in Figs. 48 and 49 for the longitudinal and lateral modes, respectively.

```
-8.4595 + 9.9852i
-8.4595 - 9.9852i
-0.0001 + 1.6191i
-0.0001 - 1.6191i
```

Figure 48: Eigenvalues of the Longitudinal Modes

```
-17.1095 + 0.0000i
 -2.3047 + 6.7462i
 -2.3047 - 6.7462i
  0.2792 + 0.0000i
```

Figure 49: Eigenvalues of the Lateral Modes

From these eigenvalues, it can be determined that the aircraft does have longitudinal stability, though it is marginal. The short period mode settles very quickly, in less than one second, but the phugoid mode settles much more slowly, over the course of several minutes. The short period mode is almost an unnoticeable disturbance and settles out before it causes any significant change in any of the aircraft state variables. The changes to the state variables imparted by the short period mode is negligible compared to the phugoid mode. The phugoid

mode will cause oscillations that persist unless addressed, hindering the performance of the aircraft and its ability to complete its mission. This result enforces the need for a pitch control system to mitigate disturbances. As for the lateral modes, the roll convergence mode is not oscillatory and settles in less than one second. The dutch roll mode is oscillatory and settles in less than two seconds. The mode that causes most concern is the spiral mode, which is unstable. This unstable mode is, however, stabilizable, through control. This will be demonstrated later in this section.

Matlab and XFLR5 were used to simulate the uncontrolled response to disturbances and illustrate the stability characteristics mentioned above. The plots are included with commentary Fig 50.

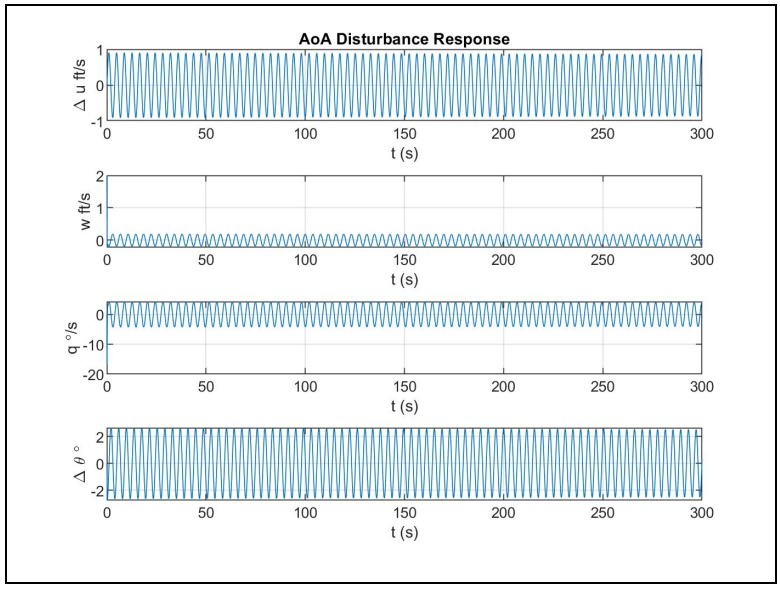

Figure 50: Longitudinal Angle of Attack Disturbance Response

In this plot, Δu is the change in velocity x component, w is the vertical velocity component, q is the pitch rate, and $\Delta\theta$ is the change in pitch angle. The disturbance response to several other disturbances follows a similar pattern to the response pictured in Fig 50. This

shows an unacceptable settling time which must be compensated with a control algorithm to prevent the aircraft from having unacceptable oscillations in pitch.

The response to a disturbance in the lateral modes is displayed in Fig 51, which was produced in XFLR5, due to difficulties calculating the corresponding stability derivatives. The response here increases exponentially with time, which if left uncontrolled, would lead to failure. As such, we will need a control algorithm to mitigate this response. In these plots, the top left represents the lateral, or slip velocity in ft/s, *v*, the to right plot represents roll rate in degrees/s, *p*, the bottom left plot represents yaw rate in degrees/s, *r*, and the bottom right plot represents roll angle in degrees, **ϕ**.

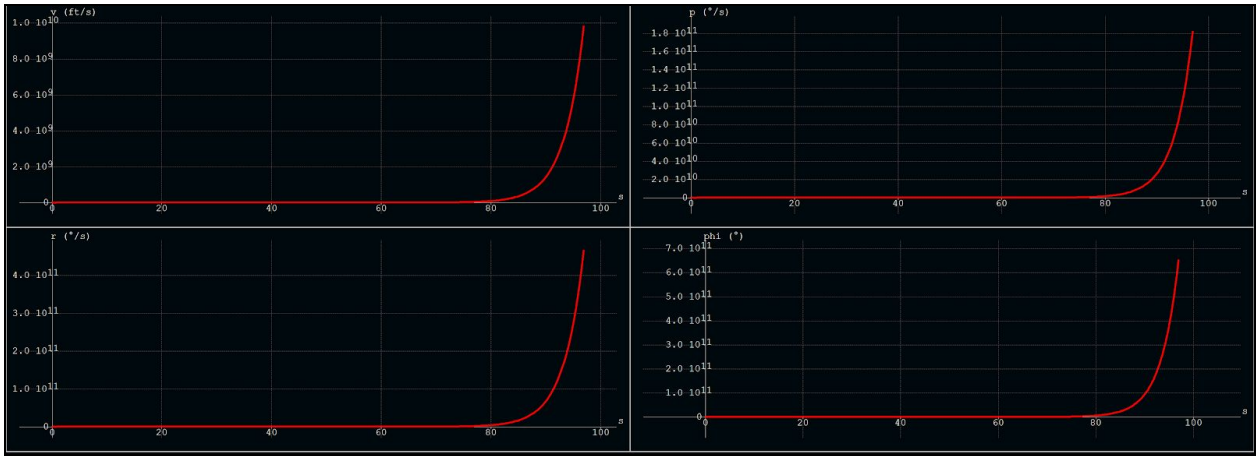

Figure 51: Lateral Disturbance Response

For longitudinal controls, the Aircraft Dynamics: From Modeling to Simulation (*see* Napolitano, 2013) book was used to determine stability derivatives based on the control surface sizing found in Section 4.4.2. The control gains were determined using pole placement techniques in Matlab. For longitudinal control, the control gains are as follows in Fig. 52:

```
K_long =

    0.0003   -0.0115   -0.0361   -0.0862
         0         0         0         0
```

Figure 52: Longitudinal Control Gains

These gains were simulated in Matlab, with the results displayed as Fig. 53.

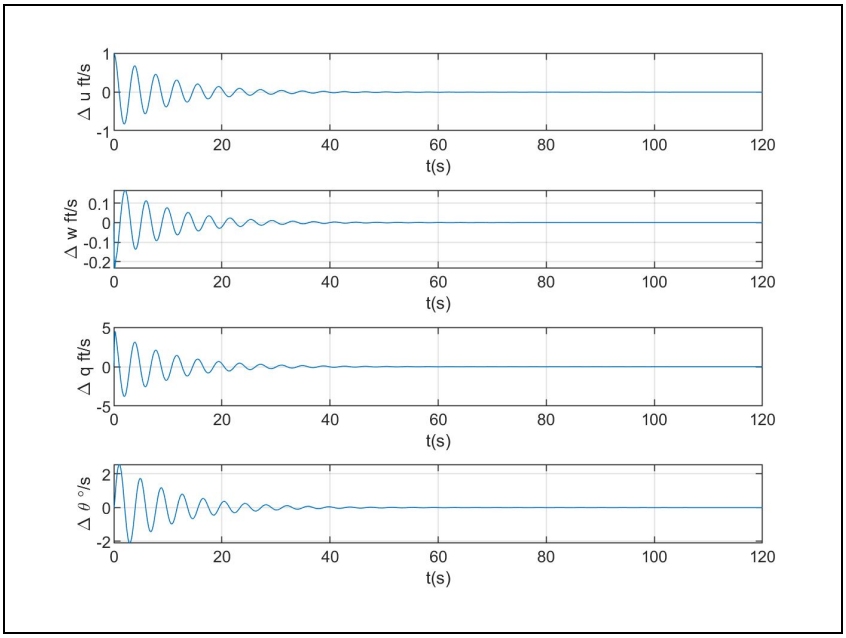

Figure 53: Longitudinal Controlled Response

This response is significantly more stable, and has a phugoid mode that settles in 40 seconds, rather than the several minutes seen in the uncontrolled case.

A similar approach was employed for the lateral controls as was employed in the longitudinal controls. The control gains were determined in Matlab using a linear quadratic regulator to find the optimal control gains. The control gains were found as follows in Fig. 54:

```
Klat =

    0.0085    0.0168   -0.0040    0.2827
    0.0042    0.0042   -0.0058    0.0663
```

Figure 54: Lateral Control Gains

The simulated response based on these control gains is as follows:

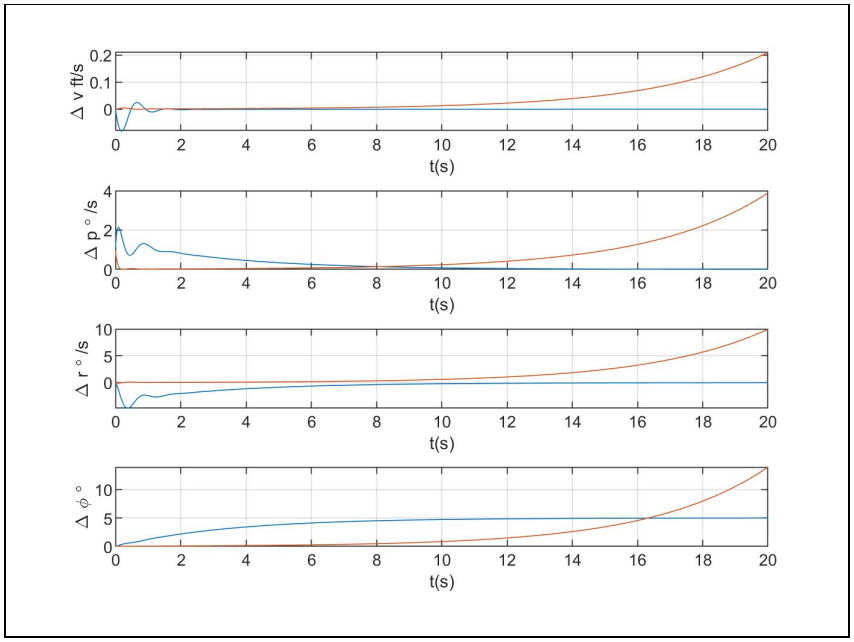

Figure 55 Lateral Controlled Response
Red is the uncontrolled response, the blue line is the the controlled response

Figure 55 displays that the control gains specified above are able to control the previously unstable spiral mode, and lead to convergence. Δv is the change in velocity y component, p is the rate, r is the yaw rate, and $\Delta\Phi$ is the change in roll angle.

4.4.6 Autonomy

A way to obtain extra points during the competition was to make our aircraft autonomous. The aircraft was to perform waypoint navigation, automatic payload drop, and stay within a restricted boundary. Unfortunately, due to time constraints and unforeseen circumstances, we were not able to fully complete this portion of our project. However, we were able to plan a complete way point navigation mission using Mission Planner and upload the mission to the Pixhawk. We also connected our receivers and servos to the Mission Planner application. The final step for us to complete autonomy was to arm our aircraft's motor via our radio controller with the Mission Planner application. From the instructions given, to arm our

vehicle we were to hold the throttle down and to the left. However this step did not work for us. We attempted to contact Holybro, the manufacturer of the Pixhawk for assistance but we did not get a response back. Due to the lack of time and resources sadly we were not able to arm our vehicle and complete our last step in the autonomy portion.

5.0 Aircraft Fabrication

In this section, we will discuss the manufacturing of the different aircraft components including the wing, tail, fuselage, control surfaces, additive manufacturing, and carbon fiber hand lay up.

5.1 Additive Manufacturing

Additive manufacturing was used to build components of the aircraft. The components that used additive manufacturing include the motor mount, tail connector, landing ski and horizontal control surface.

There are steps to creating these components. The first step is to model the part in SolidWorks. Note that the desired bottom of the component should be placed on the *Front Plane*. This is because the *3DPrinterOS* service will convert the perpendicular direction into the y-axis.

The next step is to save the SolidWorks part from a *.SLDPRT* file, into a *.STL* file. This is the file type supported by *3DPrinterOS.* The *.STL* file is then uploaded to the *3DPrinterOS* cloud services for slicing.

The final step is to orient the part on the printing bed, and determine the fill. The fill influences the speed of printing, strength of component, and weight of the component. These

three factors are important if there are constraints that need to be met. Note, a print time longer than 16 hours should be revised. This time limit is if the printer is shared with other people.

5.2 Carbon Fiber Hand Lay-up

All structural components of the aircraft were manufactured out of a carbon fiber composite. To manufacture this material, we used a twill-weave carbon fiber fabric from ACP composites that was salvaged from past MQPs, and West Systems two part epoxy that was purchased new. Later sections of carbon fiber composite were made using Aeropoxy two part epoxy, which was salvaged from past MQPs as well, but was less viscous and more challenging to work with.

The general process for manufacturing a carbon fiber composite involves a hand lay-up process. This process differs only slightly between laying up a wing, and creating carbon fiber plates. The process for laying up a wing section is detailed in this section, with differences noted for manufacturing plates.

The first step in constructing a laminate composite is to create the mold. In the case of a wing section, this constituted cutting a foam model of the wing section from insulating foam. In our case, this foam was Owens Corning Foamular 250 foam. If you were to make a plate, a flat metal sheet would do as a mold. To cut a wing out of foam, splines of the airfoil shape were cut from balsa wood and were nailed to both ends of the foam. A hot wire cutter was then used to trace the splines and cut the foam to the desired shape. A photo of the foam cutting process is included as Fig 56.

Figure 56: Application of Splines for Foam Cutting

After cutting the foam model, the carbon fiber sheet must be cut to size in order to cover the entire model. In addition to the carbon fiber sheet, a sheet of peel-ply must be cut. This sheet is made of a silky material, intended to cover the outer surface of the laminate to help separate excess epoxy from the surface, giving a better surface finish. This material is shown being cut in Fig 57.

Figure 57: Cutting Peel-Ply

In addition to the peel-ply, a sheet each of breather and wadding must be cut. The breather is a perforated plastic sheet designed to let excess epoxy soak through into the wadding, which is a synthetic cotton sheet. These layers are displayed in Fig 58 below.

Figure 58: Cutting Breather and Wadding

Additionally, plastic sheeting must be cut to create a vacuum bag. This vacuum bag will be explained in more detail later.

After all materials are cut, the epoxy must be mixed to the manufacturer's specification. This epoxy should be spread over the carbon fiber sheet, completely wetting out to fabric. Dry spots in the fabric could result in delaminations and weak spots in the final part. After the sheet is wetted, the sheet must be laid over the foam model. In the case of a plate, the metal sheet must be prepared by covering the contact area with a mold release wax, and then outlining the contact area with putty tape. After this, the carbon fiber sheet can be placed directly on to the plate, making sure that the sheet does not come into contact with the tape.

Once the carbon fiber has been laid onto the model, the peel-ply, then the breather, then the wadding must be placed over the exposed surface. Once all layers have been applied, they may be covered in the sheet prepared to be the vacuum bag. Before closing this bag, ensure that a slot has been cut for the vacuum fitting, and that the coupling has been placed inside. It may be beneficial to put an additional layer of wadding under the coupling in order to prevent the vacuum from clogging.

To close the bag, a strip of putty tape should be placed along the edges of the bag, doubling up where necessary, especially around creases and pleats. If necessary, use camps to achieve an adequate seal. Once the bag is done, the vacuum hose should be connected and the bag can be placed in an oven set to 125 degrees Fahrenheit to accelerate the curing process. Be sure to ensure that no leaks are present in the bag before leaving it to cure. An image of a completed vacuum bag in the oven is given as Fig 59.

Figure 59: Vacuum Bag in Oven

The vacuum bag should be left to cure for 17-24 hours, depending on the epoxy. At this point, the part can be removed from the oven and vacuum bag. Some post processing, including cutting and sanding of edges may be required to get the part into a condition acceptable for use.

5.3 Wing Manufacturing

The wing was constructed in 3 pieces, each manufactured in the manner described in Section 5.2. These three sections, displayed in Fig 60, were cut and sanded to be flat on adjacent surfaces so that they could be connected together.

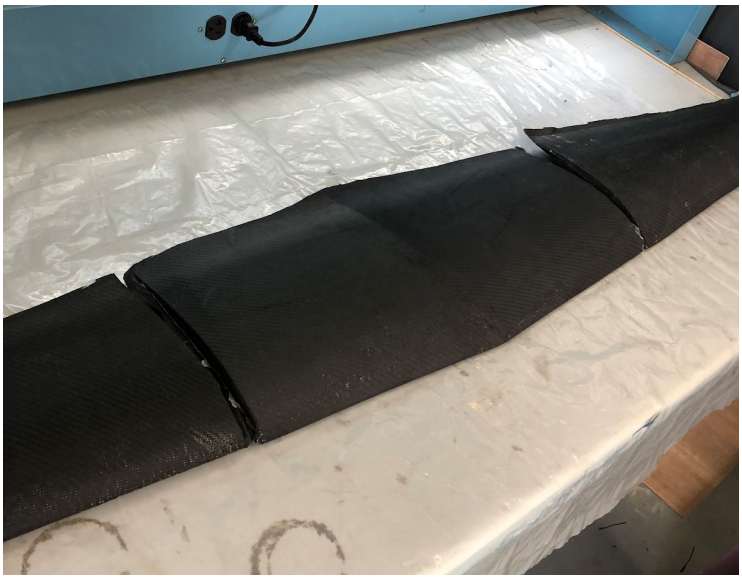

Figure 60: Wing in Three Sections

After the wing pieces were processed, they were laid-up together to create one solid wing assembly. This process differs from the vacuum bagging process only in that the lamina is allowed to cure in open air rather than under vacuum compression. This process is depicted in Fig 61.

Figure 61: Wing Assembly Lay-up

All together, the process of constructing the wing took six days to complete. This time requirement may seem like a long process for one component of the aircraft, but unlike prior MQP's, the premise behind a carbon fiber wing was to prevent damage and eliminate rework. Only one full wing was produced throughout the course of the project.

5.4 Tail Manufacturing

Tail sections were manufactured out of carbon fiber plates with a layer of polystyrene foam sandwiched between two layers of carbon fiber. These plates were used in both the tail and fuselage assemblies.

All three tail sections were cut from one carbon fiber plate. This plate, with outlines drawn for each tail section, is displayed as Fig 62.

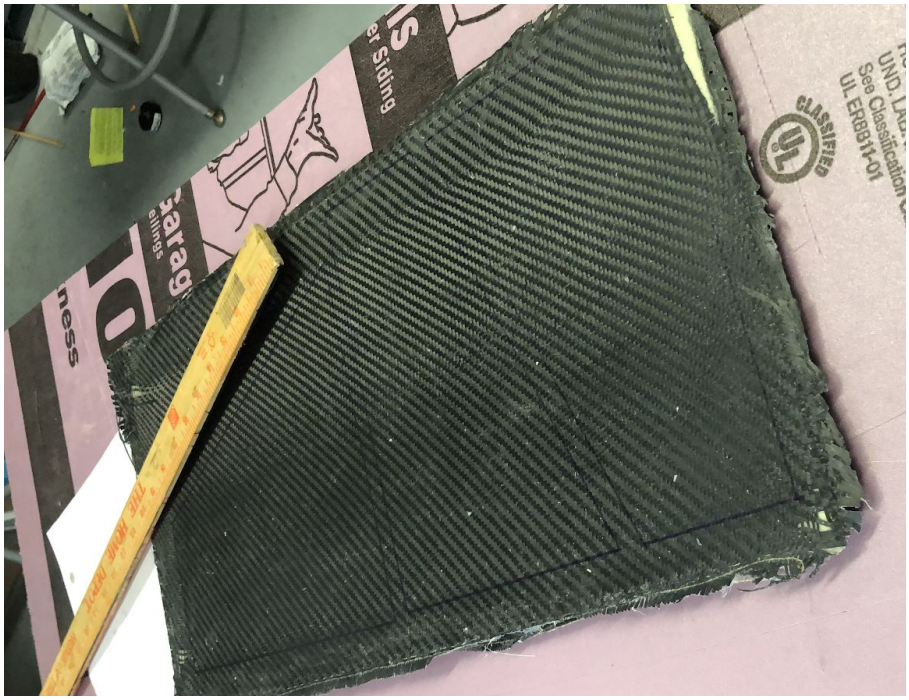

Figure 62: Plate for Tail Sections

5.5 Control Surfaces Manufacturing

After calculating the sizes of the control surfaces, we began to mark these measurements onto our wing and tail with a permanent marker. In order to cut through the carbon fiber wing, we used a Dremel to cut the different control surfaces. While cutting the control surfaces on the wing, we encountered difficulties over the flaps. This was due to the flaps having several layers of carbon fiber that were used to join three different parts of our wing together into one piece. In order to attach the tail to the fuselage, we 3D printed a connector that had slots to attach our vertical and horizontal tails. Due to our horizontal tails being uneven, the only control surface we were able to cut on the tail was the rudder. Therefore, we decided to 3D print our elevator control surface and attach it to our tail with hinges. Figures 63, 64 and 65 demonstrate the final design of our control surfaces.

Figure 63: Ailerons and flaps control surfaces

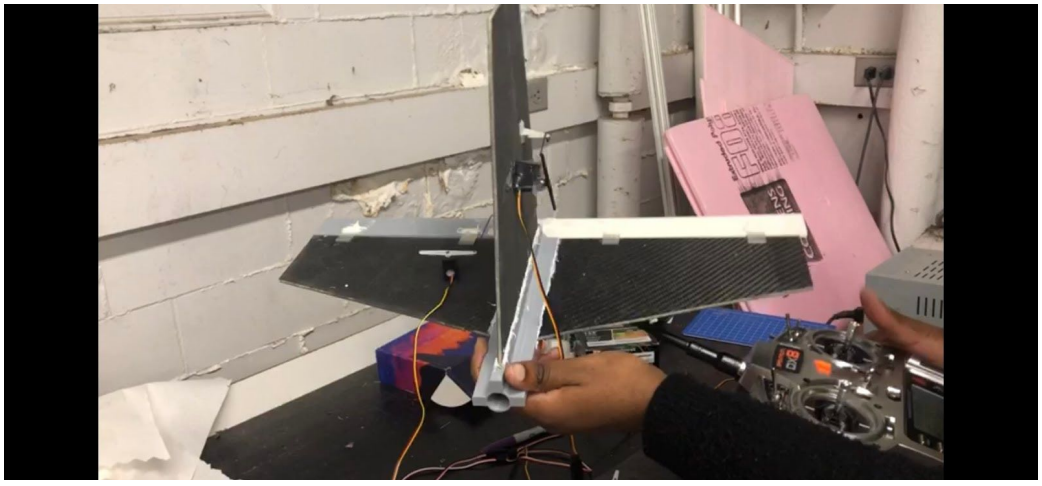

Figure 64: 3D printed tail connector in grey

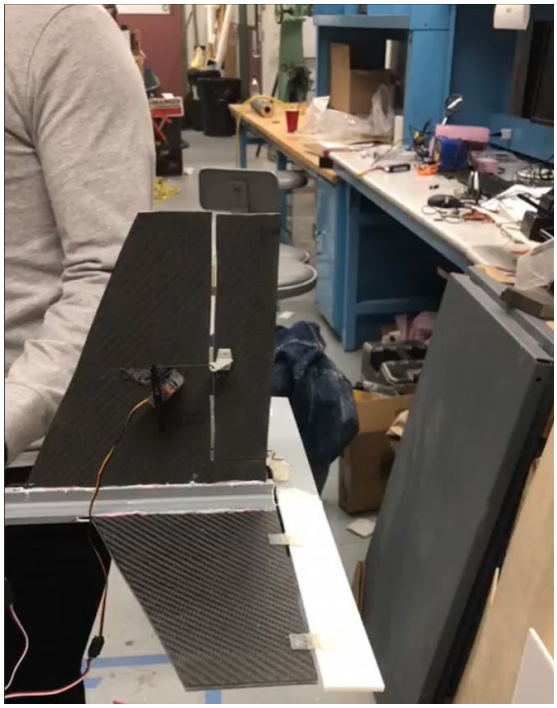

Figure 65: Rudder and 3D printed elevator control surfaces

As a team, we decided to use plastic hinges to attach our control surfaces onto the wing due to their low density and their easy access to repair. In order to attach the hinges to the wing, we cut slots on the control surfaces for every hinge to go into and then glued them to the wing. After a few minutes of gluing the left aileron and flap, we realized the super glue we used had melted the foam under the carbon fiber coating. The next day we bought construction adhesive glue that was capable of working on foam. The holes that were made by the super glue melting the foam were big enough for us not to be able to reuse them, therefore, we had to repeat the process of cutting more slots for the hinges.

5.6 Fuselage Manufacturing

The fuselage, like the tail, was manufactured out of carbon fiber plates. These plates made up both the exterior walls and the bulkheads that act to maintain the shape of the fuselage

and provide much of the structural strength. These sections were put together with a combination of gorilla glue and a silicone based glue. A picture of two sections of the fuselage, including the bulkheads, is pictured in Fig 66.

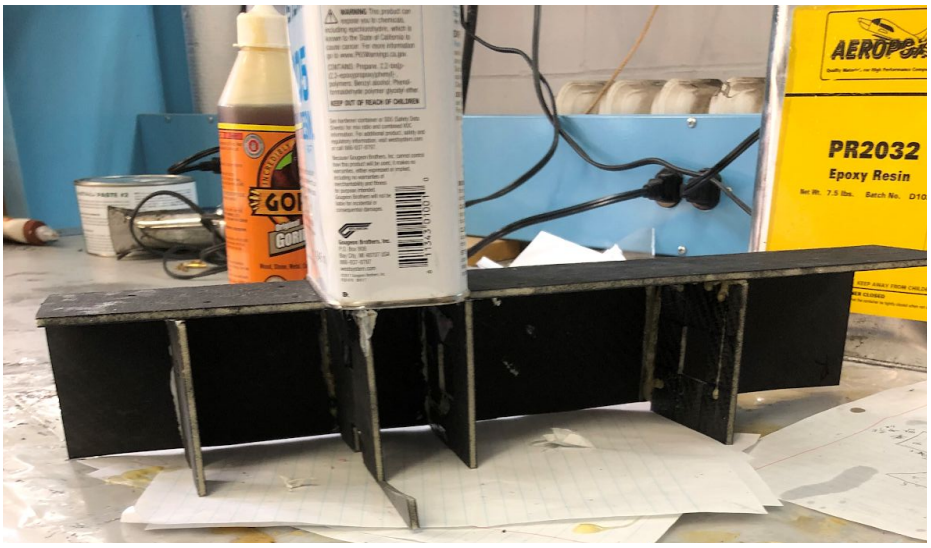

Figure 66: Fuselage Sections Drying

Additionally, the tail assembly was glued directly into the fuselage, fitting into slots left in the bulkheads left specifically to accommodate the tail boom. An image of the tail drying in place is provided as Fig 67.

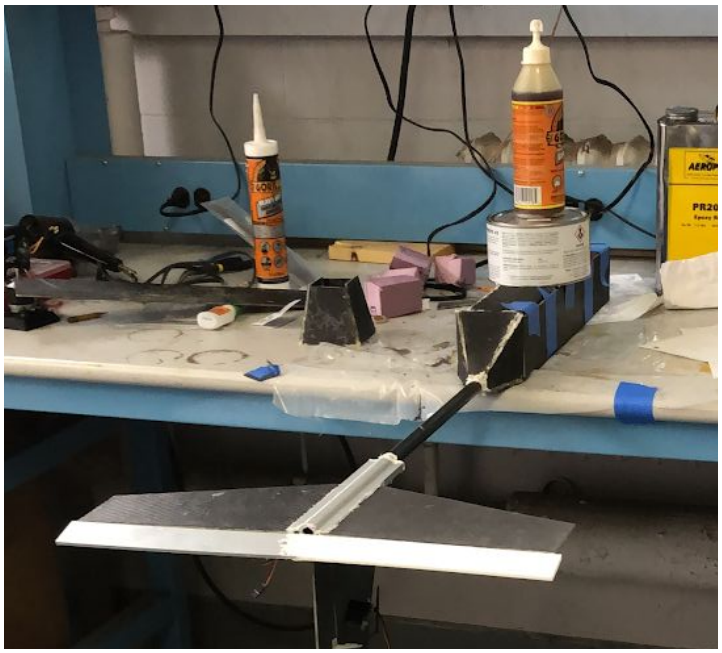

Figure 67: Tail Drying in Place

6.0 Design Verification and Testing

Through the course of this project, several tests were performed to validate theoretical results and each test conducted will be detailed in the subsections to follow.

6.1 Wind Tunnel Test

To validate the XFLR5 analysis conducted in Section 4.1.1, we conducted a wind tunnel test using the wind tunnel in the Higgins Laboratory Aerodynamics Laboratory in HL016. This wind tunnel is a water-cooled recirculating system with a 2ft by 2ft cross section and is capable of generating velocities in the test section up to 180ft/s. To fit the wing into the wind tunnel, we had to create a scaled model. In order to leave adequate space on either side of the wing, we decided to scale our 6.02 ft wingspan down to 20 inches. This caused the mean aerodynamic chord to be scaled to 2.4 inches.

To create the model for 3D printing, we created a model in 3 pieces, a left wing section, a right wing section, and a center wing section. Snapshots of the three sections are presented as Figs. 68, 69, and 70 below. The screw holes in the center wing were modeled directly after those in the AE3711 Aerodynamics class aerodynamics project (*see* Olinger, 2017) and the horizontal holes were sized in order to fit a small bolt through.

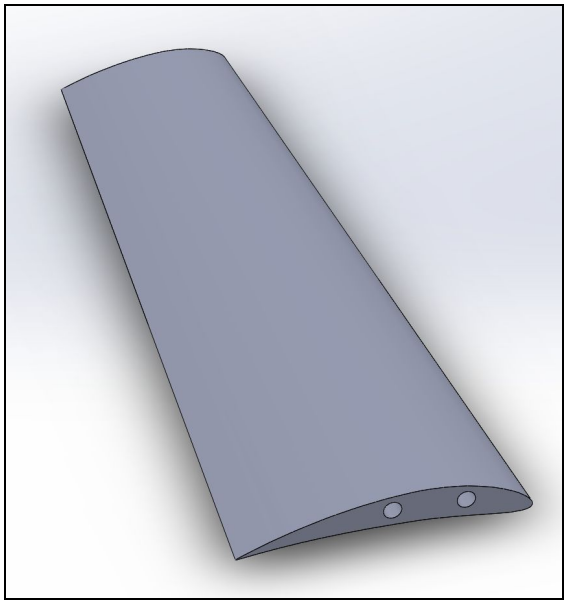

Figure 68: 3D Print Left Wing Section

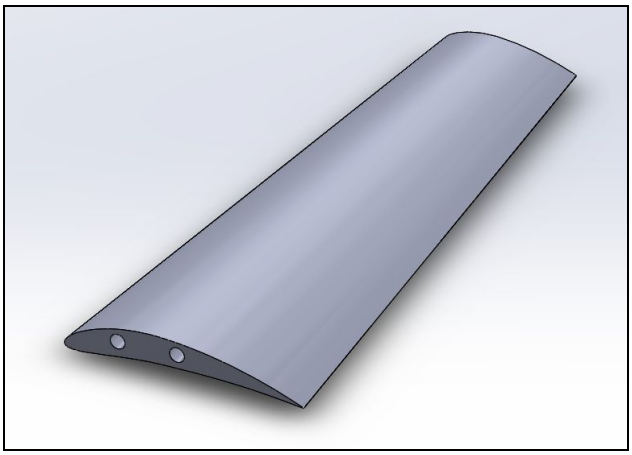

Figure 69: 3D Print Right Wing Section

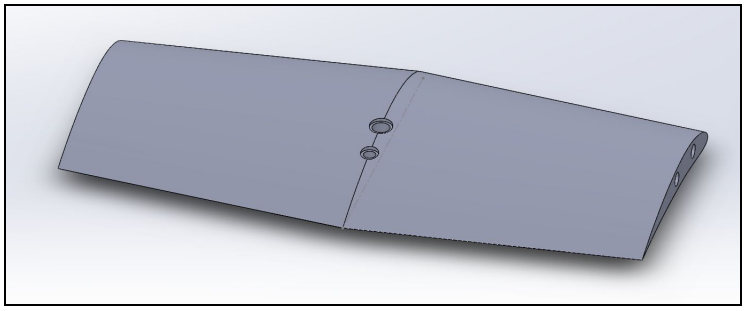

Figure 70: 3D Print Center Wing Section

These wing sections were originally 3D printed in polylactic acid (PLA), but the result was poor. The first attempt was done on its side, but toppled over mid-print and had to be discarded. The second attempt was done horizontally, but surface finish was incredibly poor and layers of the print peeled up while attempting to sand the wing. Images of the PLA print are displayed below in Figs. 71 and 72.

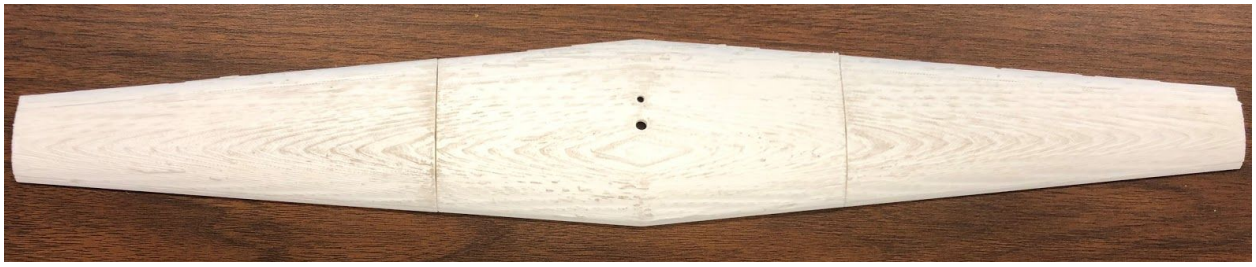

Figure 71: PLA Model

Figure 72: Zoomed in PLA Model

After this print, we contacted a friend, Andrew Kacherski, who was conducting directed research in Professor Brown's lab. He was able to print us a model of our wing in Draft through a resin deposition 3D printer. This print was significantly higher quality. Images of the wing are displayed in Figs. 73 and 74.

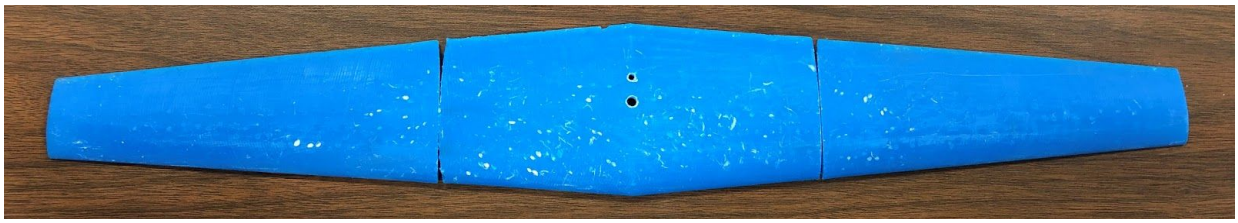

Figure 73: Final 3D Printed Model

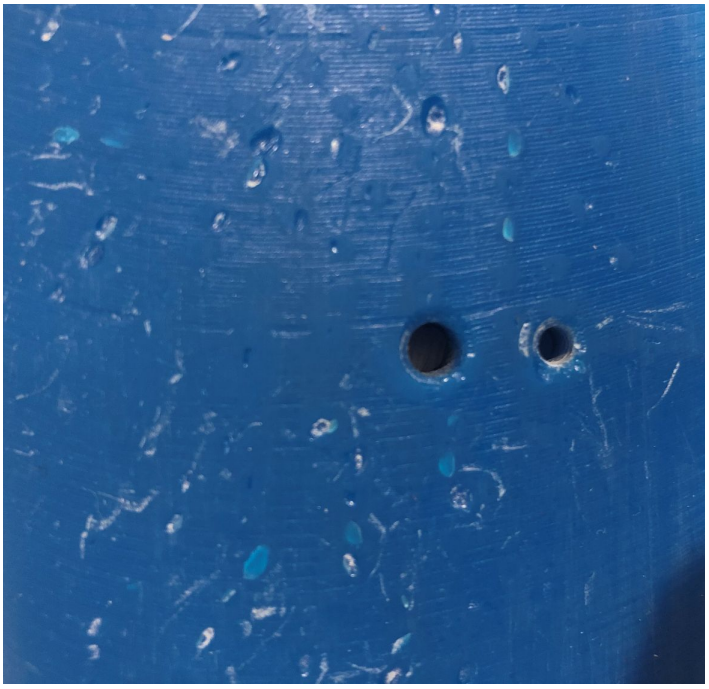

Figure 74: Zoomed in Final Mode

This wing was glued together using Gorilla Glue Gel, which provided an adequate hold and filled in the gaps left in the print.

Once the model was made, we had to match Reynold's numbers between the full size wing and the model. To do this, we took the Reynolds number found in Section 4.1.1 and rearranged Eqn. 12, inputting the model mean aerodynamic chord, and solved for the new airspeed that would be required for the wind tunnel test. This came out to 151 ft/s for the 6.02 ft span simulation.

To ensure that our test would not violate any structural limits of the force balance, we calculated the maximum normal force and maximum pitching moment that would be experienced during the test. To compute these estimates, we used the lift curve slope from the XFLR5 simulation results to get an idea of what angles of attack we could simulate in the wind

tunnel. Using the lift curve slope (5.209 rad^{-1}) and $Cl_{0,w}$, or coefficient of lift at zero angle of attack (-7 degrees) we used Eqn. 36 below to find the normal force on the wing:

$$N = \frac{(Cl_{0,w} + a \quad \alpha)\, S_{model} \quad \rho\, U^2}{2\, cos(\alpha)} \qquad (36)$$

We constrained our test to 15 degrees angle of attack, as we predicted stall at 12 degrees from the XFLR5 analysis. Applying both the velocities to this equation, we found that the normal force would be a maximum at 15 degrees angle of attack, and would have a value of 18.37 lbs for the 151 ft/s case and 24.84 lbs for the 176 ft/s case. The maximum allowable normal force is 25 lbs, so the risk would have to be mitigated in the 176 ft/s case by constraining angle of attack.

To find the maximum moment, the following equation was used:

$$M = B\, N \qquad (37)$$

Where B was the moment arm of 4 inches. The maximum allowable pitching moment for the force balance is 50 lb*in, which would be violated quite quickly in the 176 ft/s case, violating this condition at just over 4 degrees. This led us to drop that test case all together, as no useful data could be gathered from this analysis. The maximum angle of attack that the 151 ft/s case could withstand was 8 degrees. This was a conservative estimate that assumed linearity of the lift curve slope through all angles of attack, not taking into account the reduced slope at higher angles of attack. In the actual test, we were able to test beyond this 8 degree limit, but had to make sure that the gauge never indicated forces or moments that violated the allowable values and that the model did not experience excessive flutter effects.

Even though we had conducted these analyses, we still needed to make sure that the model would be able to withstand the forces that it would be subject to. As such, we slowly

ramped up the wind tunnel speed, making sure to put the airfoil through a series of angles of attack at several airspeeds along the way, watching both the gauges on the force balance to make sure that no physical constraints were being violated and watching the wing to make sure that flutter effects were not causing the wing to come apart. Once we were confident that the model would hold and that our estimates of maximum forces were valid, we conducted the test at the full 151 ft/s wind tunnel speed. On the HL016 wind tunnel, this speed corresponds to a motor frequency of 52Hz. An image of the wing mounted in the wind tunnel is depicted below as Fig. 75.

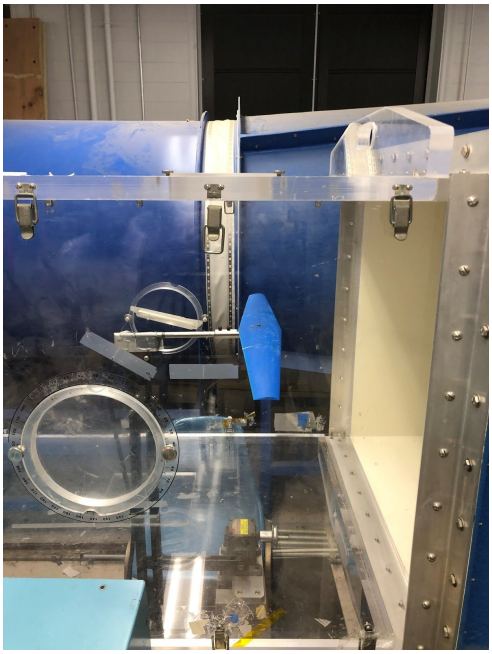

Figure 75: Model Wing Mounted in Wind Tunnel

At this speed, we were able to conduct two tests. The first test, we were able to record normal force and pitching moment over a range of -5 degrees to 13 degrees angle of attack before flutter effects started to make the team nervous. The second test was conducted between -5 and 12 degrees. During both of these tests, attempts were made to also record axial force to

give some sense to drag estimation, but the resolution limit on the sensor could not be reached, so axial force data was discarded.

After all data was recorded, the following equations were used to determine coefficient of lift and quarter chord moment coefficient:

$$Cl = \frac{Ncos(\alpha)}{\frac{1}{2}\rho U^2 S} \tag{38}$$

$$CM_{c/4} = \frac{M - B*N}{\frac{1}{2}\rho U^2 S} \tag{39}$$

From these equations, we were able to create plots of coefficient of lift and coefficient of moment for both tests and compare it to the data found from XFLR5. The plot of coefficients of lift are displayed below as Fig. 76.

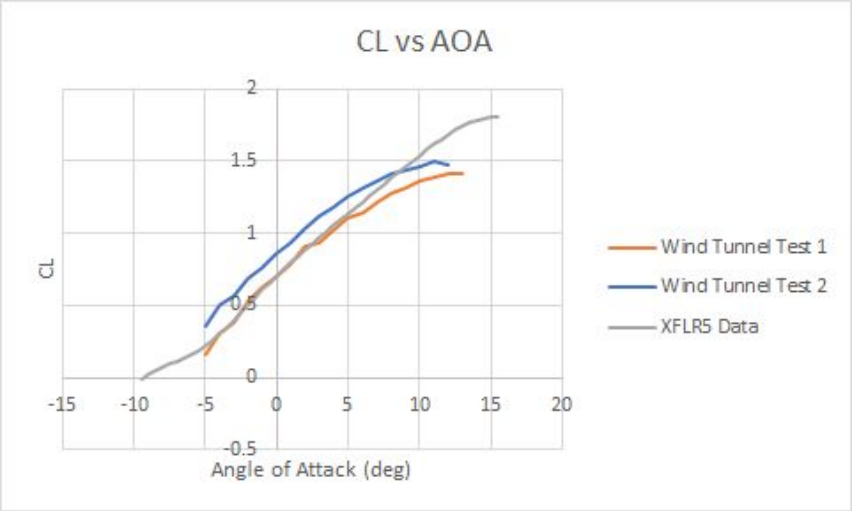

Figure 76: Lift Curve Comparison

From this plot, it becomes obvious that the lift curve slopes over the interval between about -5 degrees to 5 degrees, the most important range for our application, are mostly identical. In fact, the first wind tunnel test and the XFLR5 data overlap each other for the majority of this range. From conducting this test, it is our opinion that at high angles of attack, at least some of the decrease in coefficient of lift can be attributed to flutter effects that began in the wing above

about 7 degrees and became severe near 12 degrees angle of attack. Overall, we assert that in terms of lift curve, the wind tunnel data verifies the XFLR5 analysis. Below, a comparison of XFLR5 and wind tunnel data for moment coefficient is presented.

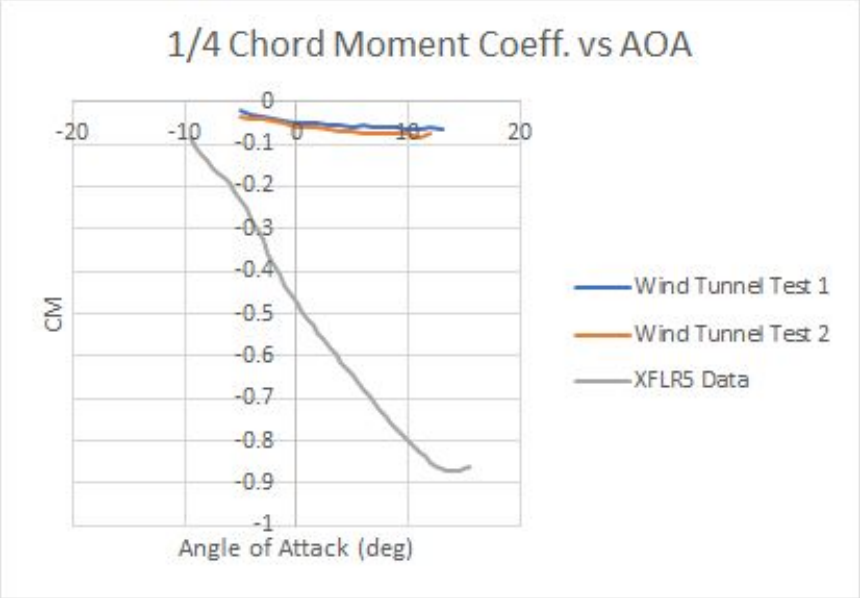

Figure 77: Moment Curve Comparison

Figure 77 displays a vast discrepancy between the theoretical and practical data in terms of moment. Upon further reading of the XFLR5 documentation, we discovered that the moment in Plane Mode, a functionality within XFLR5, measures the moment around point (0.25,0,0), which in our case, was essentially the front of the wing, not the quarter chord. There is no way documented to fix the location at which this moment is applied in the program. Stability analysis in XFLR5 calculates moments differently than the method used to perform hand calculations. As such, we plotted the moment coefficients from the wind tunnel test alone below.

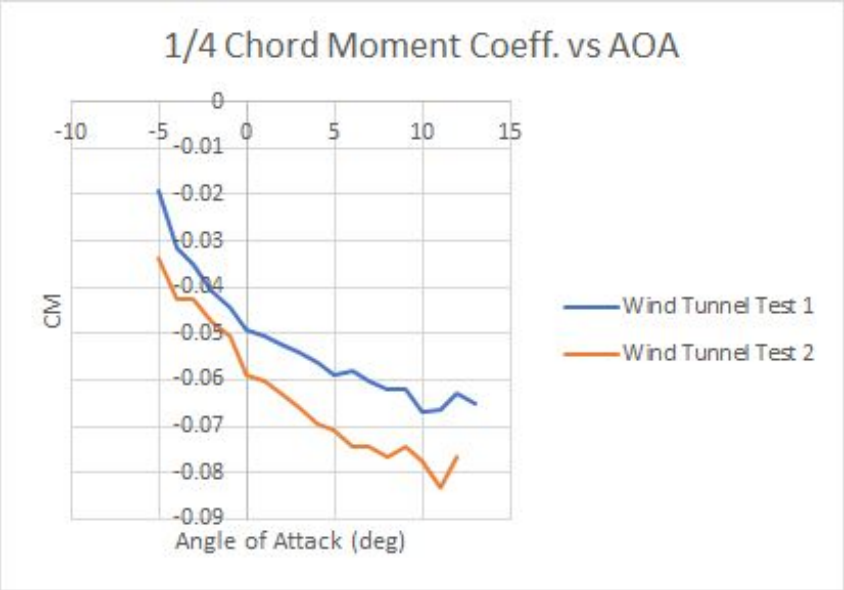

Figure 78: Empirical Moment Coefficient Curves

The reproducibility of results between the moment graphs were the reason why we looked further into the theory behind XFLR5 in terms of moment calculation. As such, for calculation of dynamic stability by hand, we used the moment data out of the wind tunnel test over the values from the XFLR5 plot.

6.2 Fuselage Structure Test

In order to decide what shape to use for our fuselage, the team conducted an impact test and a loading test on the sample square and circle fuselage that was previously mentioned in section 4.2. We conducted the impact test to see if and where cracks would occur during a possible crash when flight tests are conducted. The purpose of the loading test was to determine which shape is stronger and resistant to impact.

To impact test the fuselage we loaded the inside of the fuselage with coins that weighed a total of half a pound. The weight of the coins was determined by how many coins we could fit on

the inside of the fuselage. The coins were first put in a Ziploc bag and then rolled up and placed in the inside of the fuselage. We then proceeded to drop the loaded fuselage from a height of seven feet. This test was conducted on both the circular and square fuselage from the same height using the same amount of weight.

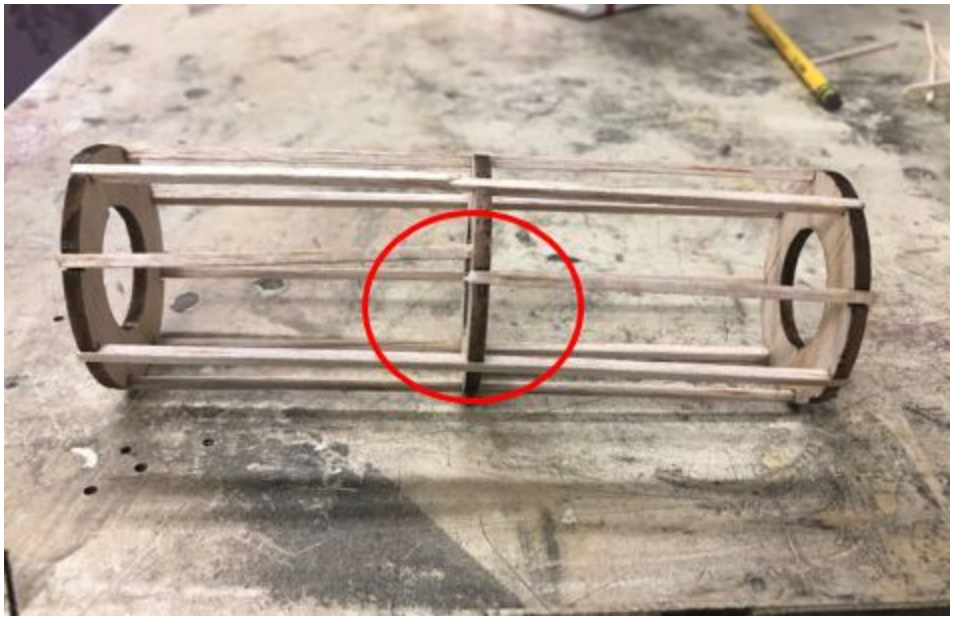

Figure 79: Broken Spar as A Result of Impact Test

The results from the impact test were different than we anticipated. We expected the circular fuselage to break at the spars but the square fuselage to break at the corners. However, both the circle and square fuselages only broke at the spars as seen in Fig. 79. We believe that the square fuselage didn't break at the corners because it was laser cut in one piece, therefore the stress concentrations were not as high as we anticipated. However, a circular airframe is the strongest construction. If a fuselage cross section is non-circular, there are points on it which will have to endure greater stress than others due to pressurization effects. If the fuselage is circular, then this load is spread more evenly, with no particular point under excessive stress.

To conduct the loading test, the team tested both square and circular fuselages similar to how balsa bridges are tested. We created our loading station using two screw hooks, a block of wood, and a bucket as seen in Fig. 80. We first inserted the block of wood into the fuselage and then screwed in the hooks after, so that way it could fit in the fuselage.

Figure 80: Materials Used to Conduct The Loading Test

We filled the bucket with sand until we saw signs of buckling and then failure as seen in Fig. 81. The square fuselage failed at 10.6 pounds and the circular fuselage failed at over eleven pounds. We were not able to get an accurate measurement for the weight of failure of the circular fuselage because our scale maxes out at eleven pounds. However, we believe the weight of failure was around 12 pounds.

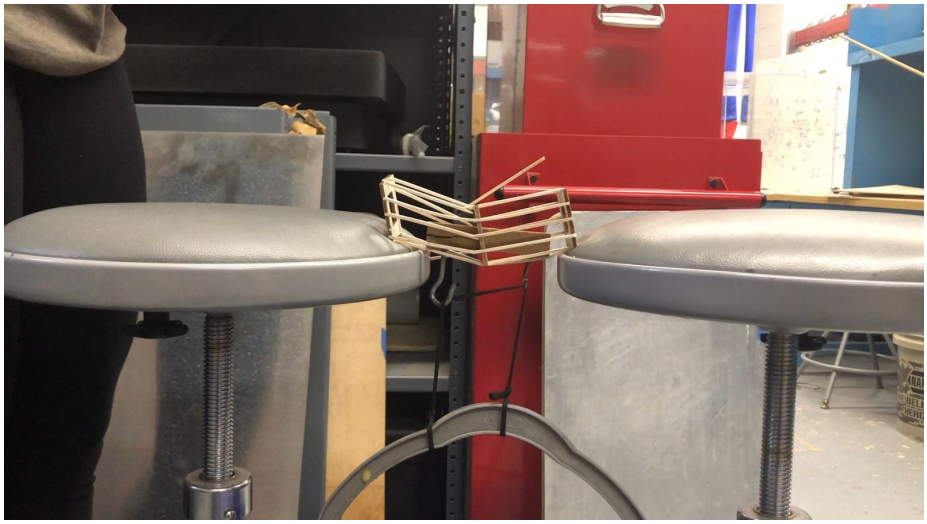

Figure 81: Fuselage Failure During Loading Test

In conclusion, we determined that based on our test results from both the impact and loading test, it would not make much of a difference what shape we went with for our fuselage. This is because both shapes broke the same way for the impact test, and failed around the same weight for the loading test. However, the team decided to use carbon fiber to construct our plane. Due to the nature of the material and construction process the team has decided to proceed with a square fuselage design, as it is extremely difficult to construct a circle fuselage from carbon fiber.

6.3 Wing Loading Test

To verify that our wing would not experience failure during normal flight conditions, we performed a wing loading test. For an in depth analysis of the aerodynamic loads experienced during a level turn at minimum turning radius, see Section 4.1.7. Unfortunately, an experimental design for an elliptically loaded wing is not simply constructed. As such, a modified test case had to be developed.

The condition we wished to match was the normal stress found at the wing root using weights placed at the wing tip. Using the simplified wing model in Section 4.1.7 and performing a simple loading analysis, it was determined that a load of 6.5 lbs placed at the wing tip would be sufficient to match the desired stress condition. A plot of this elliptical loading versus spanwise length of the wing is presented below.

Figure 82: Normal Stress vs Spanwise Wing Position

In the lab, the closest to the loading condition derived above that we could produce with available equipment was 7.5 lbs, which is more conservative than the derived case. The weight is displayed in the Fig. 83 below.

Figure 83: Weight for Wing Load Test

The aircraft was held firm to a lab stool at the wing root as the weight was applied to the wing tip. The wing did not break, thereby verifying that our design is sufficient for our application. In fact, the wing does not flex when the load is applied. In this way, the design is an improvement over the 2018-19 MQP (*see* Celaj et al, 2019), which cited issues with wing flex as one major issue with their stability. An image of such a test is included as Fig. 84.

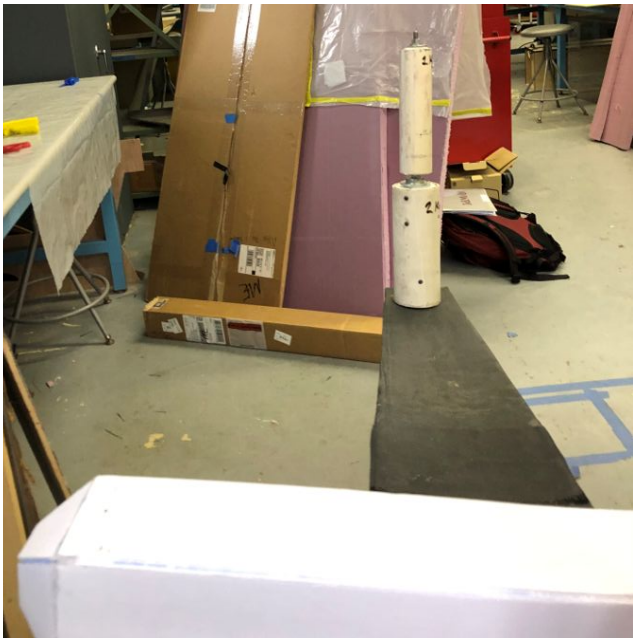

Figure 84: Wing Load Test

6.4 Glide Test

At the end of B term, a glide test was conducted on a mock-up of the final aircraft design. This mock-up had a wooden tail and foam board fuselage, as opposed to carbon fiber components seen in the final design. Weights were placed throughout the fuselage to simulate the weight of the motor and other components that were not included in the test model. Pictures of the model taken before the glide test are displayed in Figs 85-87.

Figure 85: Isometric View of Glide Test Model

Figure 86: Front View of Glide Test Model

Figure 87: Right View of Glide Test Model

For this test, the aircraft was tossed twice from a standing height to ensure that the model could hold up, and once from atop a ladder. The test from atop the ladder was the best simulation of actual flight available to us, and was the primary focus of this experiment.

Based on the flight path from this short glide experiment, it was determined that our aircraft possessed an adequate level of stability to proceed with the final design. At the end of the flight, the tail became loose, as the glue holding the tail boom broke free. This caused the aircraft to roll and dive at the end of the flight. This was not believed to be a result of a design flaw, but as a result of a poor selection of materials for the glide test model.

This glide test was also accompanied by telemetry recordings from the Pixhawk. This data was marred by significant noise and was largely unusable. It remains unknown whether this noise was a result of issues in recording data or if the sensors became loose during the test. Making sure that data was properly recorded is a major consideration for the final flight test.

6.5 Flight Test

The initial flight test took place after the end of C term. This was to be a check flight before the competition, but due to constraints surrounding Coronavirus, this became our only opportunity to test our aircraft. Unfortunately, this test was not successful, leaving much room for future improvement.

Within a few seconds of our hand launch, the aircraft seemed to struggle to maintain airspeed. The pilot increased throttle and pulled up in an attempt to gain altitude and avoid a crash. Unfortunately, this maneuver resulted in a low altitude stall, which was unrecoverable. The aircraft crashed after about eight seconds of flight time, landing hard on the left wing. This crash resulted in separation of several of the plates that made up the fuselage, but little to no damage to any individual plates, and no realized damages to electronics, though not all electronics were tested for functionality after the crash. An image of the wreckage is displayed below.

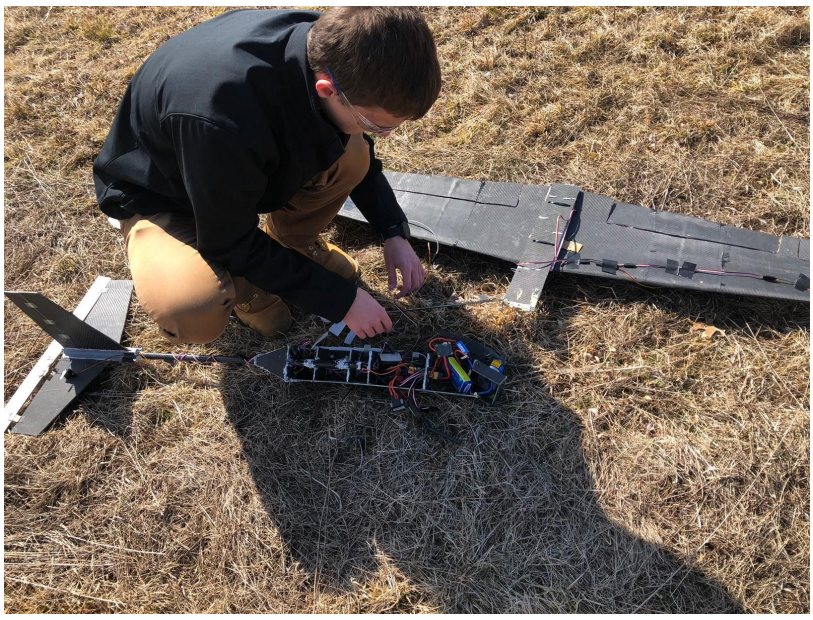

Figure 88: Flight Test Wreckage

Due to technical issues and the unavailability of electrical power at the ground station, telemetry data was unable to be recorded for this flight. This data would have been helpful in diagnosing the issue. Instead, we had to rely on the intuition of the pilot and RC Club members present for the flight demonstration. Based on the pilot's perceptions, he believed that the center of gravity was slightly too far back. This may have been able to be corrected if we had more power available, but the battery and engine combination was limiting.

The RC Club members also noted that the CG may need to be pushed forward about an inch. They also suggested a larger battery, as the motor we selected can pull a significantly higher current than what we have available. Unfortunately this was not a solution available to us due to the constraints in the competition rules.

The consensus solution was to add landing gear to the front of the fuselage to push the CG forward, push the payload mount forward about an inch to an inch and a half, and add ballast until the CG was located in a more optimal position. Due to campus being shut down, this modification was never made, and must be left as future work.

7.0 Summary, Conclusions, Recommendations, Broader Impact

7.1 Summary and Conclusions

Our team worked to design a MAV that would meet and exceed the requirements for the 2020 WPI UAV Competition. We were able to do this by creating several design objectives, such as designing a smaller fuselage, using a carbon fiber laminate on all aircraft components, and using foam board to create our wing, during the initial stages of the project. Once the

objectives were set, they gave us an idea of what we had to do during the construction stage of the project. The final design of our aircraft was small, with an overall length of 3.8 ft and lightweight with an empty weight of 3.92 lbs. Empty weight was minimized by using a carbon fiber rod connecting the fuselage to the tail and the lightest propulsion system available. The effectiveness of our aircraft was verified by theoretical calculations, a glide test, and a flight test once the aircraft was completed. The flight test proved and demonstrated how the aircraft experienced challenges with stability and handling.

After twenty-one weeks of analysis, literature review, and research, we successfully manufactured, designed, and flew a fixed wing micro aircraft vehicle that met the requirements for the 2020 WPI UAV Competition. We made several iterations on our initial design during the process of building the aircraft in order to make sure the aircraft was the most efficient and lightweight as possible. The last week of C Term we were able to conduct our flight test. However, the aircraft was tailheavy and ended up stalling, causing the aircraft to crash. Thankfully, the damage that occurred to the aircraft was easily repairable and was to be fixed during the first week of D Term. We decided to make small modifications to the design, namely moving the payload mechanism forward and the addition of a landing ski in order for the aircraft not to be as tail heavy. Due to the Coronavirus outbreak and health and safety precautions, the 2020 WPI UAV Competition was cancelled and we were not able to participate. Nonetheless, our aircraft met the requirements of the competition and was expected to be capable of flying by the scheduled date of the competition.

7.2 Challenges and Recommendations

The design decision to use carbon fiber as a primary building material presented significant challenges to the design of the aircraft. Unlike with a traditional building material, such as balsa, foam board, or a 3D printed material, the carbon fiber material can not be manufactured with the same precision. As a result, post processing and re-work to ensure correct dimensionality and eliminate defects such as delaminations took additional time that pushed back other tasks in the timeline. Additional delays were introduced due to the long lead times in procuring materials for carbon fiber manufacturing, such as the epoxy, foam inlay material, and mold release agent.

Control design was also influenced heavily by early design decisions. The team decided early on to use a PX4 Mini flight controller to record data from flight as part of the project requirelement, as well as implement autonomy into the project as part of the project score. This decision resulted in delays related to software difficulties with the flight controller. The initial perception by the team was that the PX4 Mini would be a plug-and-play solution to all of our control system needs, but the added complexity of an off the shelf flight controller required extensive tuning and hours of research to implement properly due to the complexity of the menus present in the software and the low level of detail provided in the documentation.

The flight test revealed minor issues in the design, namely a lack of power to the engine and a center of gravity that was too far to the rear of the aircraft. The center of gravity issue was going to be simple to resolve with the addition of landing gear, a re-organized placement of electronics in the fuselage, a more forward placement of the payload release mechanism, and added ballast. The power issue was going to need more investigation, but might be aided by a

larger propeller. Unfortunately, these changes were not implemented due to circumstances related to the Coronavirus pandemic.

The first recommendation that we can make is to come up with a detailed parts list in the early stages of the project. Several times throughout the course of this project, we were stuck waiting on materials to be ordered and delivered. If all purchases were made in the beginning of the project, or at least as soon as the need for a specific part was realized, we could have had the fuselage built by the end of B term, rather than half-way through C term. This would have provided extra time to work on configuring the electronics inside of the fuselage, and improved the location of the center of gravity and better laid out the servo mechanisms.

Another improvement could be made in the area of autonomy. We spent a significant amount of time learning how to make a control system work with a Pixhawk, and how to record data to the device. It was not until late in the project that we started to work on implementation of autonomy into the control system. As a result, by the time of competition, our autonomy was not in a mature state. As a result, we lost a significant amount of points that would have been available if we were able to implement more functionality. For this reason, we would recommend that in future projects, someone should be assigned to work on the autonomy stack from the outset of the project. This will allow the team to have an expert in the autonomous systems, who will be able to influence the structural and control design to effectuate the use of autonomy in aircraft controls.

In terms of propulsion, our team ran into issues due to the unavailability of a thrust stand. As a result, our engine selection and propulsion design were based only on eCalc simulations and the recommendations of individuals with experience building RC aircraft. Ideally, we would

have liked to test a number of engine and propeller combinations in order to decide on the best combination for our design and buy a motor accordingly. We would suggest that future teams look into buying a new thrust stand, and performing a set of thrust tests. This will allow for a more tailored engine selection, and would likely lead to better performance.

The Coronavirus outbreak prevented the team from being able to complete the project and implement changes after the flight test. As previously discussed, the design could benefit from a farther forward center of gravity, which could be achieved by the addition of landing gear, a reorganization of internal electronics, replacement of the payload mechanism, and added ballast. For future projects, a larger battery, possibly a four cell LiPo could be beneficial if using the engine we selected. This would allow for the motor to draw more current and produce more thrust. This would allow for the aircraft to be more forgiving, and possibly be able to pull out of a stall like the one that caused our crash.

7.3 Project Broader Impact

The main goal of this project was to design an aircraft capable of carrying a payload and dropping said payload accurately. This capability could be beneficial in several applications, both civilian and military. One key example would be in autonomous delivery of supplies into a disaster area. A long range, high payload capacity, and ability to drop a payload autonomously could greatly increase the ability of aid workers to deliver critical supplies, such as food, water, medicine, etc. in a timely manner and over rough terrain. The autonomous operation also takes out the need for aid workers to control the aircraft and search for those in need. Marking the GPS location of a payload drop would not be too much of a technical undertaking, and would allow for aid workers to be able to find those in need faster.

References

Administration, F. A. (2009). Pilot's Handbook of Aeronautical Knowledge 2008: Faa-H-8083-25A. Chicago: Aviation Supplies & Academics, Inc.

Andraka, A. Rosano, A. Sullivan, C. Pugliese, C. Cashman, D. (2015). Design of a Micro Aerial Vehicle

Blair, J. Connors, E. Irwin, D. Mehrtens, K. Sarria, C (2012). Design of a Micro Aircraft for the 2012 SAE Aero Design Design East Competition

Brown, A. Korza, A. Asare, G. Donahue, J. DiMilia, M. (2017). Micro Aircraft Design DBF-2017

Celaj, D. Cummings, H. Frewein, A. Oswald, M. Wilson, A. (2019). Design of a Micro Aircraft for the 2019 SAE Aero Design Design East Competition

Commutating Encoder. (2019, June 20). Retrieved 25, 2019, from https://www.quantumdev.com/brushless-motors-vs-brush-motors-whats-the-difference/

Cowlagi, R. (2019). 2020 WPI UAV Competition Rules, Worcester Polytechnic Institute

Cowlagi, R. (2019). Aircraft Dynamics and Control, Worcester Polytechnic Institute. [class notes]

FliteTest How To Choose The Perfect Brushless Motor (2108). Retrieved 4, 2019, from https://www.flitetest.com/articles/how-to-choose-the-perfect-brushless-motor

Gadd, C. (n.d.). Servo Torque Calculator. Retrieved from http://www.mnbigbirds.com/Servo Torque Caculator.htm

Iskrev, B. (2015, October 18). Pusher vs Tractor Propellers. Retrieved 4, 2019, from https://www.masterairscrew.com/pages/pusher-vs-tractor-propellers

Liang, Oscar. “What Are ESC, UBEC and BEC.” *What Are ESC, UBEC and BEC*, 26 Nov. 2016, https://oscarliang.com/what-is-esc-ubec-bec-quadcopter/.

Lipka, D. Breault, E. McCaffrey, E. Scott, E. Feldman, G. (2014). Design and Construction of a Micro Aerial Vehicle for the 2014 SAE Aero Design East Competition

Montgomery, C. (2014, June 3). Multi-Rotors, First-Person View, And The Hardware You Need. Retrieved from https://www.tomshardware.com/reviews/multi-rotor-quadcopter-fpv,3828-2.html

Mueller, Markus. (2019). eCalc Propeller Calculator. https://www.ecalc.ch/motorcalc.php?ecalc&lang=en.

Napolitano, M. (2012). *Aircraft Dynamics*. Hoboken (NJ): J. Wiley & Sons.

Olinger, D. (2017). Aerodynamics, Worcester Polytechnic Institute. [class notes]

Olinger, D. (2019). Aircraft Design, Worcester Polytechnic Institute. [class notes]

Raymer, Daniel P. (2018). Aircraft Design: A Conceptual Approach 6th Edition. Reston: AIAA

RC Airplanes. (2019 4). RC Airplane Propellers. How to select and prepare. Retrieved 20, 2020, from https://www.rc-airplanes-simplified.com/rc-airplane-propellers.html

RC Airplanes Victor (2016). HOW TO CHOOSE A RC ELECTRIC MOTOR AND PROPELLER FOR YOUR PLANE https://www.youtube.com/watch?v=EL1vt9ufEcE&t=270s

Schneider, B., Brian, & Roger. (2020). A Guide to Understanding LiPo Batteries. Retrieved November 15, 2019, from https://rogershobbycenter.com/lipoguide

Smith, A. Andrews, B. Brown, C. Cahill, C. Thiesse, D. (2016). Design and Optimization of a Micro-Aerial Vehicle

Traub, Lance. (2011). Range and Endurance Estimates for Battery-Powered Aircraft. Journal of Aircraft. 48. 703-707. 10.2514/1.C031027.

Weakley. (2018). Selecting propellers | theParkPilot.org. Retrieved 6, 2020, from http://www.theparkpilot.org/selecting-propellers

XFLR5 Analysis of Foils and Wings Operating at Low Reynolds Numbers (2009). https://engineering.purdue.edu/~aerodyn/AAE333/FALL10/HOMEWORKS/HW13/XFLR5_v6.01_Beta_Win32%282%29/Release/Guidelines.pdf

Appendix A: Score Estimation MATLAB Script


```
clc; clear all;

%Defining parameters
lam1=.01;
% lam2=35;
% lam3=35;
% a1=1;
% a2=1;
% a5=1;
% a3=3;
% a4=5;
% del=0;
n=1.3;
eta=.5;
v=11.1;
c=2.2;
rho=1.225;
S=.3846;
CD0=.03;
W=3*9.81;
e0=.75;
AR=8.76;
k=1/(pi*AR*e0);
Rt=1;
vel=linspace(0,20,1000);
% Rmax=Rt^(1-n)*((eta*v*c)/((1/(rho*S))*CD0^(1/4)*(2*W*sqrt(k))^(3/2)))^(n)*sqrt(((2*W)/(rho*S))*sqrt(k/CD0))*3600
% sqrt(((2*W)/(rho*S))*sqrt(k/CD0))

%Range at full weight
t=Rt.^(1-n).*((eta.*v.*c)./(.5.*rho.*vel.^3.*S.*CD0+((2.*W.^2.*k)./(rho.*vel*S)))).^n;
Range=t.*3600.*vel;
maxR=max(Range);
index=find(Range==maxR);
Ideal_airspeed=vel(index);
ideal_time=t(index)*60;
string1='Ideal Cruise Speed is:\n %4.2f m/s\n';
fprintf(string1,Ideal_airspeed)
string2='Maximum flight time is:\n %4.2f min\n';
fprintf(string2,ideal_time)

%Score at full weight
srec=[];
for int=[1:3]
    W_p=int.*0.454;
    W_e=3-W_p;
    s=lam1.*(W_p./W_e).*Range;    %+lam2.*del+lam3.*(a1+a2+a3+a4+a5)+P;
    srec=[srec;s];
end

%plots
figure()
plot(vel,Range)
grid on
title('Expected Range vs Airspeed')
xlabel('Airspeed (m/s)')
ylabel('Range (m)')

figure()
plot(vel,srec)
grid on
title('Expected Score vs Airspeed')
xlabel('Airspeed (m/s)')
```

```
ylabel('Score')
legend('1 lb payload','2 lb payload','3 lb payload')

%Range at 3.61 lbs empty weight
W=[(3-(2*0.454))*9.81;(3-(1*0.454))*9.81;3*9.81];
t=Rt.^(1-n).*((eta.*v.*c)./(.5.*rho.*vel.^3.*S.*CD0+((2.*W.^2.*k)./(rho.*vel*S)))).^n;
Range1=t.*3600.*vel;

%Score at 3.61 lbs empty weight
srec=[];
for int=[1:3]
  W_p=int.*0.454;
    W_e=3-(3*0.454);
    s=lam1.*(W_p./W_e).*Range1(int,:);    %+lam2.*del+lam3.*(a1+a2+a3+a4+a5)+P;
    srec=[srec;s];
end

%plots
figure()
plot(vel,Range1)
grid on
title('Expected Range vs Airspeed (3.61 lb Empty Weight)')
xlabel('Airspeed (m/s)')
ylabel('Range (m)')
legend('1 lb payload','2 lb payload','3 lb payload')

figure()
plot(vel,srec)
grid on
title('Expected Score vs Airspeed (3.61 lb Empty Weight)')
xlabel('Airspeed (m/s)')
ylabel('Score')
legend('1 lb payload','2 lb payload','3 lb payload')
```

```
Ideal Cruise Speed is:
 11.89 m/s
Maximum flight time is:
 21.53 min
```

Appendix B: Sizing and Static Stability MATLAB Script

Contents


```
clc; clear all;
```

Wing Sizing

```
wcruise= 6.6;       %lbs
w0=wcruise;
cd0=.015;           %parasitic drag

W_S=-.0217*w0+1.7359;             %wing load lb/ft^2---based on past MQP's

v=42;               %velocity ft/s

%atospheric model
a=-1.9812e-3;
t0=288.16;
p0=.0023769;
r=3.0892e3;
h=500;
t=t0+a*h;
p=p0*(t/t0)^(-1-(32.15/(a*r)));


S=w0/(W_S);          %wing area
AR=-0.1047*w0+9.4498;               %Aspect Ratio-------based on past MQP's

b=sqrt(AR*S);        %wingspan

Clreq=(wcruise/(.5*p*v^2*S))*(1+(2/AR));       %Required Coeff. of Lift

q=.5*p*v^2;                                    %dynamic pressure

string1='Coefficient of Lift Required\n %4.2f\n';
fprintf(string1,Clreq)
string2='Wing Area\n %4.2f ft^2\n';
fprintf(string2,S)
string3='Aspect Ratio\n %4.2f\n';
fprintf(string3,AR)
string4='Wing Span\n %4.2f ft\n';
fprintf(string4,b)

croot=.9487;                                    %wing root chord
lam=.45;                                       %taper ratio
ctip=croot*lam;                                 %wing tip chord
mean_aero_c=((2/3)*croot*(1+lam+lam^2))/(1+lam);
string7='Mean Aerodynamic Chord\n %4.2f\n';
fprintf(string7,mean_aero_c)

mu=3.737e-7;                                    %viscosity
```

```
Re=(p*v*mean_aero_c)/(mu);
string5='Reynolds Number\n %4.2f\n';
fprintf(string5,Re)
```

```
Coefficient of Lift Required
 0.95
Wing Area
 4.14 ft^2
Aspect Ratio
 8.76
Wing Span
 6.02 ft
Mean Aerodynamic Chord
 0.72
Reynolds Number
 189752.59
```

Tail Sizing

```
length=0.2961*w0+1.8319;
string6='Estimate of Overall Length\n %4.2f ft\n';
fprintf(string6,length)

C_HT=.5;                                %horizontal tail volume coeff
C_VT=.04;                               %vertical tail volume coeff
L_HT=3;                                 %moment arm estimate
L_VT=3;                                 %moment arm estimate

S_ht=C_HT*(mean_aero_c/L_HT)*S;              %horizontal tail area
S_vt=C_VT*(b/L_VT)*S;                        %vertical tail area

string6='Horizontal Tail Area\n %4.2f ft\n';
fprintf(string6,S_ht)
string6='Vertical Tail Area\n %4.2f ft\n';
fprintf(string6,S_vt)

AR_ht=4;                                %horizontal tail aspect ratio
AR_vt=1.5;                              %vertical tail aspect ratio

lam_ht=.5;                              %ht taper
lam_vt=.5;                              %vt taper

b_ht=sqrt(AR_ht*S_ht);                   %ht span
height_vt=sqrt(AR_vt*S_vt);              %vt height

string6='Horizontal Tail Span\n %4.2f ft\n';
fprintf(string6,b_ht)
string6='Vertical Tail Height\n %4.2f ft\n';
fprintf(string6,height_vt)
```

```
Estimate of Overall Length
 3.79 ft
Horizontal Tail Area
 0.50 ft
Vertical Tail Area
 0.33 ft
```

```
Horizontal Tail Span
 1.41 ft
Vertical Tail Height
 0.71 ft
```

Static Stability

```
hac=.25; %unless otherwise stated
ltb=3/mean_aero_c;

cmac=-.46;
clow=0.71;

% ep=0;
% it=0;
a=5.209;
at=5.27;
deda=(2*a)/(pi*AR);

vh=(S_ht/S)*(ltb/mean_aero_c);

abar=a+at*(S_ht/S)*(1-deda);

hnp=hac+(at/abar)*(1-deda)*vh;          %ND location of NP behind 1/4 chord

dimensional_np=hnp*mean_aero_c;         %Dimensional location NP

string='Neutral Point % Chord\n %4.2f \n';
fprintf(string,hnp)
string='Neutral Point\n %4.2f ft behing leading edge\n';
fprintf(string,dimensional_np)

eta=.9;
A=eta*(S_ht/S)*(at/a)*(1-deda);

hmf=(-.15+hac+A*ltb)/(A+1);          %ND location of MFP behind 1/4 chord

dimensional_mf=hmf*mean_aero_c;          %Dimensional location MFP

string='Most Forward Point % Chord\n %4.2f \n';
fprintf(string,hnp)
string='Most Forward Point\n %4.2f ft behing leading edge\n';
fprintf(string,dimensional_np)
% h=.25;
% dcmda=abar*(h-hac)-at*vh*(1-deda)  %1/rad
% cm0=cmac+clow*(h-hac)-at*(it-ep)*vh*(1-(h-hac)*(mean_aero_c/ltb))
%
%
% alpha=0*pi/180
% cm=cm0+dcmda*alpha
%
% v=42;
%
% dimensional_quantity=.5*p*v^2*S*mean_aero_c;
%
% M0=cm0*dimensional_quantity
% M=cm*dimensional_quantity
%
%
% trimaoa=-cm0/dcmda
```

```
Neutral Point Neutral Point
 0.47 ft behing leading edge
Most Forward Point Most Forward Point
 0.47 ft behing leading edge
```

Wing Loading

```
ep0=1.78*(1-.045*(AR)^.68)-.64;
CD0=.015;

WS_cruise=q*sqrt((CD0*pi*AR*ep0));

string='Wing loading at the cruise condition:\n %4.2f lbs/ft^2\n';
fprintf(string,WS_cruise)

WS_loiter=q*sqrt((3*CD0*pi*AR*ep0));

string='Wing loading at the loiter condition:\n %4.2f lbs/ft^2\n';
fprintf(string,WS_loiter)

CLmax=1.8;
vstall=sqrt((2*wcruise)/(S*p*CLmax));

string='Stall Speed:\n %4.2f ft/s\n';
fprintf(string,vstall)

WS_stall=.5*p*vstall^2*CLmax;

string='Wing loading at the stall condition:\n %4.2f lbs/ft^2\n';
fprintf(string,WS_stall)

WS_vec=[WS_cruise,WS_stall,WS_loiter];
WS_for_wing_size=min(WS_vec);

string='Minimum Wing Loading:\n %4.2f lbs/ft^2\n';
fprintf(string,WS_for_wing_size)

if WS_for_wing_size==WS_stall
    disp('please add flaps')
else
    disp('no flaps needed')
end
```

```
Wing loading at the cruise condition:
 1.18 lbs/ft^2
Wing loading at the loiter condition:
 2.04 lbs/ft^2
Stall Speed:
 27.49 ft/s
Wing loading at the stall condition:
 1.59 lbs/ft^2
Minimum Wing Loading:
 1.18 lbs/ft^2
no flaps needed
```

Refined Wing Size

```
new_wing_area=w0/WS_for_wing_size;

string2='Revised Wing Area\n %4.2f ft^2\n';
fprintf(string2,new_wing_area)

New_span=sqrt(AR*new_wing_area);

string4='Revised Wing Span\n %4.2f ft\n';
fprintf(string4,New_span)

Clreq=(wcruise/(.5*p*v^2*S))*(1+(2/AR));       %Required Coeff. of Lift

ave_chord=new_wing_area/New_span;

z=[1/2 1/2;0.45 -1];
root_and_tip=z\[ave_chord;0];

mean_aero_c=((2/3)*root_and_tip(1)*(1+lam+lam^2))/(1+lam);

string7='New Mean Aerodynamic Chord\n %4.2f\n';
fprintf(string7,mean_aero_c)

Re=(p*v*mean_aero_c)/(mu);

% S_ht=C_HT*(mean_aero_c/L_HT)*S                  %horizontal tail area
% S_vt=C_VT*(b/L_VT)*S                            %vertical tail area
%
% string6='New Horizontal Tail Area\n %4.2f ft\n';
% fprintf(string6,S_ht)
% string6='New Vertical Tail Area\n %4.2f ft\n';
% fprintf(string6,S_vt)
%
% b_ht=sqrt(AR_ht*S_ht)                       %ht span
% height_vt=sqrt(AR_vt*S_vt)                  %vt height
%
% ave_c_ht=S_ht/b_ht;
% ave_c_vt=S_vt/height_vt;
%
% z=[1/2 1/2;0.5 -1];
% ht_root_and_tip=z\[ave_c_ht;0]
% vt_root_and_tip=z\[ave_c_vt;0]
%
% vh=(S_ht/new_wing_area)*(ltb/mean_aero_c);
%
% abar=a+at*(S_ht/new_wing_area)*(1-deda);

% hnp=hac+(at/abar)*(1-deda)*vh          %ND location of NP behind 1/4 chord
%
% dimensional_np=hnp*mean_aero_c         %Dimensional location NP
%
% A=eta*(S_ht/Final_wing_area)*(at/a)*(1-deda);
%
% hmf=(-.15+hac+A*ltb)/(A+1)
%
% dimensional_mf=hmf*mean_aero_c
```

```
Revised Wing Area
 5.60 ft^2
Revised Wing Span
 7.00 ft
New Mean Aerodynamic Chord
 0.84
```

Published with MATLAB® R2019a

Appendix C: Preliminary Budget

Item	Cost ($)	Link
West System 105 Resin 206 Hardener bundle	84.95	Hardener and Resin
Polyurethane Foam	48	https://store.acpsales.com/products/7752/polyurethane-foam
Pixhawk 4 mini	189.95	https://www.amazon.com/Pixhawk-Mini-Flight-Controller-GPS/dp/B07NWF6XZL
Electronics	160	--
Twill Roll Wrapped Carbon Fiber Tube*	52	https://store.acpsales.com/products/2374/carbon-fiber-twill-roll-wrapped-tubing?_vsrefdom=www.google.com
Misc	20	--
Total	554.9	

Appendix D: Material Properties Calculations

```
@author: Salamone
'''
'Volumes from SolidWorks'

vol_foam = 0.2489       # ft3
vol_carb = 0.02529      # ft3
density_foam = 1.548 # lb/ft3

'Experimental Values'

total_mass = 1.17       #pounds


def massfoam(v, d):
    mass_foam = v*d
    return(mass_foam)

mf = round(massfoam(vol_foam, density_foam),3)
print('Mass of Foam', mf, 'pounds')

def densitycf(tot, mf, vc):
    dcf = (tot - mf)/vc
    return(dcf)

rho_cf = round(densitycf(total_mass, mf, vol_carb),3)
print('Density of Carbon Fiber', rho_cf, 'lbs/ft3')
```

Code by Michael Salamone

Appendix E: Final Drawing